Super-resolution and super-localization microscopy: A novel tool for imaging chemical and biological processes

by

Bin Dong

A dissertation submitted to the graduate faculty in

partial fulfillment of the requirement for the degree of

DOCTOR OF PHILOSOPHY

Major: Analytical Chemistry

Program of Study Committee:
Wenyu Huang, Major Professor
Robert S. Houk
Emily Smith
Diane Bassham
Sanjeevi Sivasankar

Iowa State University

Ames, Iowa

2015

To

Dr. Ning Fang

My families

TABLE OF CONTENTS

ABSTRACT

Optical microscopy imaging of single molecules and single particles is an essential method for studying fundamental biological and chemical processes at the molecular and nanometer scale. The best spatial resolution ($\sim \lambda/2$) achievable in traditional optical microscopy is governed by the diffraction of light. However, single molecule-based super-localization and super-resolution microscopy imaging techniques have emerged in the past decade. Individual molecules can be localized with nanometer scale accuracy and precision for studying of biological and chemical processes.

The obtained spatial resolution for plant cell imaging is not yet as good as that achieved in mammalian cell imaging. Numerous technical challenges, including the generally high fluorescence background due to significant autofluorescence of endogenous components, and the presence of the cell wall (> 250 nm thickness) limit the potential of super-resolution imaging in studying the cellular processes in plants. Here variable-angle epi-fluorescence microscopy (VAEM) was combined with localization based super-resolution imaging, direct stochastic optical reconstruction microscopy (dSTORM), to demonstrate imaging of cortical microtubule (CMT) network in the *Arabidopsis thaliana* root cells with 20 – 40 nm spatial resolution for the first time. With such high spatial resolution, the subcellular organizations of CMTs within single cells, and different cells in many regions along the root, were analyzed quantitatively.

Nearly all of these technical advances in super-localization and super-resolution microscopy imaging were originally developed for biological studies. More recently, however, efforts in super-resolution chemical imaging started to gain momentum. New

discoveries that were previously unattainable with conventional diffraction-limited techniques have been made, such as a) super-resolution mapping of catalytic reactions on single nanocatalysts and b) mechanistic insight into protein ion-exchange adsorptive separations. Furthermore, single molecules and single particles were localized with nanometer precision for resolving the dynamic behavior of single molecules in porous materials. This work uncovered the heterogeneous properties of the pore structures. In this dissertation, the coupling of molecular transport and catalytic reaction at the single molecule and single particle level in multilayer mesoporous nanocatalysts was elucidated. Most previous studies dealt with these two important phenomena separately. A fluorogenic oxidation reaction of non-fluorescent amplex red to highly fluorescent resorufin was tested. The diffusion behavior of single resorufin molecules in aligned nanopores was studied using total internal reflection fluorescence microscopy (TIRFM).

To fully understand the working mechanisms of biological processes such as stepping of motor proteins requires resolving both the translational movement and the rotational motions of biological molecules or molecular complexes. Nanoparticle optical probes have been widely used to study biological processes such as membrane diffusion, endocytosis, and so on. The greatly enhanced absorption and scattering cross sections at the surface plasmon resonance (SPR) wavelength make nanoparticles an ideal probe for high precision tracking. Furthermore, gold nanorods (AuNRs) were used for resolving orientation changes in all three dimensions. The translational and rotational motions of AuNRs in glycerol solutions were tracked with fast imaging rate up to 500 frames per second (fps) in reflected light sheet microscopy (RLSM). The effect of imaging rates on resolving details of single AuNR motions was studied.

ABSTRACT

Optical microscopy imaging of single molecules and single particles is an essential method for studying fundamental biological and chemical processes at the molecular and nanometer scale. The best spatial resolution ($\sim \lambda/2$) achievable in traditional optical microscopy is governed by the diffraction of light. However, single molecule-based super-localization and super-resolution microscopy imaging techniques have emerged in the past decade. Individual molecules can be localized with nanometer scale accuracy and precision for studying of biological and chemical processes.

The obtained spatial resolution for plant cell imaging is not yet as good as that achieved in mammalian cell imaging. Numerous technical challenges, including the generally high fluorescence background due to significant autofluorescence of endogenous components, and the presence of the cell wall (> 250 nm thickness) limit the potential of super-resolution imaging in studying the cellular processes in plants. Here variable-angle epi-fluorescence microscopy (VAEM) was combined with localization based super-resolution imaging, direct stochastic optical reconstruction microscopy (dSTORM), to demonstrate imaging of cortical microtubule (CMT) network in the *Arabidopsis thaliana* root cells with 20 – 40 nm spatial resolution for the first time. With such high spatial resolution, the subcellular organizations of CMTs within single cells, and different cells in many regions along the root, were analyzed quantitatively.

Nearly all of these technical advances in super-localization and super-resolution microscopy imaging were originally developed for biological studies. More recently, however, efforts in super-resolution chemical imaging started to gain momentum. New

discoveries that were previously unattainable with conventional diffraction-limited techniques have been made, such as a) super-resolution mapping of catalytic reactions on single nanocatalysts and b) mechanistic insight into protein ion-exchange adsorptive separations. Furthermore, single molecules and single particles were localized with nanometer precision for resolving the dynamic behavior of single molecules in porous materials. This work uncovered the heterogeneous properties of the pore structures. In this dissertation, the coupling of molecular transport and catalytic reaction at the single molecule and single particle level in multilayer mesoporous nanocatalysts was elucidated. Most previous studies dealt with these two important phenomena separately. A fluorogenic oxidation reaction of non-fluorescent amplex red to highly fluorescent resorufin was tested. The diffusion behavior of single resorufin molecules in aligned nanopores was studied using total internal reflection fluorescence microscopy (TIRFM).

To fully understand the working mechanisms of biological processes such as stepping of motor proteins requires resolving both the translational movement and the rotational motions of biological molecules or molecular complexes. Nanoparticle optical probes have been widely used to study biological processes such as membrane diffusion, endocytosis, and so on. The greatly enhanced absorption and scattering cross sections at the surface plasmon resonance (SPR) wavelength make nanoparticles an ideal probe for high precision tracking. Furthermore, gold nanorods (AuNRs) were used for resolving orientation changes in all three dimensions. The translational and rotational motions of AuNRs in glycerol solutions were tracked with fast imaging rate up to 500 frames per second (fps) in reflected light sheet microscopy (RLSM). The effect of imaging rates on resolving details of single AuNR motions was studied.

CHAPTER 1: GENERAL INTRODUCTION

Dissertation Organization

This dissertation starts with a general introduction about super-localization and super-resolution microscopy, including introduction, recent advances in instruments, recent applications of super-localization and super-resolution fluorescence microscopy, three-dimensional (3D) orientation and rotational tracking of nanoparticles. The following chapters focus on three research areas: a) super-resolution imaging of microtubule structure in plants, b) chemical catalysis at single molecule level, c) orientation and rotational tracking of nanoparticles. Each chapters are arranged in such a way that published papers be submitted for scientific peer-review.

The second chapter demonstrates combining variable angle epi-fluorescence microscopy (VAEM) with a localization based super-resolution imaging method, direct stochastic optical reconstruction microscopy (dSTORM), for resolving the cortical microtubule (CMT) network in *Arabidopsis thaliana* root cells with sub-50-nm spatial resolution. Highly diverse spatial organizations of CMT networks in plant cells at different development stages are resolved and analyzed quantitatively.

Chapter 3 describes our study on the molecular transport in nanopores, catalytic reactions on nanocatalysts, and their coupling at the single molecule and single particle level in total internal reflection fluorescence microscopy (TIRFM). The life cycle of a fluorescent product molecule in a core-shell mesoporous nanocatalyst, including generation, diffusion within nanopores, and escapes from the nanopore and evanescent field (EF) was tracked and studied with sub-10-nm precision in TIRFM.

Chapter 4 reports studies of translational and rotational diffusion of gold nanorods (AuNRs) in aqueous solutions of high viscosity. Reflected light sheet scattering microscopy with orthogonal alignment to the axial direction of the detection objective and sub-micrometer illumination thickness was used to eliminate scattering background. Bifocal images without angular degeneracy were used for achieving simultaneously tracking the locations and orientation changes of AuNRs. Fast imaging speed up to 500 frames per second (fps) was used to reveal fast rotational behaviors of AuNRs.

The final chapter (chapter 5) summarizes the work and indicates potential directions for future research.

Introduction

Nowadays, microscopes are used by researchers in different fields to uncover tiny things beyond the capability of our bare eyes. Extraordinary discovery takes place every day with the aid of microscopes. Optical, electron, and scanning probe microscopy[1-3] are recognized as the three main micro-imaging methods in modern research. While one is often overwhelmed by the complexity of today's advanced optical microscopes, it is surprising how simple but also how brilliant the first compound microscope (a combination of few lenses) was.[4]

The performance of perfect optics (no spherical or achromatic aberrations) is limited by the physical barrier known as the diffraction limit of light. Objects smaller than the diffraction limit cannot be resolved in conventional optical microscopes. The maximum resolution available in theory was first calculated and predicted by the mathematician and physicist Ernst Abbe, who was the second owner of the enterprise

invented by the German mechanic Carl Zeiss. The original formula is present as the following:

$$d = \frac{1.22\lambda}{NA_{cond} + NA_{obj}}$$

where d is the minimum distance of separation for two objects to be resolved, λ is the wavelength of light, and NA_{cond} and NA_{obj} stands for the numerical aperture of the condenser and the objective, respectively. The numerical aperture $NA = n \cdot \sin(\alpha)$, where n is the refractive index of the immersion medium used between the objective and the object and α is the opening angle of the objective. The factor 1.22 is related to the Rayleigh criterion.

Two types of optical imaging techniques: total internal reflection fluorescence microscopy (TIRFM) and light sheet microscopy (LSM), were used for the majority of studies in this dissertation. In both methods, the samples were excited with a well-confined illumination volume, thus significantly reducing the out-of-focus background from fluorescence or scattering.

TIRFM (Fig. 1c) is arguably the most successful mode of fluorescence microscopy for studies of molecular dynamics, including diffusion[5-7] and absorption[8,9] at liquid/solid interfaces. Under TIR illumination the incident angle of light is varied upon a medium with a high index of refraction (n_1). At angles beyond the critical angle, the incident light is completely reflected. An evanescent field (EF) of the same characteristic as the reflected light is created in the adjacent medium (n_2), which must have a lower index of refraction than n_1. The intensity of the EF decays exponentially from the interface of the two media. This characteristic of EF enables the excitation of only objects within a few hundred nanometers from the surface. Thus the out-of-focus fluorescence

background is essentially eliminated. A comprehensive review of TIRFM is available in Axelrod's publication in 2008.[10]

The concept of illuminating thick samples with a thin sheet of light aligned with the focal plane of the recording objective has led to the development of a whole family of LSM techniques[11-15] in the past 20 years. Because only a thin layer of sample is illuminated by the light sheet, these techniques effectively reduce the background noise and sample photodegradation. Moreover, LSM is capable of 3D volume imaging when combined with a piezo stage for axial sectioning. LSM is an excellent choice for imaging thick samples. Though LSM is mostly used for fluorescence imaging of biological processes, one chapter in the dissertation focuses on LSM imaging of nanoparticles in solution.

Recent Advances in Instrumentation

Automated Prism-Based TIRFM. There are two basic types of TIRFM systems distinguished by the optics used for producing TIR. In objective-based TIRFM (Fig. 1c) the excitation beam is directed into a high *NA* objective off-center in order to encounter the solid/liquid interface, usually between a coverslip and aqueous solution, with an incident angle larger than the critical angle. The excitation beam is completely reflected back into the objective. The emission signal is collected by the same objective and then focused onto the signal recorder (i.e. camera) by a tube lens. The other type of TIRFM system is prism based. The illumination light is directed through a prism on which the sample lies. TIR also occurs at the solid/liquid interface, and the emission signal is collected by an objective on the other side of the interface. Many variations of

configurations for both type of TIRFM are available and have been discussed in other reviews.[10]

Both types of TIRFM systems have their own advantages. The objective-based TIRFM has become a standard module for commercial light microscopes. The main drawbacks of this type of TIRFM include the background from the scattered excitation light within the objective, the difficulty in determining the exact incident angle, and the limitation on the achievable range of incident angle due to the geometry of the objective. This can negatively influence the detection sensitivity and the axial localization accuracy of fluorescent probes.

All of these drawbacks are avoided in prism type TIRFM. However, the performance of prism-type TIRFM system strongly relies on achieving ideal illumination conditions at different incident angles with high accuracy. A time-consuming calibration process is often necessary to accomplish the goal.

To fully harvest the benefits of using prism-type TIRFM, a dual-color auto-calibrated scanning-angle (SA) TIRFM setup with an optimized system layout and an automatic high-precision calibration procedure had been demonstrated in our laboratory. A computer program developed in-house is used to calibrate the incident angles in the full range with an interval as small as ~0.1°.[16,17] The entire auto-calibration procedure can be finished within minutes. With this setup, localization of fluorescent beads in gels had been determined with nanometer precision in the axial direction.[16] This unique *automated* SA-TIRFM has also been employed for high-precision 3D tracking of non-blinking quantum dots.[18]

Variable-angle Epi-fluorescence Microscopy (VAEM). The EF provides a shallow illumination depth of a few hundred nanometers from the interface. Therefore, it essentially eliminates out-of-focus fluorescence background. TIRFM has been widely used for the purpose of improving the detection sensitivity. However, the limited illumination depth in TIRFM is not suitable for imaging large, thick samples. To overcome this limitation, the incident angle of illumination beam is operated at subcritical angles that are smaller than but yet very close to the critical angle. This illumination strategy was given names under variable-angle epi-fluorescence microscopy (VAEM),[19] also known as highly inclined thin illumination (HILO) microscopy,[20] or simply pseudo-TIRFM (Fig. 1b,d).[17] The effective excitation depth can be extended a few tens of micrometers into the sample. However, the excitation volume is still much thinner in VAEM compared to epi-illumination (Fig. 1a). Like in real TIRFM, the small illumination volume reduces the out-of-focus excitation thus achieving higher detection sensitivity. In VAEM, the sample is actually illuminated by light with title angles. Therefore, the thickness of excitation volume grows as the imaging depth increases.

Light sheet microscopy. Light sheet (Fig. 2) is an alternative excellent optical sectioning method beside TRIFM. Although Siedntopf and Zsigmondy published the first version of the light sheet microscope over a century ago,[21] the concept was not truly expanded upon until the early 1990s. The first modern LSM called orthogonal-plane fluorescence optical sectioning (OPFOS) used a beam 30 μm thick at the waist to section a sample that was placed in a rotatable holder.[13] Since the emergence of optical sectioning, LSM has seen a profound growth in application and variability. LSM is commonly used for tissue imaging. New variations have now achieved super-resolution

within single cells, making LSM one of the fastest growing and most powerful imaging techniques in biologically relevant microscopy today. Convenient innovations such as objective-coupled planar illumination (OCPI)[22,23] and inverted selective plane illumination microscopy (iSPIM)[24] are accessible additions to standard microscopes. The versatility and customization that is intrinsic to the light sheet tomography techniques allow for current and future investigators to pick and choose necessary and preferred components for their own work.[12] However, most of the current LSM techniques utilize microscope objectives with long working distance and low NA. Therefore the excitation volume is relatively large and it is not optimal for single molecule detection. More recently, reflected LSM (RLSM) had been demonstrated and used for imaging single molecules with high signal to noise ratio (SNR) in nucleus of mammalian cells.[25,26]

Super-resolution Fluorescence Microscopy. Fluorescence microscopy is commonly used in biological studies. However, conventional techniques suffer a significant drawback, that is, the diffraction limit of light. (See equation 1). Breaking this diffraction limit has become a seemingly insurmountable challenge. However, during the past two decades the emergence of super-resolution imaging techniques (Fig. 3), including stimulated emission depletion (STED) microscopy,[27-30] structured illumination microscopy (SIM),[31,32] stochastic optical reconstruction microscopy (STORM)[33] also known as photoactivated localization microscopy (PALM)[34] or fluorescence photoactivation microscopy (FPALM),[35] enabled diffraction-unlimited imaging using the same diffraction-limited far-field optics as in conventional fluorescence microscopy. Depend on how the fluorophores are modulated, these super-resolution imaging techniques can be divided into two approaches: SIM/STED use illumination light patterns

to spatially address the modulation, whereas STORM/PALM/FPALM rely on the stochastic nature of single- molecule switching. In STORM/PALM/FPALM photoactivatible fluorophores are switched randomly between a fluorescent state (on-state) and a dark state (off- state) or any other form that is non-fluorescent at the same wavelength. Subsets of fluorophores are isolated and their positions are localized by fitting the intensity distributions of images from a single fluorophore with a point spread function (PSF) or with a Gaussian function as a close estimate. The enhancement of the spatial resolution using these techniques depends on the precision with which individual fluorescent molecules can be localized. While the principle underneath this approach of super-resolution microscopy is essentially the same, differences exist. STORM utilizes organic dyes as fluorescent probes rather than fluorescent proteins, and generates images with better spatial resolution due to more collected emission photons during each switching cycle. However, the results also largely depend on the accuracy of tedious immunostaining processes. On the other hand, such drawbacks are avoided in PALM/FPALM since the photoactivatable fluorescent proteins are genetically expressed in cells.

Fundamentally, fluorescence images are composed of coordinates of fluorescent probes. Two probes with a separation distance smaller than the diffraction limit (a few hundred nanometers) can no longer be resolved in conventional fluorescence images. Though shapes and sizes of molecules cannot be determined using conventional fluorescence microscopy, the centroids of individual fluorescent molecules can be localized with high precision by fitting the fluorescence intensity distribution. The localization precision, in brief, is inversely proportional to the square root of photons

($\sqrt{N}$) collected from a single fluorescent molecule.[36,37] For example, molecules emitting several thousand photons can be localized with nanometer precision under this standard. Combined with the stochastic switching properties, the shape of a photoswitchable fluorescent probe can be rendered as the distribution of positions within nanoscale areas. Lots of these positions can then be used to reconstruct the structure of interest with a resolution beyond the diffraction limit.

Though there are many applications based on localizing the molecular or particle positions with nanometer accuracy, the majority of the work in this dissertation focuses on studying biological structures, chemical reactions and molecular motions.

Recent Applications of Localization-based Super-resolution Fluorescence Microscopy

Imaging biological processes. Almost all the super-resolution imaging techniques were originally developed for biological studies. In the aspect of STORM/PALM/FPALM, they were first used to resolve simple biological structures[33-35] such as nearby fluorescent probes separated by 135 base pairs on DNA strands (~46 nm). Later on, more complicated systems such as the cellular network (microtubule and actin network) and subcellular organelle (for example mitochondrion), and their colocalization were also well studied using multi-color super-resolution imaging microscopy.[38] 3D super-resolution microscopy resolves biological structure with nanometer resolution in all three dimensions[39,40] shortly after the emergence of these techniques. Early localization-based super-resolution imaging techniques require a long-term imaging collection process. Therefore, fast dynamic information of many biological processes is not

available due to the slow temporal resolution. Nevertheless, advances in mechanic capabilities[41] (faster imaging rate with more advanced camera), performance of fluorescent probes[42] (faster switching rates from newly developed fluorescent protein molecules or synthesized dyes), and mathematic algorithm modifications[43] have already and will continue to help scientists to look at dynamic processes at video rates.

Nearly all of these advances in super-resolution imaging were performed with mammalian cells. Very few reports exist of the study of cellular structures with such high resolution in plant samples due to numerous technical challenges,[44] including the generally high fluorescence background due to significant autofluorescence of endogenous components, and the presence of the cell wall (> 250 nm thickness). The former leads to low signal to noise ratio (S/N) for single molecule detection and therefore low localization accuracy and low spatial resolution. The latter contributes to a higher background due to additional layers with mismatched refractive indices (causing more severe scattering and spherical aberration) and restricts the use of TIR illumination. Nevertheless, several super-resolution imaging techniques have been tested for imaging plant samples. The structure of perinuclear actin in live tobacco cells was visualized with a lateral resolution of 50 nm by combining PALM imaging with optical sectioning.[45] The organization of cellulose microfibrils on the outer side of the cell wall in live onion epidermal cells has been studied by STORM imaging with a lateral resolution of 100 nm.[46] Structured illumination microscopy, which uses specially designed illumination patterns to spatially modulate fluorophores,[32] was used for imaging the dynamics of endoplasmic reticulum, plasmodesmata, and cortical microtubules in live cells with a two-fold improvement in the spatial resolution (~ 100 nm) over traditional fluorescence

microscopy techniques.[47,48] Stimulated emission depletion (STED) microscopy has also been used to measure the size of protein clusters on the lateral plasma membrane of plant cells with a lateral resolution of 70 nm.[49]

Imaging chemical reactions at single turn-over resolution. More recently, super-resolution imaging techniques have brought new discoveries in chemical reactions such as super-resolution mapping of catalytic reactions on single nanocatalysts[50-60] and mechanistic insights into protein ion-exchange adsorptive separations.[61] According to what kinds of fluorescent probes are used, these studies can be divided into two strategies[62] (Fig. 4). In the first strategy, fluorescent probes are involved in the chemical reaction during which the bond forming or breaking happens on the probe molecule to induce a sharp change of fluorescent properties such as fluorescence emission wavelength shifting, fluorescence quenching. The chemical reaction events are detected when the changes of fluorescent properties happen. In the other type, the fluorescent probes work as a spectators which do not change their chemical structures during the reaction processes. The chemical reaction is detected by the change of locations of fluorescent probes (for example, association-dissociation with reagents on surface) indicating the presence of target reagents. However, fluorescent properties of probes such as color, intensity, and lifetime may also change. Usually, the chemical reaction rate at the single particle level is slow and the particle density f on the sample slide is small, so individual events can be identified both temporally and spatially. All of these advanced studies prove the potential to study chemical reactions at the temporary resolution of single turn-over and the spatial resolution of nanometers

Characterize the heterogeneous inner structure of porous nanomaterials with nanometer resolution. Advances in super-localization based imaging methods are used for single particle, single molecule tracking. Motions of single fluorescent molecules have been tracked with one-nanometer precision (FIONA).[63] FIONA was successfully used to resolve the hand-over-hand walking mechanism of kinesin and dynein motor proteins on microtubules.[64,65] Efforts in studying other types of mechanically biological processes were also made using the same method.[66] More recently, single molecule tracking methods were used to visualize the porous networks, interconnectivities of channels and diverse diffusion behaviors of molecules in host-guest system (Fig. 5).[67-70] The pore size of these channels is only few nanometers in diameter. Therefore it is critical that molecular positions of fluorescent probes are localized with nanometer precision in order to reveal the heterogeneity of inner structures in the porous material.

Three-dimensional Orientation and Rotational Tracking of Nanoparticles

Many biological activities, such as DNA polymerization,[71] stepping of motor protein,[64,72] self-rotation of ATP synthase,[73] involve motions of sub-micrometer scale. To fully understand the fine mechanisms of these biological events requires not only visualizing the translational movement but also uncovering the rotational motions. For deciphering the rotational motion of biological molecules, fluorescence polarization spectroscopy[72,74,75] is commonly used taking the advantage of coupling the interaction of polarized excitation with well-defined dipole of fluorescent probes and splitting anisotropy emissions from the dipole orthogonally.

Anisotropic gold nanoparticles of excellent optical and chemical stability[76-79] are widely used for orientation and rotational tracking. A few techniques (Fig. 6) have been developed to resolve the orientation angles of gold nanorods (AuNRs) in the focal plane including dark-field (DF) polarization microscopy,[80] photothermal heterodyne imaging (PHI),[81,82] and differential interference contrast (DIC) microscopy.[83-87] These imaging methods have been well demonstrated to decipher the in-plane angle of AuNRs either simply on a coverslip or in live cell. However, the out-of-plane angle is either unavailable (PHI) or ambiguous because of low angular resolution (DF, DIC). Furthermore, the angular degeneracy resulting from the symmetric cylindrical shape of AuNRs limits their abilities to differentiate the orientation of nanorods in the four quadrants of the Cartesian coordinate system.

Another method called defocused orientation and position imaging (DOPI)[88,89] has been developed to determine the 3D orientation of a tilted single dipole in a single image frame without angular detergency. The core idea is essentially based on electron transition dipole approximation and the fact that the dipole emission exhibits an angular anisotropy. Therefore, the direct detection of the spatial distribution of the scattered or emitted field of single dipoles becomes possible when deliberately applying an aberration (defocusing) in the imaging system. It often requires switching back and forth between defocused and focused imaging for more precise position and orientation determination in DOPI. Because of this limitation, DOPI is more suitable to study the angular information of stationary probes.

A method called focused orientation and position imaging (FOPI) was previously demonstrated, which overcame the drawbacks of both polarization based in-focus

imaging methods or the DOPI method.[84] The core idea is coupling the effects of the supporting substrate (a gold film in this case) with the far-field scattering patterns of plasmonic nanoparticles. The in-focus imaging pattern is used to resolve the absolute 3D orientation of tilted AuNRs (within 15 nm from the substrate) with high signal to noise ratio. Nevertheless, the necessary interaction between the AuNRs and gold film substrate limits its potential applications.

A dual-color total internal reflection scattering (TIRS) imaging method was also developed to determine the 3D orientation angles of AuNRs on lipid membranes. Combining with super-resolution mapping locations of AuNRs, it reveals in-plane rotational motions without angular degeneracy. This technique has been used to characterize distinct binding patterns of AuNRs on the synthetic lipid membrane. Because of the exponential decay of intensity in EF of TIRS, it is mainly used to determine rotational motions of AuNRs within a thin layer on the substrate surface.

Dissertation Focus

This dissertation focuses mainly on applying single molecule localization-based fluorescence microscopy for tissue imaging and chemical imaging, and developing reflected light sheet scattering microscopy for particle tracking. These studies can be separated in three directions: a) STORM imaging under the VAEM illumination scheme to resolve the microtubule network in cells of intact root sample with sub-50-nm spatial resolution. Details of microtubule organization were therefore uncovered and quantified. The variations of microtubule organization at different cellular developmental stages were correlated with their growing activities. b) Studying mass transport and chemical

reaction in nanopore environment with a 3D multilayer mesoporous catalyst. This part of work sets up the platform for systematic investigations to understand how factors, including size, structure, and molecular transport, affecting the catalytic properties and efficiency. c) Developing reflected light sheet scattering microscopy. Translational and rotational motions of gold nanorods were tracked simultaneously. 3D orientation changes of gold nanorods were revealed at the same time in a home-built dual-view imaging system.

References:

1 Davidson, M. W. & Abramowitz, M. in *Encyclopedia of Imaging Science and Technology* (John Wiley & Sons, Inc., 2002).

2 Kalinin, S. G., A. Scanning Probe Microscopy. *Springer-Verlag New York* (2007).

3 Williams, D. & Carter, C. B. in *Transmission Electron Microscopy* Ch. 1, 3-17 (Springer US, 1996).

4 Kapitza, H. G. Microscopy from the very beginning. *In Zeiss, Ed* (1997).

5 Xu, X.-H. & Yeung, E. S. Direct Measurement of Single-Molecule Diffusion and Photodecomposition in Free Solution. *Science* **275**, 1106-1109 (1997).

6 Xu, X.-H. N. & Yeung, E. S. Long-Range Electrostatic Trapping of Single-Protein Molecules at a Liquid-Solid Interface. *Science* **281**, 1650-1653 (1998).

7 He, Y., Li, H. W. & Yeung, E. S. Motion of single DNA molecules at a liquid-solid interface as revealed by variable-angle evanescent-field microscopy. *J. Phys. Chem. B* **109**, 8820-8832 (2005).

8 Kang, S. H. & Yeung, E. S. Dynamics of Single-Protein Molecules at a Liquid/Solid Interface: Implications in Capillary Electrophoresis and Chromatography. *Anal. Chem.* **74**, 6334-6339 (2002).

9 Kang, S. H., Shortreed, M. R. & Yeung, E. S. Real-Time Dynamics of Single-DNA Molecules Undergoing Adsorption and Desorption at Liquid-Solid Interfaces. *Anal. Chem.* **73**, 1091-1099 (2001).

10 Axelrod, D. in *Methods in Cell Biology* Vol. Volume 89 (eds J. Correia Dr. John & Dr. H. William Detrich, III) 169-221 (Academic Press, 2008).

11 Huisken, J., Swoger, J., Del Bene, F., Wittbrodt, J. & Stelzer, E. H. K. Optical Sectioning Deep Inside Live Embryos by Selective Plane Illumination Microscopy. *Science* **305**, 1007-1009 (2004).

12 Greger, K., Swoger, J. & Stelzer, E. H. K. Basic building units and properties of a fluorescence single plane illumination microscope. *Rev. Sci. Instrum.* **78**, 023705 (2007).

13 Voie, A. H., Burns, D. H. & Spelman, F. A. Orthogonal-plane fluorescence optical sectioning: Three-dimensional imaging of macroscopic biological specimens. *J. Microsc-Oxford* **170**, 229-236 (1993).

14 Keller, P. J., Schmidt, A. D., Wittbrodt, J. & Stelzer, E. H. K. Reconstruction of Zebrafish Early Embryonic Development by Scanned Light Sheet Microscopy. *Science* **322**, 1065-1069 (2008).

15 Stender, A. S. *et al.* Single Cell Optical Imaging and Spectroscopy. *Chem. Rev.* **113**, 2469-2527 (2013).

16 Sun, W., Marchuk, K., Wang, G. F. & Fang, N. Autocalibrated Scanning-Angle Prism-Type Total Internal Reflection Fluorescence Microscopy for Nanometer-Precision Axial Position Determination. *Anal. Chem.* **82**, 2441-2447 (2010).

17 Sun, W., Xu, A., Marchuk, K., Wang, G. & Fang, N. Whole-Cell Scan Using Automatic Variable-Angle and Variable-Illumination-Depth Pseudo-Total Internal Reflection Fluorescence Microscopy. *J. Lab. Autom.* **16**, 255-262 (2011).

18 Marchuk, K., Guo, Y., Sun, W., Vela, J. & Fang, N. High-Precision Tracking with Non-blinking Quantum Dots Resolves Nanoscale Vertical Displacement. *J. Am. Chem. Soc.* **134**, 6108-6111 (2012).

19 Konopka, C. A. & Bednarek, S. Y. Variable-angle epifluorescence microscopy: a new way to look at protein dynamics in the plant cell cortex. *Plant J.* **53**, 186-196 (2008).

20 Tokunaga, M., Imamoto, N. & Sakata-Sogawa, K. Highly inclined thin illumination enables clear single-molecule imaging in cells. *Nat. Methods* **5**, 159-161 (2008).

21 Siedentopf, H. & Zsigmondy, R. Uber Sichtbarmachung und Größenbestimmung ultramikoskopischer Teilchen, mit besonderer Anwendung auf Goldrubingläser. *Ann. Phys.* **315**, 1-39 (1902).

22 Holekamp, T. F., Turaga, D. & Holy, T. E. Fast Three-Dimensional Fluorescence Imaging of Activity in Neural Populations by Objective-Coupled Planar Illumination Microscopy. *Neuron* **57**, 661-672 (2008).

23 Turaga, D. & Holy, T. E. Miniaturization and defocus correction for objective-coupled planar illumination microscopy. *Opt. Lett.* **33**, 2302-2304 (2008).

24 Wu, Y. *et al.* Inverted selective plane illumination microscopy (iSPIM) enables coupled cell identity lineaging and neurodevelopmental imaging in Caenorhabditis elegans. *Proc. Natl. Acad. Sci. U. S. A.* **108**, 17708-17713 (2011).

25 Gebhardt, J. C. M. *et al.* Single-molecule imaging of transcription factor binding to DNA in live mammalian cells. *Nat. Meth.* **10**, 421-426 (2013).

26 Zhao, Z. W. *et al.* Spatial organization of RNA polymerase II inside a mammalian cell nucleus revealed by reflected light-sheet superresolution microscopy. *Proc. Natl. Acad. Sci. U. S. A.* **111**, 681-686 (2014).

27 Hell, S. W. & Wichmann, J. Breaking the diffraction resolution limit by stimulated emission: stimulated-emission-depletion fluorescence microscopy. *Opt. Lett.* **19**, 780-782 (1994).

28 Klar, T. A. & Hell, S. W. Subdiffraction resolution in far-field fluorescence microscopy. *Opt. Lett.* **24**, 954-956 (1999).

29 Hell, S. W. Far-Field Optical Nanoscopy. *Science* **316**, 1153-1158 (2007).

30 Hein, B., Willig, K. I. & Hell, S. W. Stimulated emission depletion (STED) nanoscopy of a fluorescent protein-labeled organelle inside a living cell. *Proc. Natl. Acad. Sci. U. S. A.* **105**, 14271-14276 (2008).

31 Kner, P., Chhun, B. B., Griffis, E. R., Winoto, L. & Gustafsson, M. G. L. Super-resolution video microscopy of live cells by structured illumination. *Nat. Meth.* **6**, 339-342 (2009).

32 Gustafsson, M. G. L. Nonlinear structured-illumination microscopy: Wide-field fluorescence imaging with theoretically unlimited resolution. *Proc. Natl. Acad. Sci. U. S. A.* **102**, 13081-13086 (2005).

33 Rust, M. J., Bates, M. & Zhuang, X. Sub-diffraction-limit imaging by stochastic optical reconstruction microscopy (STORM). *Nat. Meth.* **3**, 793-796 (2006).

34 Betzig, E. *et al.* Imaging Intracellular Fluorescent Proteins at Nanometer Resolution. *Science* **313**, 1642-1645 (2006).

35 Hess, S. T., Girirajan, T. P. K. & Mason, M. D. Ultra-High Resolution Imaging by Fluorescence Photoactivation Localization Microscopy. *Biophys. J.* **91**, 4258-4272 (2006).

36 Thompson, R. E., Larson, D. R. & Webb, W. W. Precise Nanometer Localization Analysis for Individual Fluorescent Probes. *Biophys. J.* **82**, 2775-2783 (2002).

37 Ober, R. J., Ram, S. & Ward, E. S. Localization Accuracy in Single-Molecule Microscopy. *Biophys. J.* **86**, 1185-1200 (2004).

38 Bates, M., Huang, B., Dempsey, G. T. & Zhuang, X. Multicolor Super-Resolution Imaging with Photo-Switchable Fluorescent Probes. *Science* **317**, 1749-1753 (2007).

39 Huang, B., Wang, W., Bates, M. & Zhuang, X. Three-Dimensional Super-Resolution Imaging by Stochastic Optical Reconstruction Microscopy. *Science* **319**, 810-813 (2008).

40 Huang, B., Babcock, H. & Zhuang, X. Breaking the Diffraction Barrier: Super-Resolution Imaging of Cells. *Cell* **143**, 1047-1058 (2010).

41 van de Linde, S. *et al.* Direct stochastic optical reconstruction microscopy with standard fluorescent probes. *Nat. Protoc.* **6**, 991-1009 (2011).

42 McKinney, S. A., Murphy, C. S., Hazelwood, K. L., Davidson, M. W. & Looger, L. L. A bright and photostable photoconvertible fluorescent protein. *Nat. Meth.* **6**, 131-133 (2009).

43 Parthasarathy, R. Rapid, accurate particle tracking by calculation of radial symmetry centers. *Nat. Meth.* **9**, 724-726 (2012).

44 Ehrhardt, D. W. & Frommer, W. B. New Technologies for 21st Century Plant Science. *Plant Cell* **24**, 374-394 (2012).

45 Durst, S. *et al.* Organization of perinuclear actin in live tobacco cells observed by PALM with optical sectioning. *J. Plant Physiol.* **171**, 97-108 (2014).

46 Liesche, J., Ziomkiewicz, I. & Schulz, A. Super-resolution imaging with Pontamine Fast Scarlet 4BS enables direct visualization of cellulose orientation and cell connection architecture in onion epidermis cells. *BMC Plant Biol.* **13**, 226 (2013).

47 Fitzgibbon, J., Bell, K., King, E. & Oparka, K. Super-Resolution Imaging of Plasmodesmata Using Three-Dimensional Structured Illumination Microscopy. *Plant Physiol.* **153**, 1453-1463 (2010).

48 Komis, G. *et al.* Dynamics and Organization of Cortical Microtubules as Revealed by Superresolution Structured Illumination Microscopy. *Plant Physiol.* **165**, 129-148 (2014).

49 Kleine-Vehn, J. *et al.* Recycling, clustering, and endocytosis jointly maintain PIN auxin carrier polarity at the plasma membrane. *Mol. Sys. Biol.* **7**, 540-540 (2011).

50 Roeffaers, M. B. J. *et al.* Spatially resolved observation of crystal-face-dependent catalysis by single turnover counting. *Nature* **439**, 572-575 (2006).

51 De Cremer, G., Sels, B. F., De Vos, D. E., Hofkens, J. & Roeffaers, M. B. J. Fluorescence micro(spectro)scopy as a tool to study catalytic materials in action. *Chem. Soc. Rev.* **39**, 4703-4717 (2010).

52 Chen, P. *et al.* Single-molecule fluorescence imaging of nanocatalytic processes. *Chem. Soc. Rev.* **39**, 4560-4570 (2010).

53 Xu, W., Jain, P. K., Beberwyck, B. J. & Alivisatos, A. P. Probing Redox Photocatalysis of Trapped Electrons and Holes on Single Sb-doped Titania Nanorod Surfaces. *J. Am. Chem. Soc.* **134**, 3946-3949 (2012).

54 Han, K. S., Liu, G., Zhou, X., Medina, R. E. & Chen, P. How Does a Single Pt Nanocatalyst Behave in Two Different Reactions? A Single-Molecule Study. *Nano Lett.* **12**, 1253-1259 (2012).

55 Ha, J. W. *et al.* Super-Resolution Mapping of Photogenerated Electron and Hole Separation in Single Metal–Semiconductor Nanocatalysts. *J. Am. Chem. Soc.* **136**, 1398-1408 (2014).

56 Tachikawa, T., Yonezawa, T. & Majima, T. Super-Resolution Mapping of Reactive Sites on Titania-Based Nanoparticles with Water-Soluble Fluorogenic Probes. *ACS Nano* **7**, 263-275 (2012).

57 Roeffaers, M. B. J. *et al.* Super-Resolution Reactivity Mapping of Nanostructured Catalyst Particles. *Angew. Chem. Int. Edit.* **48**, 9285-9289 (2009).

58 Blum, S. A. Location change method for imaging chemical reactivity and catalysis with single-molecule and -particle fluorescence microscopy. *Phys. Chem. Chem. Phys.* **16**, 16333-16339 (2014).

59 Zhou, X., Choudhary, E., Andoy, N. M., Zou, N. & Chen, P. Scalable Parallel Screening of Catalyst Activity at the Single-Particle Level and Subdiffraction Resolution. *ACS Catalysis* **3**, 1448-1453 (2013).

60 Xu, W. *et al.* Single-Molecule Electrocatalysis by Single-Walled Carbon Nanotubes. *Nano Lett.* **9**, 3968-3973 (2009).

61 Kisley, L. *et al.* Unified superresolution experiments and stochastic theory provide mechanistic insight into protein ion-exchange adsorptive separations. *Proc. Natl. Acad. Sci. U. S. A.* **111**, 2075-2080 (2014).

62 Cordes, T. & Blum, S. A. Opportunities and challenges in single-molecule and single-particle fluorescence microscopy for mechanistic studies of chemical reactions. *Nat. Chem.* **5**, 993-999 (2013).

63 Yildiz, A. & Selvin, P. R. Fluorescence Imaging with One Nanometer Accuracy: Application to Molecular Motors. *Acc. Chem. Res.* **38**, 574-582 (2005).

64 Kural, C. *et al.* Kinesin and Dynein Move a Peroxisome in Vivo: A Tug-of-War or Coordinated Movement? *Science* **308**, 1469-1472 (2005).

65 Yildiz, A. & Selvin, P. R. Kinesin: walking, crawling or sliding along? *Trends Cell Biol.* **15**, 112-120 (2005).

66 Yildiz, A. *et al.* Myosin V Walks Hand-Over-Hand: Single Fluorophore Imaging with 1.5-nm Localization. *Science* **300**, 2061-2065 (2003).

67 Lebold, T., Michaelis, J. & Brauchle, C. The complexity of mesoporous silica nanomaterials unravelled by single molecule microscopy. *Phys. Chem. Chem. Phys.* **13**, 5017-5033 (2011).

68 Hellriegel, C. *et al.* Diffusion of Single Streptocyanine Molecules in the Nanoporous Network of Sol−Gel Glasses†. *J. Phys. Chem. B* **108**, 14699-14709 (2004).

69 Mabry, J. N., Skaug, M. J. & Schwartz, D. K. Single-Molecule Insights into Retention at a Reversed-Phase Chromatographic Interface. *Anal. Chem.* **86**, 9451-9458 (2014).

70 Christian, H., Johanna, K. & Christoph, B. Tracking of single molecules as a powerful method to characterize diffusivity of organic species in mesoporous materials. *New J. Phys.* **7**, 23 (2005).

71 Waga, S. & Stillman, B. THE DNA REPLICATION FORK IN EUKARYOTIC CELLS. *Annu. Rev. Biochem.* **67**, 721-751 (1998).

72 Forkey, J. N., Quinlan, M. E., Alexander Shaw, M., Corrie, J. E. T. & Goldman, Y. E. Three-dimensional structural dynamics of myosin V by single-molecule fluorescence polarization. *Nature* **422**, 399-404 (2003).

73 Yasuda, R., Noji, H., Yoshida, M., Kinosita, K. & Itoh, H. Resolution of distinct rotational substeps by submillisecond kinetic analysis of F1-ATPase. *Nature* **410**, 898-904 (2001).

74 Khatua, S. *et al.* Micrometer-Scale Translation and Monitoring of Individual Nanocars on Glass. *ACS Nano* **3**, 351-356 (2009).

75 Chung, I., Shimizu, K. T. & Bawendi, M. G. Room temperature measurements of the 3D orientation of single CdSe quantum dots using polarization microscopy. *Proc. Natl. Acad. Sci. U. S. A.* **100**, 405-408 (2003).

76 Wang, G., Stender, A. S., Sun, W. & Fang, N. Optical imaging of non-fluorescent nanoparticle probes in live cells. *Analyst* **135**, 215-221 (2010).

77 West, J. L. & Halas, N. J. Engineered Nanomaterials for Biophotonics Applications: Improving Sensing, Imaging, and Therapeutics. *Annu. Rev. Biomed. Eng.* **5**, 285-292 (2003).

78 Murphy, C. J. *et al.* Gold Nanoparticles in Biology: Beyond Toxicity to Cellular Imaging. *Acc. Chem. Res.* **41**, 1721-1730 (2008).

79 De, M., Ghosh, P. S. & Rotello, V. M. Applications of Nanoparticles in Biology. *Adv. Mater.* **20**, 4225-4241 (2008).

80 Sönnichsen, C. & Alivisatos, A. P. Gold Nanorods as Novel Nonbleaching Plasmon-Based Orientation Sensors for Polarized Single-Particle Microscopy. *Nano Lett.* **5**, 301-304 (2005).

81 Chang, W.-S., Ha, J. W., Slaughter, L. S. & Link, S. Plasmonic nanorod absorbers as orientation sensors. *Proc. Natl. Acad. Sci. U. S. A.* **107**, 2781-2786 (2010).

82 Berciaud, S., Cognet, L., Tamarat, P. & Lounis, B. Observation of Intrinsic Size Effects in the Optical Response of Individual Gold Nanoparticles. *Nano Lett.* **5**, 515-518 (2005).

83 Gu, Y., Sun, W., Wang, G. & Fang, N. Single Particle Orientation and Rotation Tracking Discloses Distinctive Rotational Dynamics of Drug Delivery Vectors on Live Cell Membranes. *J. Am. Chem. Soc.* **133**, 5720-5723 (2011).

84 Ha, J. W., Marchuk, K. & Fang, N. Focused Orientation and Position Imaging (FOPI) of Single Anisotropic Plasmonic Nanoparticles by Total Internal Reflection Scattering Microscopy. *Nano Lett.* **12**, 4282-4288 (2012).

85 Ha, J. W., Sun, W., Stender, A. S. & Fang, N. Dual-Wavelength Detection of Rotational Diffusion of Single Anisotropic Nanocarriers on Live Cell Membranes. *J. Phys. Chem. C* **116**, 2766-2771 (2012).

86 Stender, A. S., Wang, G., Sun, W. & Fang, N. Influence of Gold Nanorod Geometry on Optical Response. *ACS Nano* **4**, 7667-7675 (2010).

87 Wang, G., Sun, W., Luo, Y. & Fang, N. Resolving Rotational Motions of Nano-objects in Engineered Environments and Live Cells with Gold Nanorods and Differential Interference Contrast Microscopy. *J. Am. Chem. Soc.* **132**, 16417-16422 (2010).

88 Li, T. *et al.* Three-Dimensional Orientation Sensors by Defocused Imaging of Gold Nanorods through an Ordinary Wide-Field Microscope. *ACS Nano* **6**, 1268-1277 (2012).

89 Toprak, E. *et al.* Defocused orientation and position imaging (DOPI) of myosin V. *Proc. Natl. Acad. Sci. U. S. A.* **103**, 6495-6499 (2006).

Figures

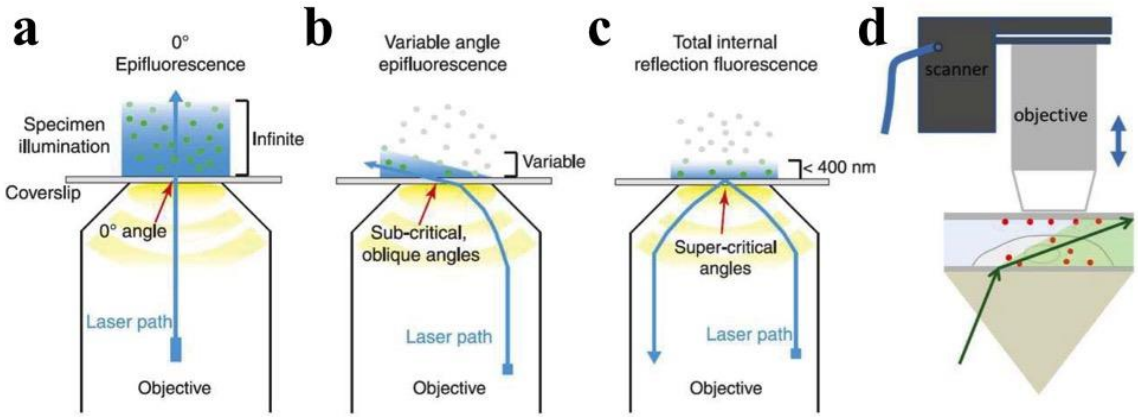

Figure 1. **Various TIRFM and VAEM configurations.** (a) Epi-fluorescence. (b) Objective-based VAEM. (c) Objective-based TIRFM. Adapted with permission from ref 19. Copyright 2008 Blackwell Publishing Ltd. (d) Prism-based VAEM. The objective scanner facilitates vertical sectioning of the sample. Adapted with permission from ref 17. Copyright 2011 Elsevier. The components are not drawn to scale.

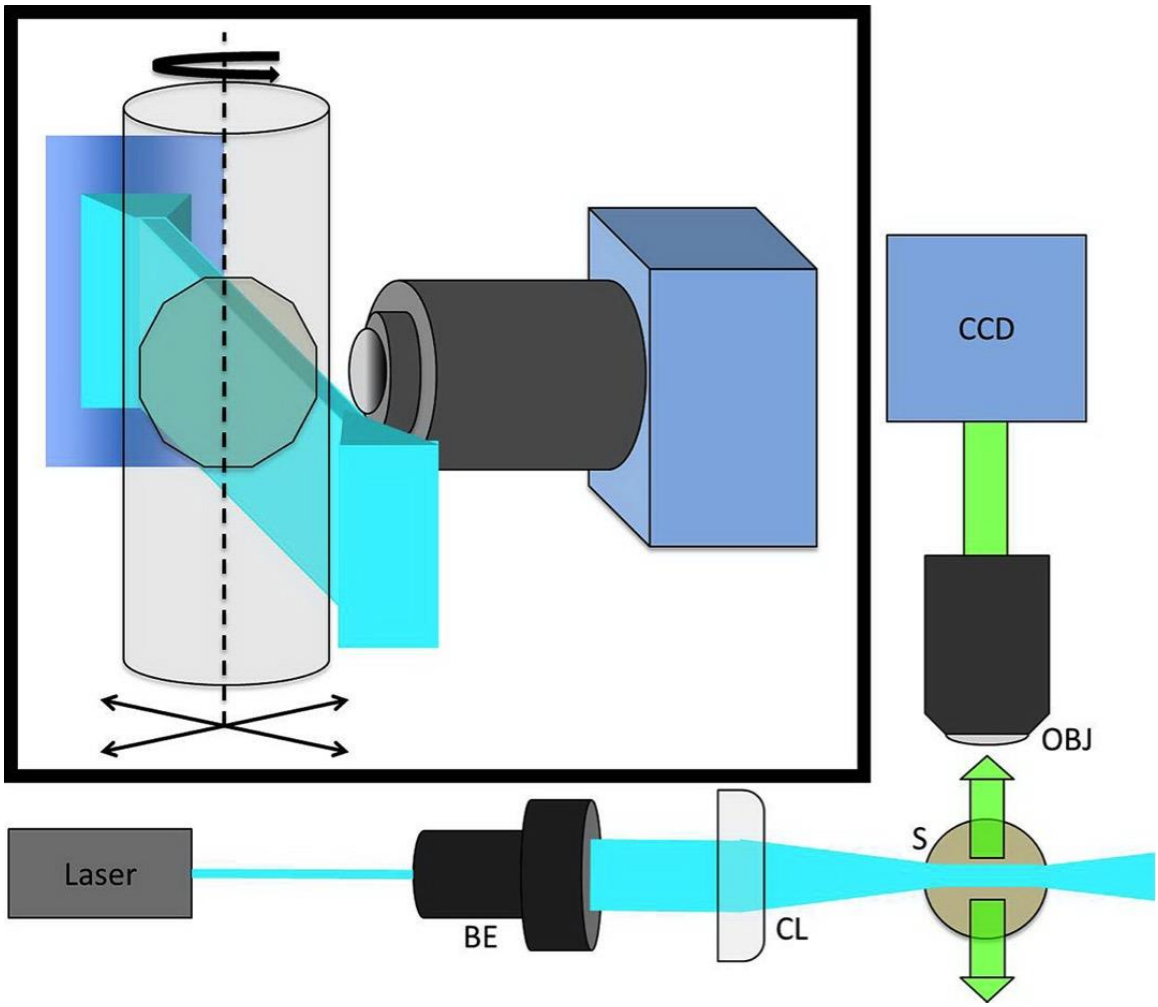

Figure 2. Schematic of a typical LSM. Laser illumination passes through a beam expander (BE), shaped by the cylindrical lens (CL), and passes through the sample (S). Emitted light is collected by the objective (OBJ) and recorded by the camera (CCD). Boxed region is a close-up of the sample holder depicting its degrees of freedom during image acquisition. Adapted with permission from ref 15. Copyright 2013 American Chemical Society.

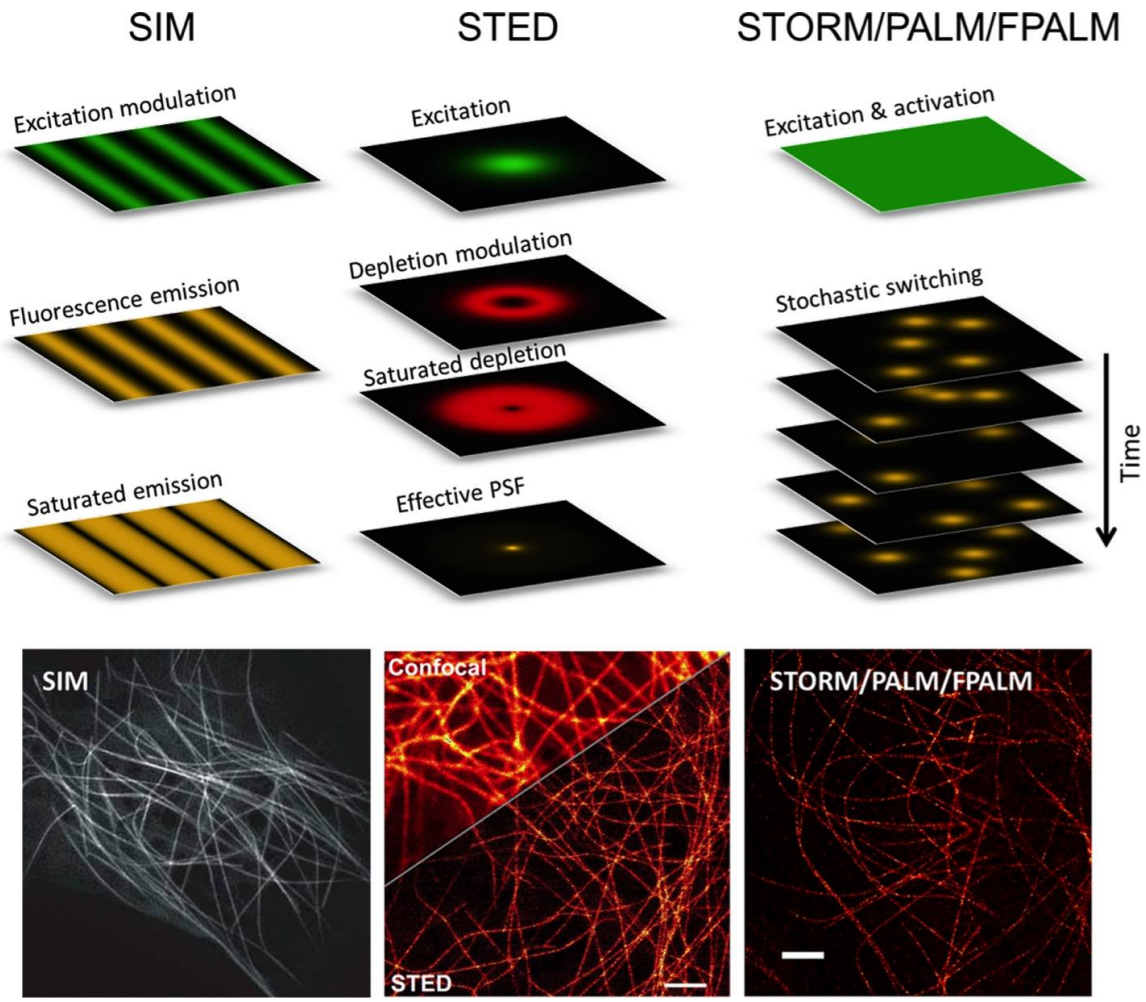

Figure 3. Super-resolution microscopy. Upper panel: Principles of super-resolution microscopy techniques. Lower panel: Confocal and super-resolution images of fluorescent protein labeled microtubules in living cells, showing SIM of EGFP-tubulin in a living Drosophila S2 cell (adapted with permission from ref 31. Copyright 2009 Nature Publication Group), confocal and STED microscopy of mCitrine-tubulin in a living PtK2 cell (adapted with permission from ref 30. Copyright 2008 National Academy of Sciences), and STORM/PALM/FPALM of mEos2-tubulin in a living Drosophila S2 cell (adapted with permission from ref 15. Copyright 2013 American Chemical Society), respectively. All images are shown with the same magnification. Scale bars: 2 μm.

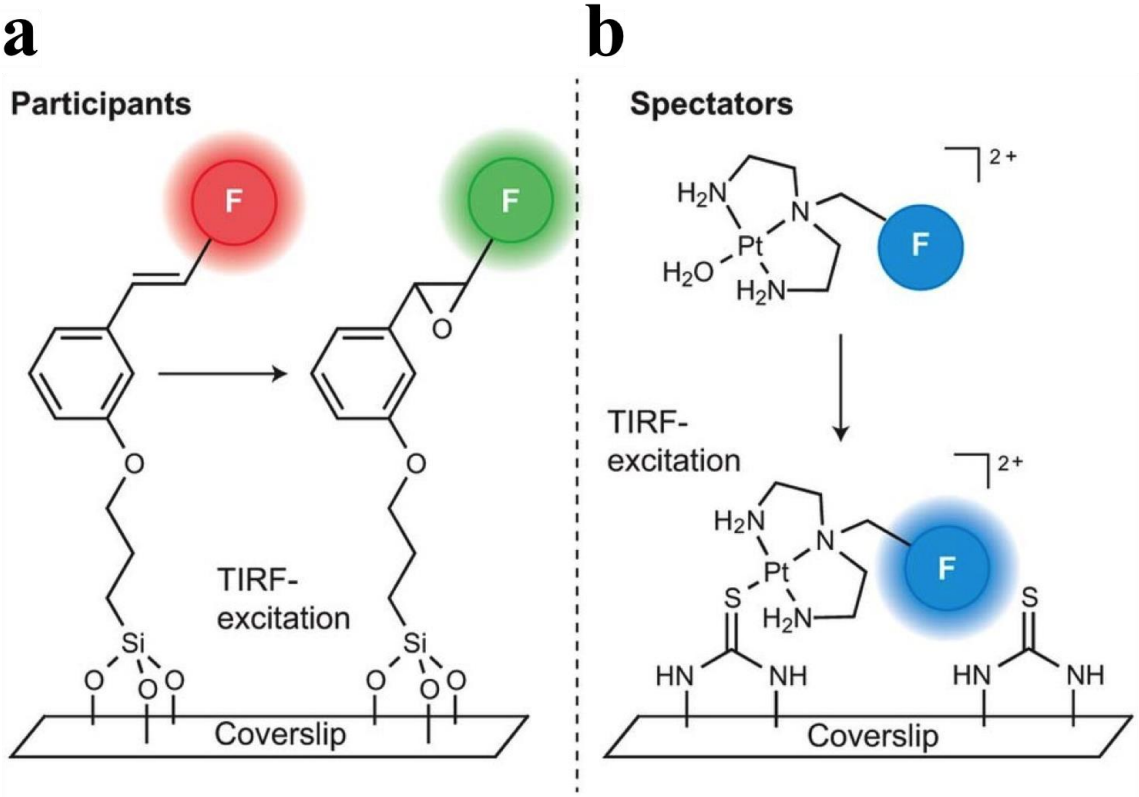

Figure 4. Principles of single molecule microscopy in chemical reaction imaging. Organic fluorophore (F) as participants (a) and spectator (b) for indicating events of chemical reactions. Adapted with permission from ref 62. Copyright 2014 Nature Publication Group.

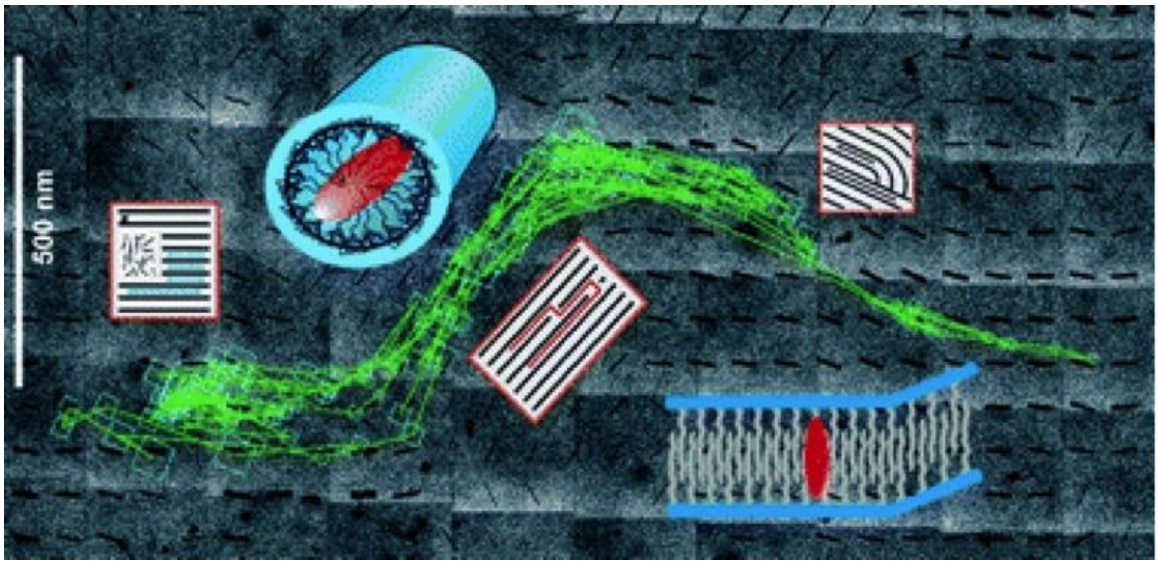

Figure 5. Single molecule microscopy in studying porous materials. Structure defects, pore network, and interconnectivity of channels (inserted images) were revealed by single molecular trajectories (green lines) within which the molecular positions were determined with nanometer precision. HRTEM images composed the background; two types of pore structures were presented. Adapted with permission from ref 67. Copyright 2011 Royal Society of Chemistry.

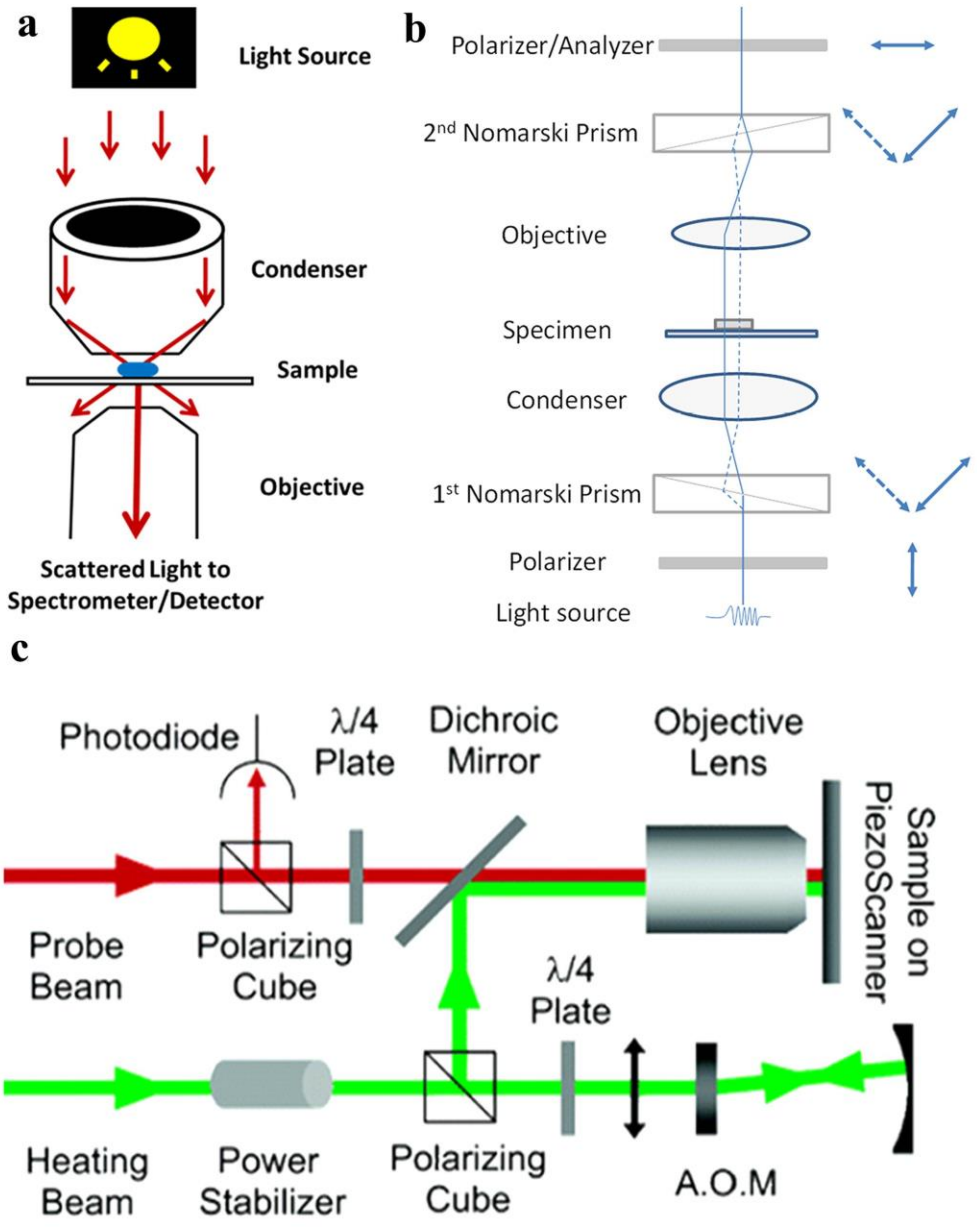

Figure 6. Optical imaging techniques for nonfluorescent nanoparticles. (a) Dark-field microscopy. (b) Differential interference contrast (DIC) microscopy. The arrows show the vibration directions of the light beams at different locations. Adapted with permission from ref 15. Copyright 2013 American Chemical Society. (c) Photothermal. Adapted with permission from ref 80. Copyright 2005 American Chemical Society.

CHAPTER 2: DIRECT STOCHASTIC OPTICAL RECONSTRUCTION MICROSCOPY IMAGING (dSTORM) OF MICROTUBULE ARRAYS IN INTACT *ARABIDOPSIS THALIANA* SEEDLING ROOTS WITH SUB-50-NM SPATIAL RESOLUTION

Bin Dong, Xiaochen Yang, Shaobin Zhu, Diane C. Bassham, and Ning Fang

Published in Scientific Reports[§]

Abstract

Super-resolution fluorescence microscopy has generated tremendous success in revealing detailed subcellular structures in animal cells. However, its application to plant cell biology remains extremely limited due to numerous technical challenges, including the generally high fluorescence background of plant cells and the presence of the cell wall. In the current study, stochastic optical reconstruction microscopy (STORM) imaging of intact *Arabidopsis thaliana* seedling roots with a spatial resolution of 20-40 nm was demonstrated. Using the super-resolution images, the spatial organization of cortical microtubules in different parts of a whole Arabidopsis root tip was analyzed quantitatively, and the results show the dramatic differences in the density and spatial organization of cortical microtubules in cells of different differentiation

---

stages or types. The method developed can be applied to a wide range of plant cell biological processes, including imaging of additional elements of the cytoskeleton, organelle substructure, membrane domains and other structures currently only accessible by electron microscopy.

Introduction

The emergence of far-field super-resolution microscopy techniques[1,2] has provided researchers with new opportunities for further insights into subcellular structures. The diffraction limit for light microscopy of about half of the wavelength of light is overcome in super-resolution techniques through spatial or temporal modulation of fluorophores. A group of techniques, named stochastic optical reconstruction microscopy (STORM),[3-5] photoactivated localization microscopy (PALM),[6] and fluorescence photoactivation localization microscopy (FPALM),[7] relies on the stochastic nature of single molecule switching. Photoactivatible fluorophores are switched randomly between a fluorescent state (on-state) and a dark state (off-state) or any other form that is non-fluorescent at the same wavelength, and isolated fluorescent molecules are localized by fitting with a point spread function (PSF) or with a Gaussian function as a close estimate. The enhancement of the spatial resolution using these techniques depends on the precision with which individual fluorescent molecules can be localized. This is in reverse relation to the square root of the photon number detected from a single molecule burst.[8,9] Therefore, single molecule detection with sufficiently high signal-to-noise ratio (S/N) is commonly required to achieve nanometer-scale localization accuracy. Total internal reflection (TIR) illumination was adapted to meet such requirements. Its thin illumination volume (a few hundred nanometers from the interface) greatly reduces the out-of-focus background.[10] Clearly, however, this also restricts the imaging depth. Various strategies, such as combining epi-

excitation and two-photon activation or using multiple imaging planes simultaneously, have been demonstrated to extend the super-resolution imaging depth to whole cell and tissue samples.[11-14]

Nearly all of these advances in super-resolution imaging were performed with mammalian cells. Very few reports exist of the study of cellular structures with such high resolution in plant samples due to numerous technical challenges,[15] including the generally high fluorescence background due to significant autofluorescence of endogenous components, and the presence of the cell wall (> 250 nm thickness). The former leads to low S/N for single molecule detection and therefore low localization accuracy and low spatial resolution. The latter contributes to a higher background due to additional layers with mismatched refractive indices (causing more severe scattering and spherical aberration) and restricts the use of TIR illumination.

Several super-resolution imaging techniques have been tested for imaging plant samples. The structure of perinuclear actin in live tobacco cells was visualized with a lateral resolution of 50 nm by combining PALM imaging with optical sectioning.[16] The organization of cellulose microfibrils on the outer side of the cell wall in live onion epidermal cells has been studied by STORM imaging with a lateral resolution of 100 nm.[17] Structured illumination microscopy, which uses specially designed illumination patterns to spatially modulate fluorophores,[18] was used for imaging the dynamics of endoplasmic reticulum, plasmodesmata, and cortical microtubules in live cells with a two-fold improvement in the spatial resolution (~ 100 nm) over traditional fluorescence microscopy techniques.[19,20] Stimulated emission depletion (STED) microscopy has also been used to measure the size of protein clusters on the lateral plasma membrane of plant cells with a lateral resolution of 70 nm.[21] Despite all of these recent advances,

imaging cellular structures deep in plant cells, such as those of intact Arabidopsis root tips, with a spatial resolution below 50 nm remains a challenge.

Plant cells have highly anisotropic shapes that are important to cell function and multicellular development.[22] The cortical microtubule array is one of the key factors in determining plant cell morphogenesis. In rapidly expanding plant cells, cortical microtubules are often densely aligned parallel to each other with a transverse orientation to the direction of growth. Several models including the cellulose synthase constraint hypothesis,[23-25] templated-incorporation model,[26] and the microfibril length regulation hypothesis[27] have been established or proposed to explain the role of cortical microtubule arrays during cell expansion. Detailed quantitative information on the structure and organization of cortical microtubules is critical to an understanding of the mechanism of cell expansion and directional growth. We therefore use the cortical microtubule array as a test case in the present study to develop techniques for super-resolution imaging within whole-mount seedling root tips. We successfully demonstrated a spatial resolution of 20-40 nm in whole plant tissue imaging by combining direct STORM,[28] which is essentially STORM without an activator fluorophore, with variable angle epi-fluorescence microscopy (VAEM).[29,30] Such high spatial resolution is crucial to resolve the dense cortical microtubule structures in the active elongation zone of the plant root. Quantitative data including microtubule density and orientation have been obtained for intact Arabidopsis seedling roots.

Results and Discussion

Comparison of the background between epi-illumination and VAE illumination

The evanescent field generated by TIR illumination excites samples within a few hundred nanometers of the solid-liquid interface.[31] The thin illumination volume largely rejects the out-of-focus background, thereby offering an ideal optical sectioning method for imaging with high S/N, and has been frequently used for super-resolution imaging in animal cells[3,6]. However, the application of TIR illumination is restricted to the surface because of its shallow illumination depth, limiting its use with plants due to the presence of the thick cell wall. To overcome this limitation, VAE illumination[32] was developed to extend the illumination depth to a few tens of micrometers when the incident angle is operated at subcritical angles (smaller than but still very close to the critical angle), while the S/N is still several fold higher than that of epi-illumination (Fig. 2B, C). The features of VAE make it an excellent choice for imaging cortical microtubules in plant root cells.

Cortical microtubules of young Arabidopsis seedling root cells were labeled with the photoswitchable dye Alexa Fluor 647 through immunostaining with tubulin antibodies. The excitation (660 nm) laser and the activation (405 nm) laser were collimated and operated at subcritical angles at the interface of the root sample and the coverslip (Fig. 1 and Fig. 2). The background is greatly reduced with the confined excitation volume under VAE illumination (Fig. 3). The cross-sectional profiles along the elongation direction of the root cells show that dense microtubules are much better resolved in images under VAEM than under epi-illumination (Fig. 3E). The light intensity profile on the sample side is shown in Fig. 2D. Within 10° of the critical angle, the light intensity is higher than the incident beam. This feature is also important for

STORM imaging experiments, in which turning off fluorescent molecules to a ‘dark’ state usually requires high illumination light intensity.

Imaging cortical microtubule arrays in plant cells with VAEM-STORM imaging

Images of the cortical microtubule arrays were reconstructed from 20,000-30,000 frames captured in 17-25 min. To correct for the sample stage drift during the relatively long STORM image acquisition period, fluorescent beads were used as landmarks to track the stage movement and reconstruct the STORM images (e.g., Fig. 4C), which show higher spatial resolution compared to epi-fluorescence images (e.g., Fig. 4B and Fig. 5A) and confocal microscopy images (Fig. 5C-D). In the regions where cortical microtubules are present at high density and unresolved in epi-fluorescence and confocal microscopy images, individual microtubule filaments are clearly well-separated and resolved from each other in the STORM images. The complex organization patterns of cortical microtubule arrays in higher plants have diverse forms including random arrangement, regional organization, and eventually global organization. For example, parallel cortical microtubules in fast-elongating plant cells often co-align, forming microtubule bundles that are crucial for stabilizing the whole microtubule network. The bundles are believed to form by the crosslinking of individual microtubules with filamentous structures composed of microtubule-associated proteins.[8,33-36] Electron microscopy (EM) was used in these studies to reveal the details of cross-linking including the bridge-angle and inter-microtubule spacing in synthesized microtubule networks *in vitro*. As an example, in Fig. 4D-E, individual microtubule filaments in one bundle are clearly resolved, showing a spacing of 80-140 nm between neighboring microtubules, which is in agreement with the EM results.[34]

Determination of the spatial resolution of VAEM-STORM imaging in plant tissues

To quantify the achieved spatial resolution of VAEM-STORM imaging, point-like objects appearing as small clusters in the STORM images were used for analysis (Fig. 6A), as was described previously.[4,37] The lateral resolution was estimated to be 42 nm as the full width of half maximum (FWHM) from 2D Gaussian fitting of the distributions of locations (Fig. 6B). Alternatively, the resolution can be estimated from the localization accuracy.[3] The average localization precision (σ) is 16.0 ± 2.2 nm (Fig. 6D) from single molecule image analysis of the same clusters, giving a localization accuracy (~2.35σ) of 37.6 ± 5.2 nm. The results from both analyses agree well. Therefore, we have achieved a resolution of ~40 nm in intact plant tissue imaging.

We then measured the apparent width of individual cortical microtubule filaments in the STORM images by analyzing the cross-sectional profiles (Fig. 6E). Relatively long cortical microtubule filaments were chosen in order to obtain more reliable results. Fitting the cross-sectional distributions of the microtubule filament with a Gaussian distribution gives a FWHM of 52 nm (Fig. 6F). The average apparent width over 20 microtubule filaments is 57 ± 4 nm. The measured width is in agreement with the actual size of a microtubule filament plus staining with primary antibody and secondary $F(ab')_2$ fragments.[38] These results illustrate that the final spatial resolution depends both on the imaging method and the size of the objects. Therefore, microtubule filaments separated by ~60 nm should be readily resolved in VAEM-STORM imaging. As an example, two microtubules with 62-nm-separation are clearly resolved in Fig. 6G-H. Quantification of the ability to resolve nearby cortical microtubules based on Rayleigh criteria gives a resolution of 67 ± 8 nm.

Optimization of sample preparation and labeling

In order to label cytoskeletal structures in plant cells, permeabilization of the cell wall is required, as it presents an obstacle for the transfer of any probe larger than several nanometers into the cytoplasm. Several methods, including the digestion of cell walls with degradative enzymes (whole-mount),[39] mechanical sectioning[40] and freeze shattering combined with enzyme degradation,[41] have been previously reported. In addition, appropriate labeling density is critical for localization-based super-resolution imaging. The typical labeling concentrations reported in the literature were 1 - 10 μg/mL of dye-conjugated antibodies in animal cell imaging.[4,28] We attempted VAEM-STORM imaging of plant cells using such labeling conditions, using whole-mount samples in which the integrity of the cells is well preserved. However, due to high background and substantial interference between single molecule images resulting from the high labeling densities under such experimental conditions, no clear microtubule structures could be reconstructed (results not shown).

To optimize the labeling strategy, we conducted two sets of experiments. In the first, combinations of different concentrations of both primary tubulin antibody and secondary $F(ab')_2$ fragment with whole mount immunostaining were used to label the cortical microtubules of Arabidopsis seedling roots (Fig. 7A-D). The labeling concentration of Alexa Fluor 647-conjugated $F(ab')_2$ fragments was found to contribute the most to increasing the localization precision and thus the spatial resolution. The best spatial resolution of ~ 38 nm was achieved with 1.0 μg/mL primary antibody and 0.04 μg/mL secondary $F(ab')_2$ fragment, as a result of more photons being collected and lower background noise (Fig. 7F-H). Continuous structures could not be completely reconstructed using more dilute labeling conditions (results not shown). These concentrations are ~50-fold lower than the typical concentrations used in mammalian cell STORM imaging [4,28]. The low concentration of antibodies reduces the number of activated

probes during every activation cycle and increases the accuracy of point-localization during analysis [42]. Proper labeling density and relatively low background were achieved at these optimum antibody concentrations as demonstrated in Fig. 7A-D.

In the second set of experiments, we compared the whole mount method of sample preparation with the freeze shattering/enzyme degradation method, in which intact roots were randomly split longitudinally, reducing the number of cell layers in the roots. Each method was followed with immunostaining of cortical microtubules using the optimized labeling concentrations. For both methods, sub-diffraction limited resolution was achieved for imaging cortical microtubules in Arabidopsis seedling root epidermal cells (Fig. 7D, E). To quantitatively compare the spatial resolution achieved with these two sample preparation methods, cluster analysis was performed for each. The spatial resolution, estimated from the single molecule localization precision, was ~38 nm and ~23 nm for the whole mount and freeze shattering plus enzyme degradation methods respectively (Fig. 7F). The increased resolution upon freeze shattering was primarily due to an increase in the number (N) of photons collected, from 3988 ± 53 photons up to 5525 ± 352 photons, and a reduction in b from 69 ± 8 photons to 54 ± 3 photons (Fig. 7G, H). The increased photon counts and reduced background noise improve the localization accuracy by a factor of two, indicating that the multiple cell layers of intact roots is one important factor limiting the resolution achievable during super-resolution imaging in plant tissues. Especially in the case of the freeze shattering method, the spatial resolution was comparable to that achieved in animal cell imaging. Although it has been argued that minimal disruption of cellular components is introduced by freeze-shattering,[41] the continuous structure of the cortical microtubules could be disrupted noticeably with this method as shown in the present work (Fig. 7E). Intact root staining is therefore the procedure of choice unless maximal spatial resolution is required. We used the whole mount immunostaining method to label cortical

microtubules with the photoswitchable dye molecule Alexa Fluor 647 for the remaining experiments.

Quantitative analysis of the microtubule network with sub-50-nm resolution

The cortical microtubule array plays a key role in controlling plant cell growth and anisotropy through directly guiding the deposition of cell wall material. This occurs largely by determining the directional movement and plasma membrane insertion site of cellulose synthase complexes during cellulose synthesis and deposition, which constrains the direction of plant cell expansion.[25,43] Quantitative analysis of microtubule organization can therefore provide insight into the expansion and differentiation status of cells within the root.[44] Due to technical limitations, the details of microtubule structures have not been fully visualized or quantified. Using the enhanced spatial resolution of STORM images, quantitative data including microtubule density and orientation were obtained. Individual microtubules were resolved from one another even within crowded microtubule bundles, allowing the microtubule density to be accurately determined by simply counting microtubule filaments per micrometer. The uniformity of microtubule filament distribution within a cell is related to its differentiation status. Insights into cellular growth and differentiation could be acquired with accurate assessment of the microtubule density.

Although the predominant orientation of cortical microtubules can be identified from both epi-fluorescence and STORM images, much more detail is evident in the STORM images. Fig. 9F and Fig. 9G show the distributions of cortical microtubules in the highlighted red boxes in the epi-fluorescence (Fig. 9D) and the STORM (Fig. 9E) image, respectively. In addition to the predominant transverse alignment, a significant population of microtubules aligning in

between the transverse and longitudinal orientations can be resolved only in the STORM image. To verify the results from manual counting (Fig. 8), MicroFilament Analyzer (MFA)[44] was also used to analyze the angular distributions of cortical microtubules in both epi-fluorescence (Fig. 9H) and STORM (Fig. 9I) images. Consistently, more detailed structural information is found in the STORM images as demonstrated in the polar plots (Fig. 9J, K). It is therefore evident that STORM imaging, with the capability of resolving individual microtubules with sub-50-nm spatial resolution, helps in the accurate determination of the spatial organization, including density and orientation of cortical microtubule arrays, in plant cells.

VAEM-STORM imaging of a whole Arabidopsis seedling root tip

The spatial organization of cortical microtubules can change as a response to the environment or during different developmental stages.[45,46] In Arabidopsis roots, the apical meristem is initially established during embryo development and provides stem cells for later, post-embryonic, growth. The defined division patterns of the stem cells lead to the formation of distinct developmental zones along the length of the root.[47,48] After cell division occurs in the meristem, cells leave the meristem and begin to elongate in a specialized zone termed the transition zone. Extensive rearrangement of the cytoskeleton occurs in the transition zone to allow the developmental switch to elongation. Cells then enter the elongation zone, in which rapid cell elongation occurs, and finally the more distal differentiation zone.[49]

Seven regions (***a-g***) spread throughout a root tip, as highlighted in the white boxes in Fig. 10A, were chosen for STORM imaging. Regions ***a*** and ***b*** represent cells in the apical cap and meristematic zone respectively, ***c-d*** are in the elongation zone, *e-**f*** is between the elongation and the differentiation zone, and finally, ***g*** is in the differentiation zone. Variations in density and

orientation of microtubule arrays between different zones in the root tip can be observed qualitatively in both epi-fluorescence images and STORM images; however, accurate quantitative structural information, which varies dramatically in different zones, is only available in STORM images (Fig. 10B).

The STORM images show that cortical microtubules in rapidly elongating cells (Fig. 10B ***c*** and Fig. 4C) are preferentially present in bundled structures, while single unbundled microtubules are commonly found in the apical cap and meristematic cells(Fig. 10B *a*-***b***) and the differentiated cells (Fig. 10B ***g***) where the microtubules are less organized and at lower density. Moreover, the transition regions (Fig. 10B ***e, f***) between different zones have intermediate microtubule density, indicating the changing organization during different growth phases. It has been suggested that the highly spatially organized and more stable regions of the cortical microtubule arrays are formed from bundled microtubules; the bundling lends stability to the overall structure despite the rapid treadmilling behavior of individual filaments.[50] In contrast, the less organized and short-lived areas were hypothesized to correspond to individual microtubules present at lower density that move and reorganize via treadmilling.[51] To provide direct evidence for this hypothesis, super-resolution is necessary to distinguish individual microtubules within bundles and to accurately assess microtubule density in different regions of the plant root.

Fig. 11 shows the results from the quantitative analysis of the density and orientation of cortical microtubules in the cells highlighted in Fig. 10. Statistics provided in Table 1 indicate that the microtubule densities are not significantly different ($P > 0.1$) between regions ***c-d***, ***e-f*$_1$**, ***f*$_2$*-g***. Root cap cells (***a***) have loosely organized cortical microtubule structures at low density ($1.6 \pm 0.8\ \mu m^{-1}$) and rarely form microtubule bundles. Cells in the late meristematic zone (***b***) have an increased microtubule density, and the cortical microtubules are arranged more tightly in the

transverse direction. In the elongation zone (***c, d***), cortical microtubules strongly prefer to exist as bundles in the rapidly growing cells, and as expected, the density is 3-4 times higher (~ 6.0 μm^{-1}) than in region ***a***. For the cells in the late elongation or early differentiation stages (***e, f_1***), the microtubule density decreases to ~ 4.0 μm^{-1}. Cortical microtubule structure becomes loose (~ 2.0-2.5 μm^{-1}) and preferentially exists as free microtubule filaments in the differentiation zone (***f_2, g***), which is consistent with decreasing growth.

Microtubule orientation, on the other hand, varies dramatically in different zones of the root tip. This set of data shows that microtubule orientation changes from random alignment at low density (***a***), to transverse alignment (90° to the long axis of the cell) at high density (***b-f_1***), then to random alignment again at intermediate density (***f_2-g_1***), and finally to longitudinal alignment at low density (***g_2***). Consistent with previous reports,[52] cortical microtubules are more likely to have a random organization in the root apical area (***a***) where cells are in the process of division, and no predominant orientations are found in this region. A transverse alignment is predominant in ***b*** to ***f_1*** with only small variations among these regions. Nonetheless, a significant population of microtubules with small orientation angles are present in ***f_1*** which does not exist in ***b-e***. In contrast to ***f_1***, the adjacent cell ***f_2*** has no predominant orientations (with angles spanning the full range), which is consistent with the helical structure of cortical microtubules[39] in ***f_2***. The variability in microtubule orientation continues to increase in ***g_1***; however, its adjacent cell ***g_2*** shows a predominant orientation angle parallel to the cell's long axis. The difference in microtubule organization at the same distance from the root tip (***f_1*** vs. ***f_2*** and ***g_1*** vs. ***g_2***) could be because neighboring cells are at different differentiation stages or, alternatively, because they are of different cell types (epidermal and cortical cells).[23]

Conclusions

In conclusion, we have successfully applied direct STORM imaging to cortical microtubules in Arabidopsis root cells with sub-50-nm resolution. The optimized labeling strategy, with much lower antibody/fragment concentrations compared to those reported in the literature, was critical for achieving such high resolution in plant cell and whole tissue imaging. Different sample preparation methods, including the commonly used enzymatic degradation of the cell wall and a combination of freeze-shattering and enzymatic cell wall degradation, were optimized to provide a spatial resolution of up to 20 nm, which is close to the best resolution demonstrated in mammalian cells. Finally, we quantified the spatial organization of cortical microtubules in different parts of an intact Arabidopsis root tip. The quantitative results show the dramatic differences in the density and spatial organization of cortical microtubules in cells of different differentiation stages or types. The methods developed can be applied to a wide range of plant cell biological processes, including imaging of additional elements of the cytoskeleton, organelle substructure, membrane domains and other structures currently only accessible by electron microscopy. We expect these advances in super-resolution imaging will enable critical progress in understanding the detailed spatial organization of biological processes in plant cells.

Materials and Methods

Optical setup for VAEM-STORM

The imaging system for VAEM-STORM (Fig. 1) was integrated into an inverted microscope (Zeiss, Axiovert 100 TV, Germany). Multicolor lasers were collimated into a single light path after the beam expander (Thorlabs, BE03M-A) with 3× magnification. Illumination light was provided by solid state lasers operating at different wavelengths (Newport, Excelsior

one 405 nm, 200 mW; Laser Quantum, Gem 660, 200 mW). Collimation of multicolor lasers was accomplished by using a dichroic mirror (Thorlabs, DMLP425T), thus allowing simultaneous illumination of the sample at multi-wavelengths. Uniblitz mechanical shutters (Vincent Associates, LS2Z2) in front of each laser were used to control the illumination conditions, either pulsed or continuous illumination profiles. The collimated light was expanded by a telescope of a pair of achromatic lenses (Thorlabs, AC127-025-A & AC254-150-A) and then focused at the back focal plane of a high refractive index oil immersion objective (Nikon, 100X Oil, N.A. 1.49) using another achromatic lens (Thorlabs, AC508-200-A). The incident angle of illumination light is controlled by the lateral shift of the light path, through a three-dimensional stage (Sigma KOKI, SGSP-20-20), before entering the objective. A multi-edge beam splitter (Semrock, DC-405-388-543-635) was used to reflect the light into the working objective to excite the sample and the emission light is collected by the same objective. After the tube lens provided with the microscope, a pair of relay lenses (Thorlabs, AC127-125-A) was used to focus emission light onto an EMCCD chip (Andor iXon^{EM}+ 897) enabling a pixel size of ~160nm. A combination of filters (Semrock, 664 nm RazorEdge long-pass edge filter (LP02-664RU-25), 658 nm StopLine single-notch filter (NF03-658E-25), 708/75 nm BrightLine single-band bandpass filter (FF01-708/75-25)) was inserted in front of the camera to reduce the background noise. Epi-fluorescence imaging under variable angle illumination and VAEM-STORM imaging were performed using the customized system. Confocal images were acquired with a Leica confocal laser scanning microscope (Leica Microsystems, Leica SP5) using a ×63 Leica oil-immersion objective. Excitation and emission wavelengths were 652 and 668 nm respectively.

Plant materials and growth conditions

Arabidopsis thaliana Columbia-0 seeds were surface sterilized with 33% bleach (Clorox), 0.1% (v/v) Triton X-100 (Sigma) for 20 min, followed by 5 rinses with deionized water. Sterilized seeds were kept in the dark at 4°C for 2 days. Arabidopsis seedlings were grown vertically for 3-5 days under long-day conditions (16 hours light) on half-strength MS agar medium (Murashige-Skoog vitamin and salt mixture [Caisson, MSPA0910]) with 1% sucrose (Sigma), 2.4 mM MES (Sigma) (pH 5.7) , and 0.6% (w/v) Phytoblend (Caisson).

Immunofluorescence by whole mounting

Arabidopsis seedlings were immunostained as previously described[39] with some modifications. Three- to five-day-old Arabidopsis seedlings were fixed for 40 min in fixation solution (1.5% paraformaldehyde (Sigma) and 0.5% glutaraldehyde (Sigma) in PME buffer [50mM PIPES (J.T. Baker), 2mM EGTA (Sigma), 2mM MgSO4 (Fisher)] with 0.05% Triton X-100). The fixed samples were washed 3 times (10 min each time) with PME buffer followed by digestion for 20 min with 0.05% (w/v) Pectolyase (Karlan) in 0.4M mannitol (Sigma) in PME buffer. The samples were washed again in PME buffer for 3 x 5 min. The samples were treated with -20°C methanol (Fisher) for 10 min and rehydrated in phosphate-buffered saline (PBS) buffer for 10 min. 1mg/mL $NaBH_4$ (Fisher) in PBS was applied to the samples for 20 min to reduce autofluorescence and then 3% BSA (Fisher) in PBS supplemented with 50 mM Gly (MP Biomedicals) for 3 hours for blocking. The samples were incubated with mouse anti-α-tubulin primary antibody (Sigma, T6074) at 1:1000-1:2000 dilution in 1% BSA in PBS at 4°C overnight. Samples were washed three times for 10 min each and incubated in Alexa Fluor-647 modified $F(ab')_2$ fragment of goat anti-mouse IgG (H+L) (Invitrogen, A-21237) at 1:20,000 - 1:50,000 dilution in 1% BSA in PBS for 3 hours at 37 °C. After rinsing 5 times (10 min each time) in

PBS, samples were post-fixed with fixation solution, washed a further 3 times (10 min each time), and mounted on a coverslip in imaging buffer [100 mM Tris pH 8.0 (Ambion), 10 mM NaCl (Sigma), 0.5mg/mL glucose oxidase (Sigma), 40μg/mL catalase (Sigma), 10% (w/v) glucose (Sigma) and 1% (v/v) β-mercaptoethanol (Sigma)] for epi-fluorescence/STORM imaging or kept in PBS buffer at 4°C for up to one month.

Immunofluorescence by freeze shattering

Freeze-shattering was performed as described previously[41] with modifications. Three- to five-day-old Arabidopsis seedlings were fixed in fixation solution, washed 5 times with PME buffer and digested with enzyme as same as those in whole mounting method. After digestion, samples were placed between two 3-Aminopropyltriethoxysilane (APTES) coated slides and frozen immediately in liquid nitrogen for 5 min. After removal from liquid nitrogen, the paired-slides were immediately separated and air-dried for 40 min. Freeze-shattered samples were permeabilized on the slides using 0.5% [v/v] NP40 (USB) and 10% DMSO (Fisher) in PME buffer and washed three times with PME buffer (10 min each time). The samples were reduced using 1 mg/mL $NaBH_4$ in PBS for 20 min and blocked with 3% BSA in PBS for 1.5-2 hours. Primary antibody and secondary fragment were as above. The samples were post-fixed for 20 min in fixation solution. For long-time storage, samples were immersed in PBS buffer and kept at 4°C for up to one month.

Sample preparation and drift correction using fiducial marker

For intact root samples, the labeled root was placed on a 22×50mm coverslip (Corning, No.1). For the freeze-shattering procedure, glass slides coated with APTES were used to attach the root to the surface. Imaging buffer was applied to the sample slide and then an 18×18mm

coverslip (Corning, No.1) was applied on the sample to form a chamber and sealed using nail polish to avoid oxygen from the air, thus allowing imaging for several hours. The sample chamber was then placed on a customized sample holder and was locked with two metal clips to reduce the sample drift. The sample holder was mounted on a high performance three-dimensional piezo stage (PI, P-527.3CD), which was integrated into the microscope system. Fluorescent beads (Invitrogen, T7279) absorbed on the coverslip or glass slides were used as fiducial markers. The positions of the beads were tracked and used for stage drift correction of localized molecular positions in STORM images.

Localizing the center of single molecules and determining localization accuracy

The molecular size of single fluorescent molecules is usually a few nanometers; however the corresponding microscopic images have a typical size of a few hundred nanometers because of the point spread function (PSF) of the imaging system. Though the true molecular size of molecules cannot be determined using fluorescence microscopy, the centroid of the molecule can be localized with high precision with fitting by its PSF or 2D Gaussian function as an estimate. The precision of the localization, in brief, is inversely proportional to the square root of photons ($\sqrt{N}$) collected from the single molecule.[8] Molecules emitting several thousand photons can be localized with nanometer precision under this standard. The simple estimation model works well in cases where the background noise is very small so that it can be neglected. In circumstances such as plant cell imaging, background noise is often high. Localization precision is measured by using another equation according to Thompson et al.[53]

$$\sigma = \sqrt{\frac{s^2}{N} + \frac{a^2}{12N} + \frac{8\pi b^2 s^4}{a^2 N^2}}$$

where *s* is the standard deviation of the Gaussian distribution that equals 1/2.2 of the PSF width, *a* is the pixel size, *b* is background noise and *N* is number of collected photons. The first term (s^2/N) is the photon noise, the second term is the effect of finite pixel size of the detector, and the last term is the effect of background. Using point-like objects appearing as clusters in the STORM images, the fitting parameters (Fig. 6A) were extracted *b*: 68, *N*: 3600, *a*: 156 nm giving an average localization of 16 nm. The FWHM of the fitting is used, giving an estimation of the spatial resolution as 40 nm. The spatial distributions of the clusters were also fitted by 2D Gaussian function giving a FWHM of 42 nm (Fig. 6B), in agreement with the results from single molecule fitting. The spatial resolution in VAEM-STORM imaging of intact Arabidopsis root cells in our experiments therefore was comparable to the resolution in animal cell imaging.

Data analysis of VAEM-STORM imaging

VAEM-STORM imaging data was processed using Insight3 software kindly provided by Dr. Bo Huang, University of California at San Francisco. In our experiments, an imaging sequence of 20,000-30,000 frames recorded at 20-60Hz was used to reconstruct a high resolution STORM image. In each frame, individual molecules were identified and fit by an elliptical Gaussian function to determine their centroid positions, widths, intensities and ellipticities. A threshold was chosen to eliminate molecules that were too dim, too wide or too elliptical to yield high localization accuracy based on the fit parameters. Usually, the intensity of the illumination light and the recording speed was adjusted such that fluorescent molecules were in the ‘on’ state for 2 – 3 frames. Molecules appearing in consecutive frames with a displacement smaller than one pixel were considered to be from the same fluorescent molecule and their final positions were determined using the weighted centroid positions in all consecutive frames.

A pixel size of 10 nm was used to generate the STORM images. In the STORM images, each molecular position was assigned as one point. These points were rendered as a normalized 2D Gaussian peak, the width of which was determined by its theoretical localization accuracy calculated from the number of photons detected for that localization event.

Acknowledgements

We thank Dr. Bo Huang and Jörg Schnitzbauer at the University of California, San Francisco for providing the imaging data analysis program 'Insight3' and for assistance with data analysis.

References:

1 Huang, B., Babcock, H. & Zhuang, X. Breaking the Diffraction Barrier: Super-Resolution Imaging of Cells. *Cell* **143**, 1047-1058, (2010).

2 Hell, S. W. Far-Field Optical Nanoscopy. *Science* **316**, 1153-1158 (2007).

3 Rust, M. J., Bates, M. & Zhuang, X. Sub-diffraction-limit imaging by stochastic optical reconstruction microscopy (STORM). *Nat. Methods* **3**, 793-796, (2006).

4 Bates, M., Huang, B., Dempsey, G. T. & Zhuang, X. Multicolor Super-Resolution Imaging with Photo-Switchable Fluorescent Probes. *Science* **317**, 1749-1753 (2007).

5 Huang, B., Wang, W., Bates, M. & Zhuang, X. Three-Dimensional Super-Resolution Imaging by Stochastic Optical Reconstruction Microscopy. *Science* **319**, 810-813 (2008).

6 Betzig, E. *et al.* Imaging Intracellular Fluorescent Proteins at Nanometer Resolution. *Science* **313**, 1642-1645 (2006).

7 Hess, S. T., Girirajan, T. P. K. & Mason, M. D. Ultra-High Resolution Imaging by Fluorescence Photoactivation Localization Microscopy. *Biophys. J.* **91**, 4258-4272, (2006).

8 Ober, R. J., Ram, S. & Ward, E. S. Localization Accuracy in Single-Molecule Microscopy. *Biophys. J.* **86**, 1185-1200, (2004).

9 Yildiz, A. & Selvin, P. R. Fluorescence Imaging with One Nanometer Accuracy: Application to Molecular Motors. *Acc. Chem. Res.* **38**, 574-582, (2005).

10 Stender, A. S. *et al.* Single Cell Optical Imaging and Spectroscopy. *Chem. Rev.* **113**, 2469-2527, (2013).

11 Dedecker, P., Flors, C., Hotta, J.-i., Uji-i, H. & Hofkens, J. 3D Nanoscopy: Bringing Biological Nanostructures into Sharp Focus. *Angew. Chem.-Int. Edit.* **46**, 8330-8332, (2007).

12 Fölling, J. *et al.* Fluorescence Nanoscopy with Optical Sectioning by Two-Photon Induced Molecular Switching using Continuous-Wave Lasers. *ChemPhysChem* **9**, 321-326, (2008).

13 Jones, S. A., Shim, S.-H., He, J. & Zhuang, X. Fast, three-dimensional super-resolution imaging of live cells. *Nat. Methods* **8**, 499-505, (2011).

14 Vaziri, A., Tang, J., Shroff, H. & Shank, C. V. Multilayer three-dimensional super resolution imaging of thick biological samples. *Proc. Natl. Acad. Sci. U. S. A.* (2008).

15 Ehrhardt, D. W. & Frommer, W. B. New Technologies for 21st Century Plant Science. *Plant Cell* **24**, 374-394 (2012).

16 Durst, S. *et al.* Organization of perinuclear actin in live tobacco cells observed by PALM with optical sectioning. *J Plant Physiol* **171**, 97-108, (2014).

17 Liesche, J., Ziomkiewicz, I. & Schulz, A. Super-resolution imaging with Pontamine Fast Scarlet 4BS enables direct visualization of cellulose orientation and cell connection architecture in onion epidermis cells. *BMC Plant Biol.* **13**, 226 (2013).

18 Gustafsson, M. G. L. Nonlinear structured-illumination microscopy: Wide-field fluorescence imaging with theoretically unlimited resolution. *Proc. Natl. Acad. Sci. U. S. A.* **102**, 13081-13086 (2005).

19 Fitzgibbon, J., Bell, K., King, E. & Oparka, K. Super-Resolution Imaging of Plasmodesmata Using Three-Dimensional Structured Illumination Microscopy. *Plan Physiol* **153**, 1453-1463 (2010).

20 Komis, G. *et al.* Dynamics and Organization of Cortical Microtubules as Revealed by Superresolution Structured Illumination Microscopy. *Plan Physiol* **165**, 129-148 (2014).

21 Kleine-Vehn, J. *et al.* Recycling, clustering, and endocytosis jointly maintain PIN auxin carrier polarity at the plasma membrane. *Mol Syst Biol* **7**, 540-540, (2011).

22 Paradez, A., Wright, A. & Ehrhardt, D. W. Microtubule cortical array organization and plant cell morphogenesis. *Curr Opin Plant Biol* **9**, 571-578, (2006).

23 Smith, L. G. Cytoskeletal control of plant cell shape: getting the fine points. *Curr Opin Plant Biol* **6**, 63-73, (2003).

24 Smith, L. G. & Oppenheimer, D. G. SPATIAL CONTROL OF CELL EXPANSION BY THE PLANT CYTOSKELETON. *Annu. Rev. Cell Dev. Biol.* **21**, 271-295, (2005).

25 Paredez, A. R., Somerville, C. R. & Ehrhardt, D. W. Visualization of Cellulose Synthase Demonstrates Functional Association with Microtubules. *Science* **312**, 1491-1495 (2006).

26 Baskin, T. On the alignment of cellulose microfibrils by cortical microtubules: A review and a model. *Protoplasma* **215**, 150-171, (2001).

27 Wasteneys, G. O. Progress in understanding the role of microtubules in plant cells. *Curr Opin Plant Biol* **7**, 651-660, (2004).

28 van de Linde, S. *et al.* Direct stochastic optical reconstruction microscopy with standard fluorescent probes. *Nat Protoc* **6**, 991-1009 (2011).

29 Wang, X. *et al.* Imaging of Dynamic Secretory Vesicles in Living Pollen Tubes of Picea meyeri Using Evanescent Wave Microscopy. *Plan Physiol* **141**, 1591-1603 (2006).

30 Konopka, C. A. & Bednarek, S. Y. Variable-angle epifluorescence microscopy: a new way to look at protein dynamics in the plant cell cortex. *Plant J* **53**, 186-196, (2008).

31 Axelrod, D., Burghardt, T. P. & Thompson, N. L. Total Internal-Reflection Fluorescence. *Annu. Rev. Biophys. Bioeng.* **13**, 247-268 (1984).

32 Tokunaga, M., Imamoto, N. & Sakata-Sogawa, K. Highly inclined thin illumination enables clear single-molecule imaging in cells. *Nat. Methods* **5**, 159-161, (2008).

33 Chen, J., Kanai, Y., Cowan, N. J. & Hirokawa, N. Projection domains of MAP2 and tau determine spacings between microtubules in dendrites and axons. *Nature* **360**, 674-677 (1992).

34 Gaillard, J. *et al.* Two Microtubule-associated Proteins of Arabidopsis MAP65s Promote Antiparallel Microtubule Bundling. *Mol. Biol. Cell* **19**, 4534-4544 (2008).

35 Fache, V. *et al.* Arabidopsis Kinetochore Fiber-Associated MAP65-4 Cross-Links Microtubules and Promotes Microtubule Bundle Elongation. *Plant Cell* **22**, 3804-3815 (2010).

36 Li, H. *et al.* Arabidopsis microtubule-associated protein AtMAP65-2 acts as a microtubule stabilizer. *Plant Mol Biol* **69**, 313-324, (2009).

37 Cella Zanacchi, F. *et al.* Live-cell 3D super-resolution imaging in thick biological samples. *Nat. Methods* **8**, 1047-1049, (2011).

38 Weber, K., Rathke, P. C. & Osborn, M. Cytoplasmic Microtubular Images in Glutaraldehyde-Fixed Tissue Culture Cells by Electron Microscopy and by Immunofluorescence Microscopy. *Proc. Natl. Acad. Sci. U. S. A.* **75**, 1820-1824, (1978).

39 Sugimoto, K., Williamson, R. E. & Wasteneys, G. O. New Techniques Enable Comparative Analysis of Microtubule Orientation, Wall Texture, and Growth Rate in Intact Roots of Arabidopsis. *Plan Physiol* **124**, 1493-1506 (2000).

40 Dyachok, J., Yoo, C.-M., Palanichelvam, K. & Blancaflor, E. in *Cytoskeleton Methods and Protocols* Vol. 586 *Methods in Molecular Biology* (ed Ray H. Gavin) Ch. 8, 157-169 (Humana Press, 2010).

41 Wasteneys, G. O., Willingale-Theune, J. & Menzel, D. Freeze shattering: a simple and effective method for permeabilizing higher plant cell walls. *J. Microsc-Oxford* **188**, 51-61, (1997).

42 Leung, B. O. & Chou, K. C. Review of Super-Resolution Fluorescence Microscopy for Biology. *Appl. Spectrosc.* **65**, 967-980, (2011).

43 Gutierrez, R., Lindeboom, J. J., Paredez, A. R., Emons, A. M. & Ehrhardt, D. W. Arabidopsis cortical microtubules position cellulose synthase delivery to the plasma membrane and interact with cellulose synthase trafficking compartments. *Nat. Cell Biol.* **11**, 797-806, (2009).

44 Jacques, E. *et al.* MicroFilament Analyzer, an image analysis tool for quantifying fibrillar orientation, reveals changes in microtubule organization during gravitropism. *Plant J* **74**, 1045-1058, (2013).

45 Kropf, D. L., Bisgrove, S. R. & Hable, W. E. Cytoskeletal control of polar growth in plant cells. *Curr. Opin. Cell Biol.* **10**, 117-122, (1998).

46 De Vos, D. *et al.* Towards mechanistic models of plant organ growth. *J Exp Bot* **63**, 3325-3337 (2012).

47 Baluška, F., Mancuso, S., Volkmann, D. & Barlow, P. W. Root apex transition zone: a signalling–response nexus in the root. *Trends Plant Sci* **15**, 402-408, (2010).

48 Sozzani, R. & Iyer-Pascuzzi, A. Postembryonic control of root meristem growth and development. *Curr Opin Plant Biol* **17**, 7-12, (2014).

49 Takatsuka, H. & Umeda, M. Hormonal control of cell division and elongation along differentiation trajectories in roots. *J Exp Bot* **65**, 2633-2643, (2014).

50 Shaw, S. L. & Lucas, J. Intrabundle microtubule dynamics in the Arabidopsis cortical array. *Cytoskeleton* **68**, 56-67, (2011).

51 Shaw, S. L., Kamyar, R. & Ehrhardt, D. W. Sustained microtubule treadmilling in Arabidopsis cortical arrays. *Science* **300**, 1715-1718, (2003).

52 Burian, A. *et al.* A correlative microscopy approach relates microtubule behaviour, local organ geometry, and cell growth at the Arabidopsis shoot apical meristem. *J Exp Bot* **64**, 5753-5767 (2013).

53 Thompson, R. E., Larson, D. R. & Webb, W. W. Precise Nanometer Localization Analysis for Individual Fluorescent Probes. *Biophys. J.* **82**, 2775-2783, (2002).

Tables

Table 1. Comparison of densities of CMT at different regions in plant root.

P-value	*a*	*b*	*c*	*d*	*e*	f_1	f_2	g_1	g_2
a		.0011							
b			.0059						
c				0.1767					
d					0.0001				
e						.6499	.0011		
f_1							.0025	.0001	.0001
f_2								.2499	.7527
g_1									.2220
g_2									

T-test of densities of cortical microtubules between adjacent regions (***a-g***) highlighted in Fig. 5. Cells or regions with densities of cortical microtubules not significantly different ($P > 0.1$) are highlighted in light blue in the table.

Figures

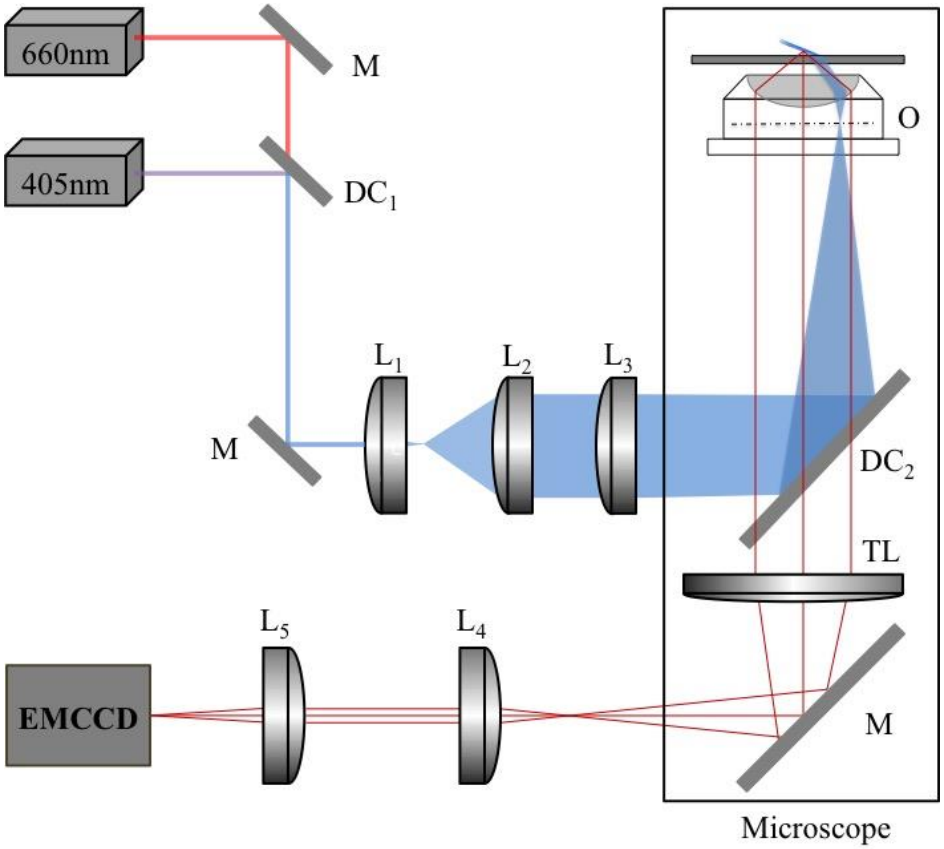

Figure 1. Schematic diagram of the setup for VAEM-STORM imaging. Multiple lasers were collimated by using dichroic mirrors DC_1. Collimated lasers were first expanded with two achromatic lenses L_1 (Thorlabs, AC127-025-A) and L_2 (Thorlabs, AC254-150-A) and then focused by an achromatic lens L_3 (Thorlabs, AC508-200-A) at the back focal plane of an oil objective O (N.A. = 1.49). Dotted-dashed and solid lines represent the back focal plane of O and the sample-imaging plane respectively. The single molecule images generated by the objective and tube lens (TL) were imaged by an Andor iXon+ 897 EMCCD camera via a pair of relay lenses L_4 and L_5 (Thorlabs, AC254-125-A). Emission filters are inserted between L_4 and L_5 to exclude scattering background. A highly inclined illumination condition was achieved via lateral shifting of the position of L_3, which was mounted on a motorized 3D stage.

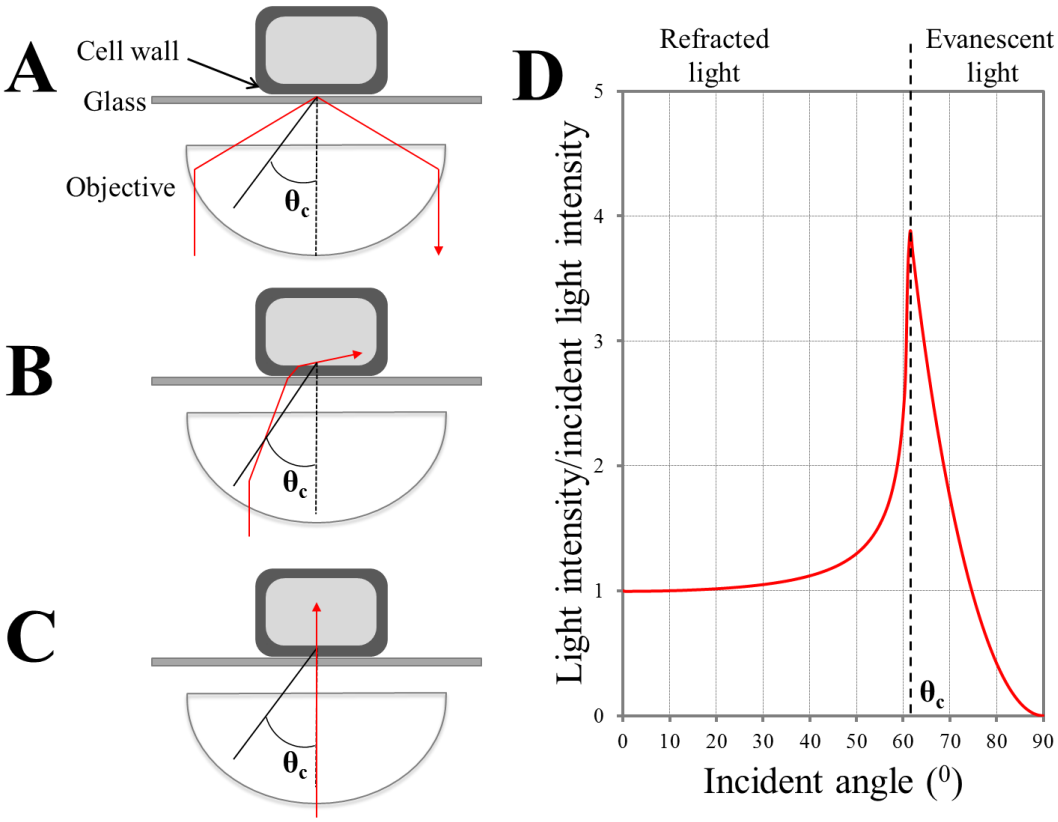

Figure 2. Comparison of laser beam paths. Comparison of the laser beam paths of total internal reflection fluorescence (TIRF) (A), variable angle epi-fluorescence (VAE) (B) and epi-fluorescence (C) illumination. In VAE geometry, the incident angle of the laser beam is slightly smaller than yet very close to the critical angle. The illumination depth is adjusted by scanning the subcritical angles to achieve the illumination condition giving the best signal to noise ratio. (D) Theoretical light intensity on the coverslip-specimen surface at the specimen side, when a beam is introduced from the glass side, as a function of the incident angle. At $\theta < \theta_c$, the laser beam is refracted. At $\theta \geq \theta_c$, the beam is totally internally reflected. Within about 10^o from the critical angle, the light intensity on the specimen side is larger than that of the incident laser beam. When the incident angle is increased up to the critical angle, the intensity of refracted light increases due to the reduced thickness of the refracted beam at large incident angles. This

provides the necessary pre-condition for tuning the switching properties of dye molecules. At the critical angle, the laser intensity of the evanescent field is about four times higher than the incident beam. This is because the light intensity at the surface is the sum of the incident and reflected beams whose phases are the same. Therefore, the electric field of the total light doubles while the light intensity increases by a factor of four, which is the square of the electric field. As the incident angles become larger than the critical angle, the phases of the incident and reflected beams are different, thus the light intensity of the evanescent field decreases.

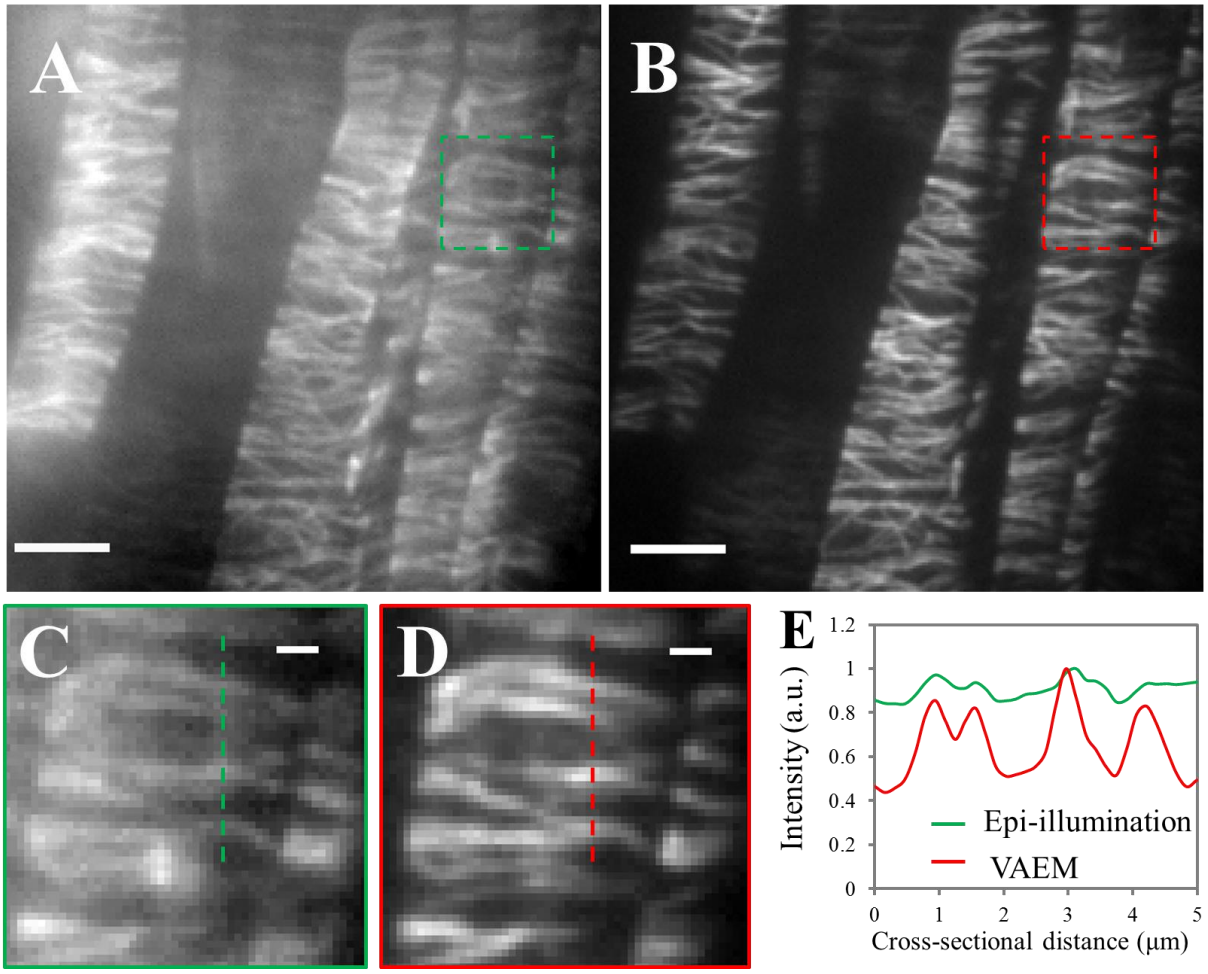

Figure 3. Comparison of S/N between epi-fluorescence illumination and VAE illumination. Imaging of Alexa Fluor 647-labeled cortical microtubules under epi-fluorescence (A) or VAEM (B). Images are acquired for epi-fluorescence and VAEM imaging using the same excitation intensity at 660 nm (3.5 kW/cm2) and same exposure time (50ms). The corresponding close-up images (C, D) show that the background due to out of focus contributions in VAEM is greatly reduced compared to epi-fluorescence. (E) Cross-sectional profiles at the same location show the dramatically enhanced S/N in VAEM compared to epi-fluorescence. Scale bar: 5 μm (A, B) and 1 μm (C, D).

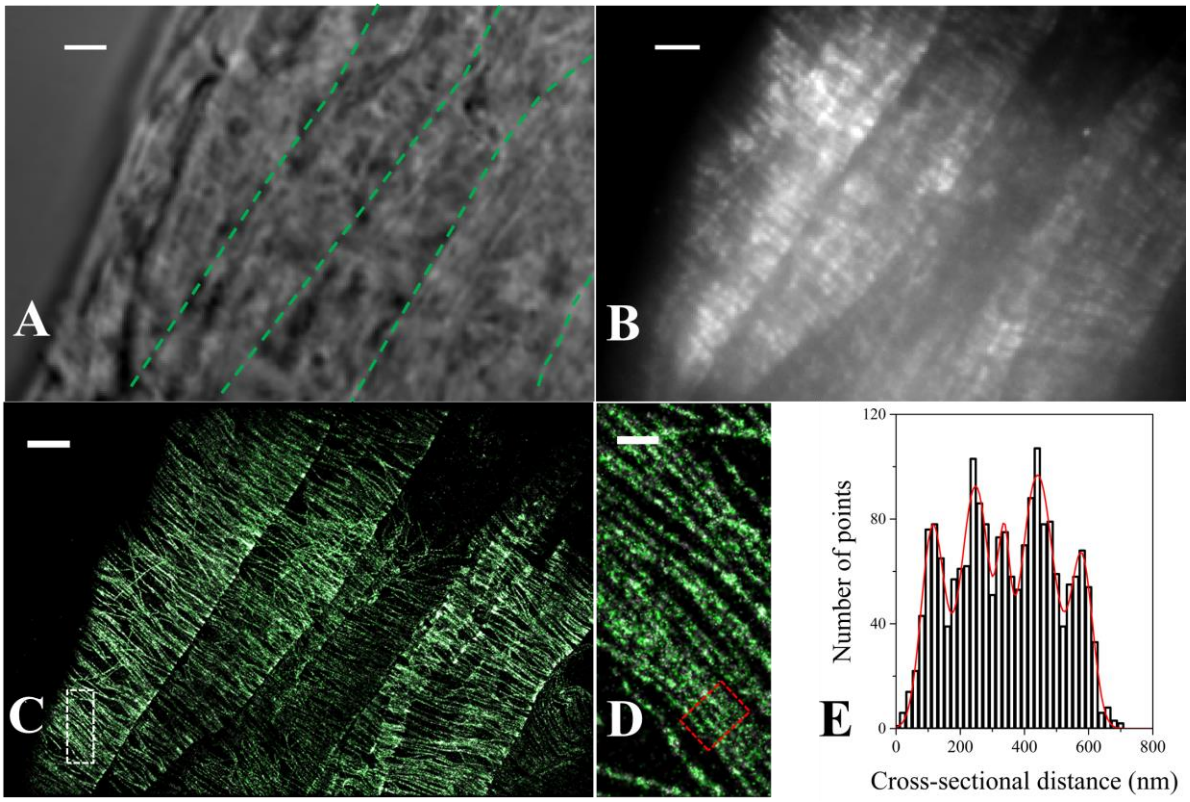

Figure 4. VAEM-STORM imaging of the cortical microtubule network of intact epidermal plant cells in the elongation zone of an Arabidopsis root tip. (A) Bright field image of cells at the elongation zone. The cells shown here are also highlighted in Fig. 5A as region d. The boundary between cells is highlighted with green dashed lines in the bright field image. (B) Epi-fluorescence image of the dense cortical microtubule network in the elongating cells and (C) the corresponding STORM image. (D) Zoomed-in STORM image as indicated in the white region in (C). (E) Cross-sectional profiles of a microtubule bundle in the cell [highlighted in the red box in (D)]. The histogram shows the cross-sectional distribution of the positions within the region specified by the red box. The red line is the fitting result from five simple Gaussian functions showing the centers of individual microtubules that are 80.0 nm ~ 137.9 nm apart. Scale bar: 3 μm (A-C) and 500 nm (D).

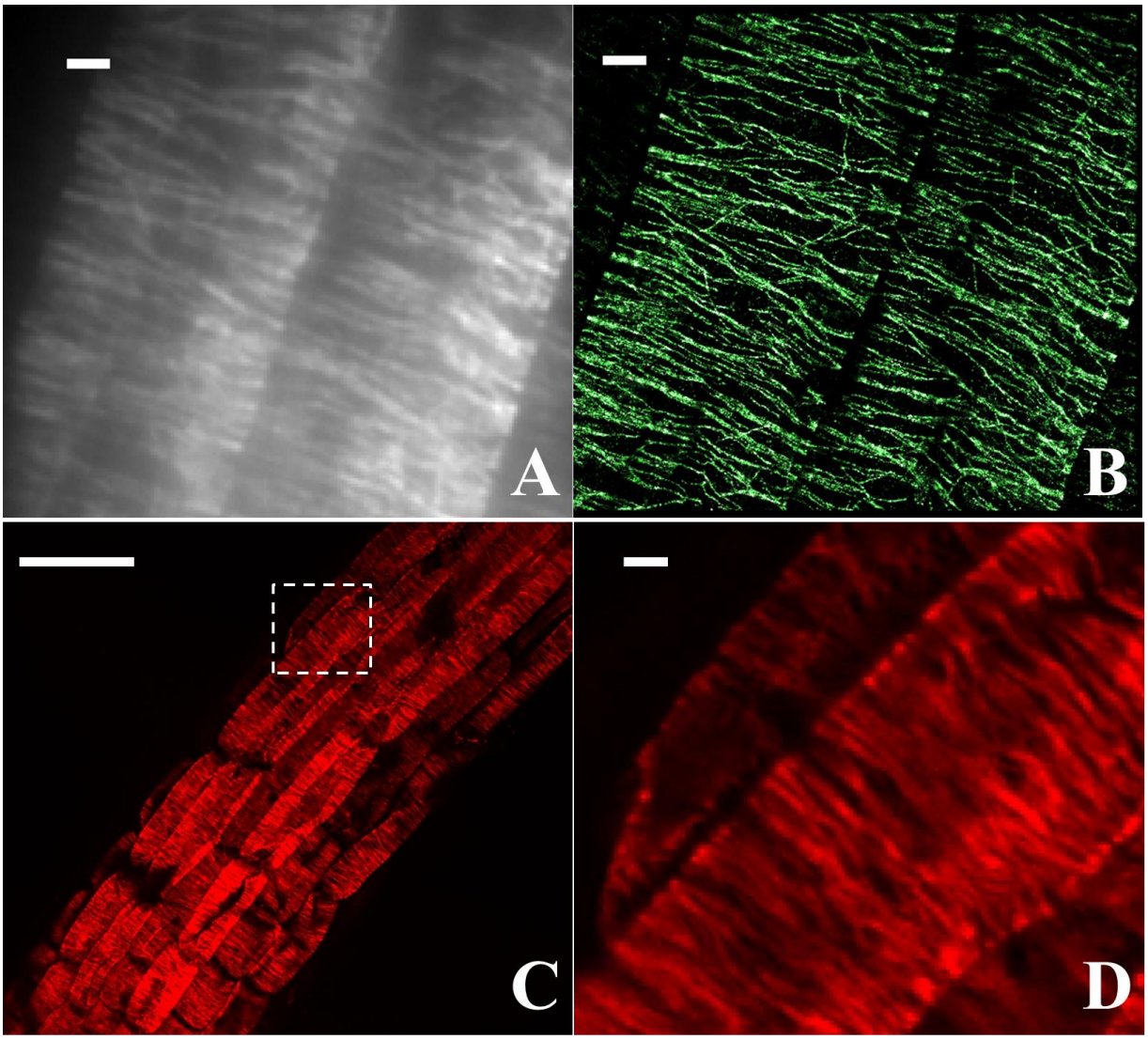

Figure 5. Diffraction unlimited resolution in VAEM-STORM imaging compared to diffraction limited imaging of cortical microtubules in plant cells in the elongation zone. (A) Epi-fluorescence image and (B) STORM image of the same area. (C) Confocal image and (D) zoomed-in image showing the highly packed cortical microtubules in plant cells. Compared to the images taken by epi-fluorescence microscopy and confocal microscopy, where close cortical microtubules are not resolvable, the structure and organization of the cortical microtubules in the STORM images are much clearer and better resolved. Scale bar: 2 μm (A, B, D) and 50 μm (C).

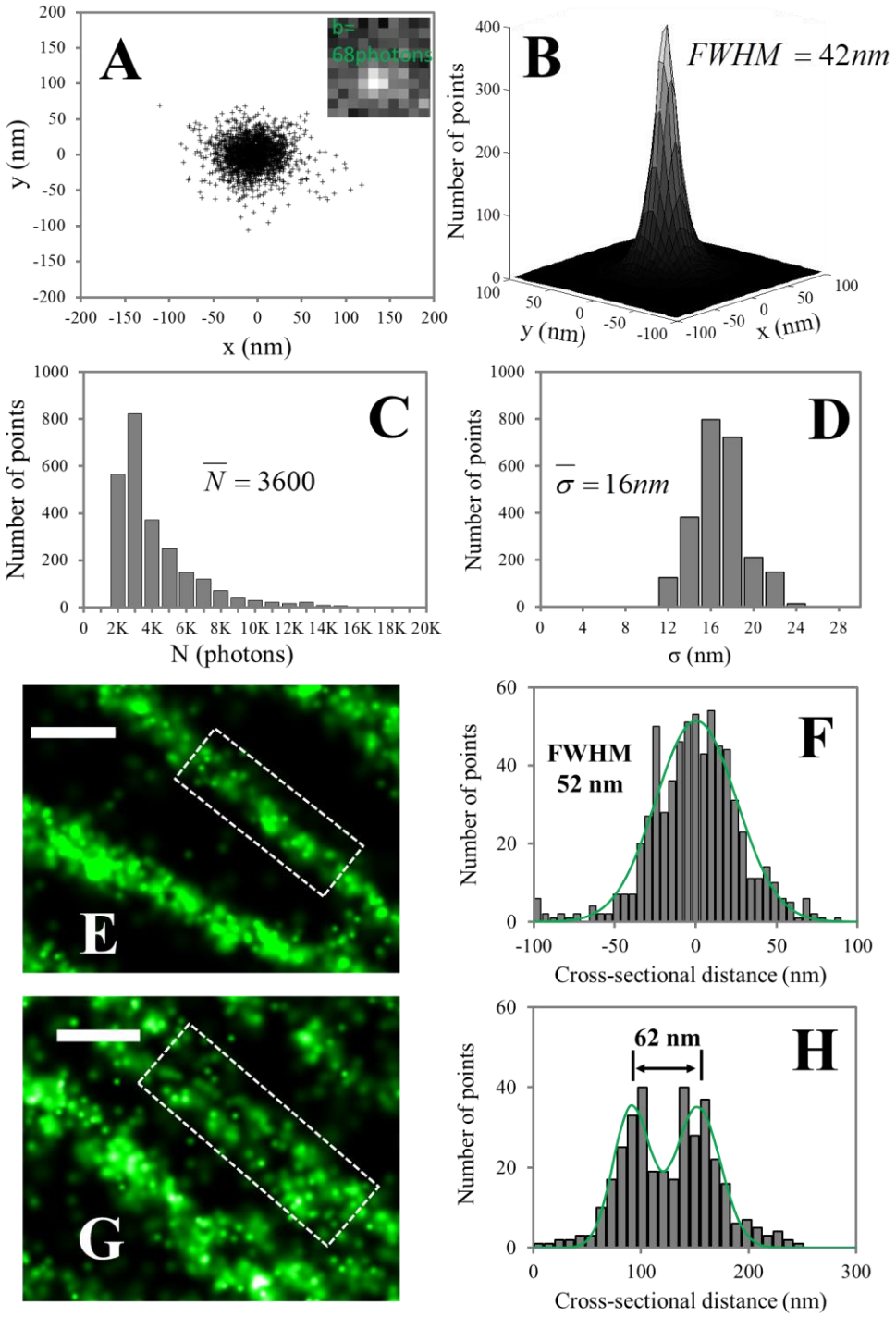

Figure 6. Estimation of the spatial resolution of VAEM-STORM imaging in intact Arabidopsis root tip cells. (A) Point-like objects appearing as clusters in the STORM image were used to directly determine the localization accuracy, thus estimating the spatial resolution.

Inset shows a single molecule image in one frame. (B) The localization distributions of clusters. A histogram of the distributions of locations in 2D was generated by aligning about 30 clusters by their center of mass. The distribution was then fitted with a simple Gaussian function for determining the FWHM of 42 nm, which was used as the resolution for STORM imaging. (C) Photon numbers and (D) localization accuracies of Gaussian fitting of single molecule images from the same clusters as in (B). The typical image parameters, including the background noise b (68 ± 24 photons) and collected photons N from single molecules in their switching cycles (3,600 ± 1,297 photons), were determined. As expected, the background noise in plant cell imaging is much higher than in animal cell imaging in which b is almost negligible. Nonetheless, the collected N is sufficiently large to ensure highly accurate localization. The localization precisions are calculated for each localized molecule following previously established methods (see Materials and Methods). The average localization precision from a histogram of over 2,000 positions is 16.0 ± 2.2 nm. (F) The apparent width of a single free microtubule is ~50 nm from fitting the cross-sectional profiles of locations (white box, E, zoomed-in image are extracted from Fig. 1C) with a simple Gaussian function. The average apparent width of over 20 single free microtubules is 57 ± 4 nm (data not shown). The apparent microtubule width is a result of the actual size of the microtubule plus staining antibodies and the sub-50-nm imaging resolution. (G) VAEM-STORM imaging provides details of microtubule bundling structures in plant cells. (H) Microtubule bundles composed of two single microtubules (white region, G, zoomed-in image are extracted from Fig. 1C) with 62 nm separation are clearly resolved in STORM images. Space between individual microtubule filaments varies from 50 nm – 120 nm[33] in animal cells and 20 nm – 40 nm in Arabidopsis cells[34] depending on the crosslinking structures. The separation distance is larger as a result of broadening effects due to antibody sizes and the spatial resolution. Scale bar: 200 nm.

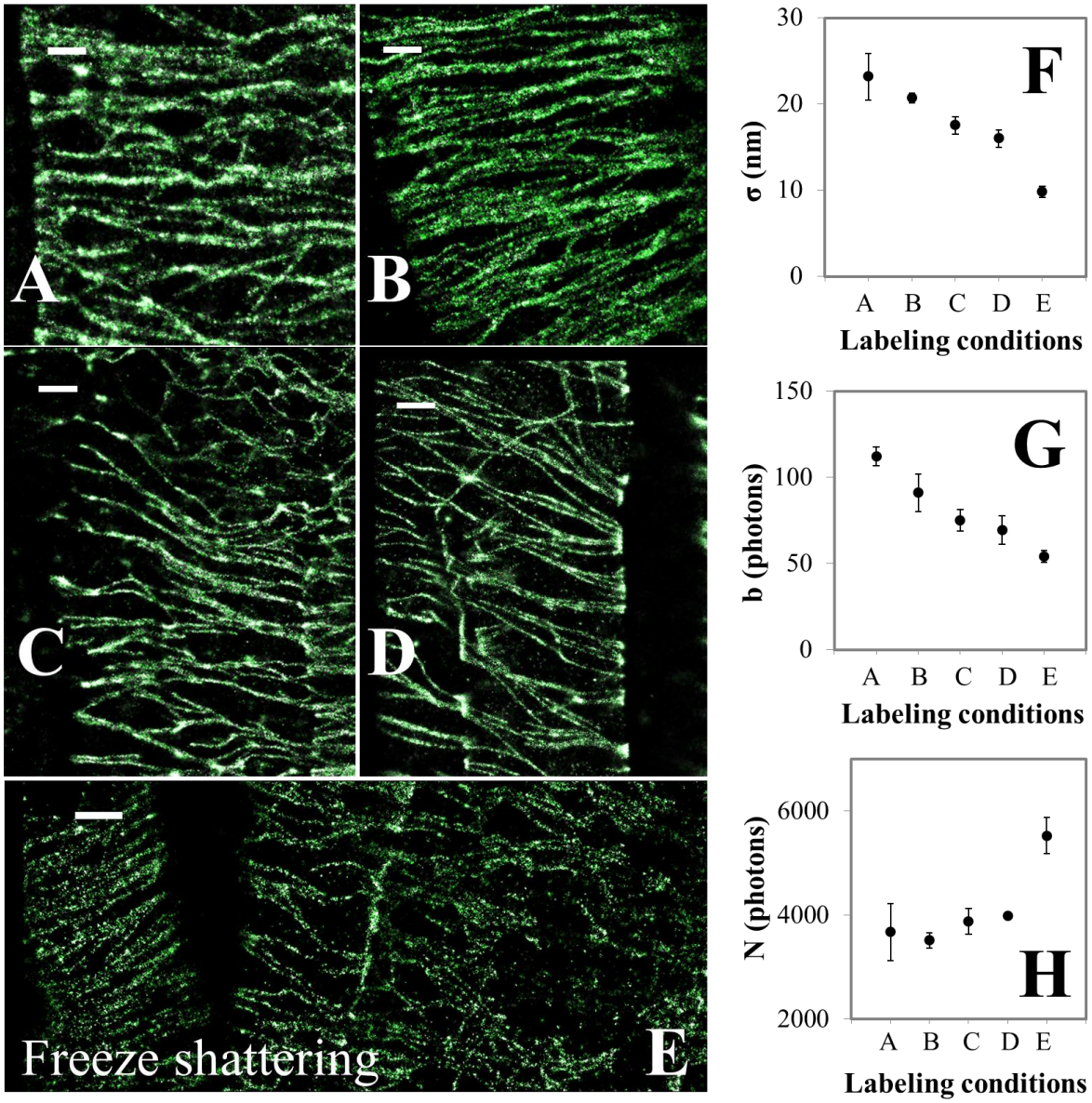

Figure 7. Proper labeling density of cortical microtubules by antibody-conjugated dye molecules is critical for generating super resolution images with sub-50nm-spatial resolution. Cortical microtubules in Arabidopsis root cells were first labeled with mouse anti-α-tubulin antibody, followed by goat anti-mouse F(ab')$_2$ fragments conjugated with Alexa Fluor 647. (A)-(D) STORM images using various concentrations of primary antibody and secondary antibody fragments are shown..(E) STORM image with sample preparation using the freeze-shattering process and with antibody concentrations the same as those in (D). The corresponding

localization precisions using clusters located between cortical microtubules (F), the local background in photon counts around the cluster (G) and the collected photon number of localized positions in the clusters (H) are shown. Scale bars: 1 µm.

	A	B	C	D
primary antibody (µg/mL)	2.0	1.0	2.0	1.0
secondary antibody (µg/mL)	0.20	0.20	0.04	0.04

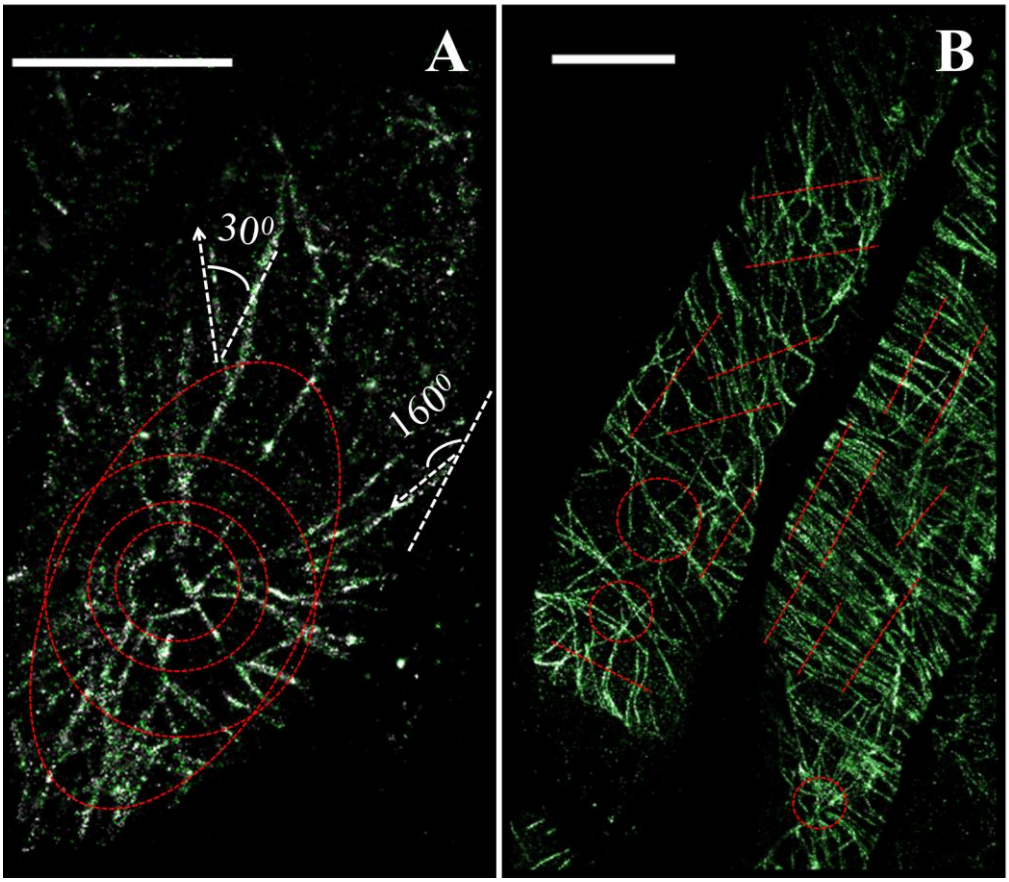

Figure 8. Quantitative information on the cortical microtubule network is readily available with a resolution of 20 – 40 nm in STORM images. (A) White dashed lines show the long axis of the plant root cell and white dashed arrows indicate the orientation of individual microtubule filaments. The orientation angles are taken as the angle of each microtubule filament relative to the long axis of the cell. Two examples of microtubule filaments are shown with orientation angle of 30º and 160º respectively. (B) These images demonstrate how the densities of cortical microtubules are measured. Since close microtubule filaments are easily resolvable, the densities can be determined by counting numbers of filaments along the cross-sectional or circular profiles (red dashed lines) depending on the local arrangement of the cortical microtubule network. Scale bars: 5 μm.

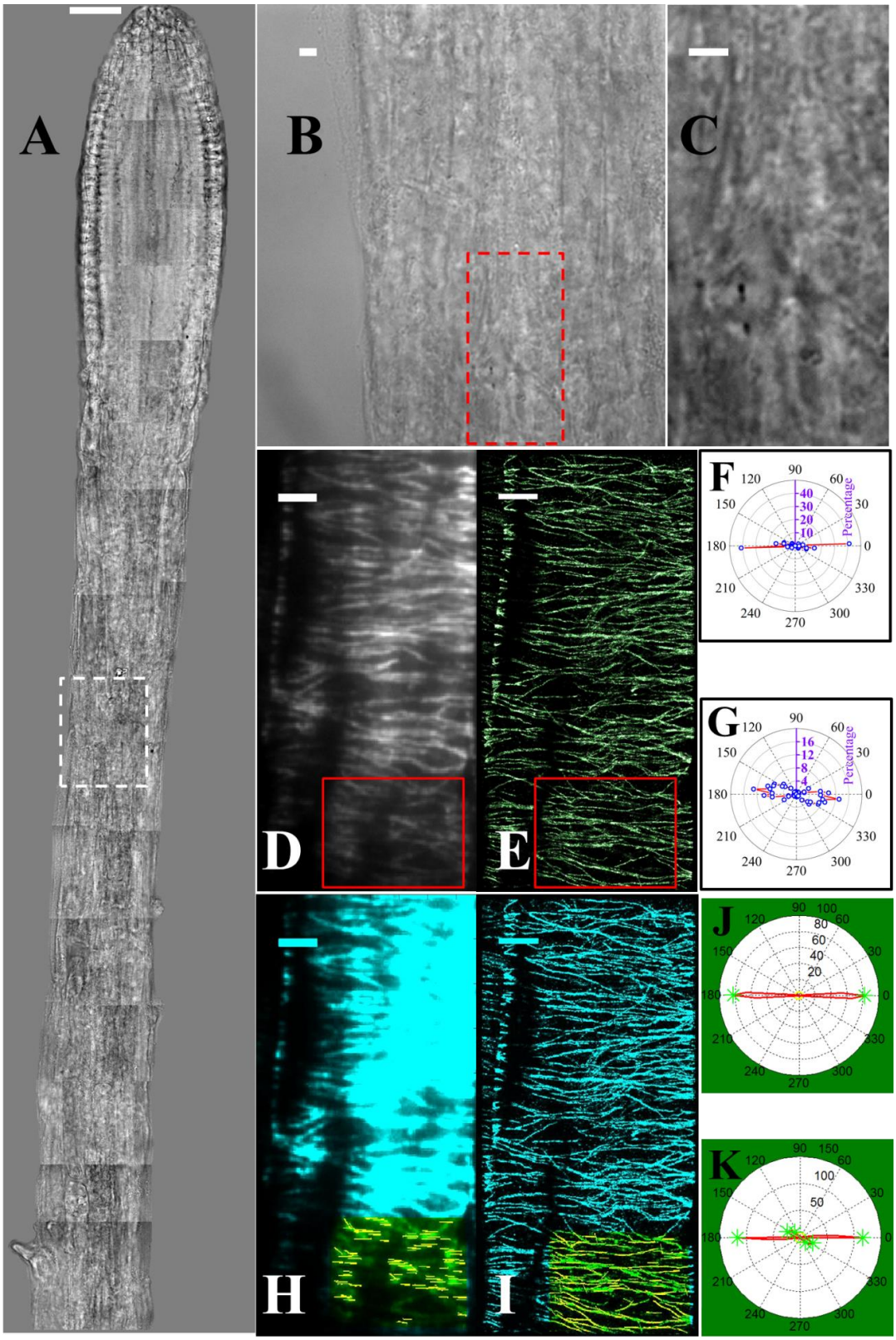
A
B
C
D
E
F
90
120
60
150
30
180
0
210
330
240
300
270
40
30
20
10
Persentage
G
16
12
8
4
Persentage
H
I
J
100
80
60
40
20
K
150
100
50

Figure 9. VAEM-STORM imaging of cortical microtubules in a plant epidermal cell of a whole intact root tip and orientation analysis. Analysis was performed both manually and using Microfilament Analyzer (MFA) software.[44] (A) Bright field image of the whole root tip. Image is a collage of individual images with the same optical setup (100× objective) as for epi-fluorescence and STORM imaging. The location of cells for STORM imaging in the whole root therefore can be easily determined from the bright field images under the same magnification. (B)-(C) Zoomed-in bright field images showing the location of cells used for STORM imaging. (D) VAEM image and (E) STORM image of the cells highlighted in the bright field image, corresponding to the red box in (B). (F)-(G) Polar plots of the orientations of microtubule filaments in the VAEM image (F) and STORM image (G) as highlighted in the red boxes in (D) and (E), respectively. The long axis of the cell is indicated by the purple axis in the polar plots. (H) - (K) Results of orientation analysis using the MFA software. The offset angle is 90^0 (long axis) and is not corrected in the polar plot, consistent with (F) and (G). Predominant angles are highlighted as green stars in the polar plot. Note that Figures (F-G) and Figures (H-K) are in different forms due to two different measuring methods. Scale bars: 30 μm (A) and 3 μm (B – I).

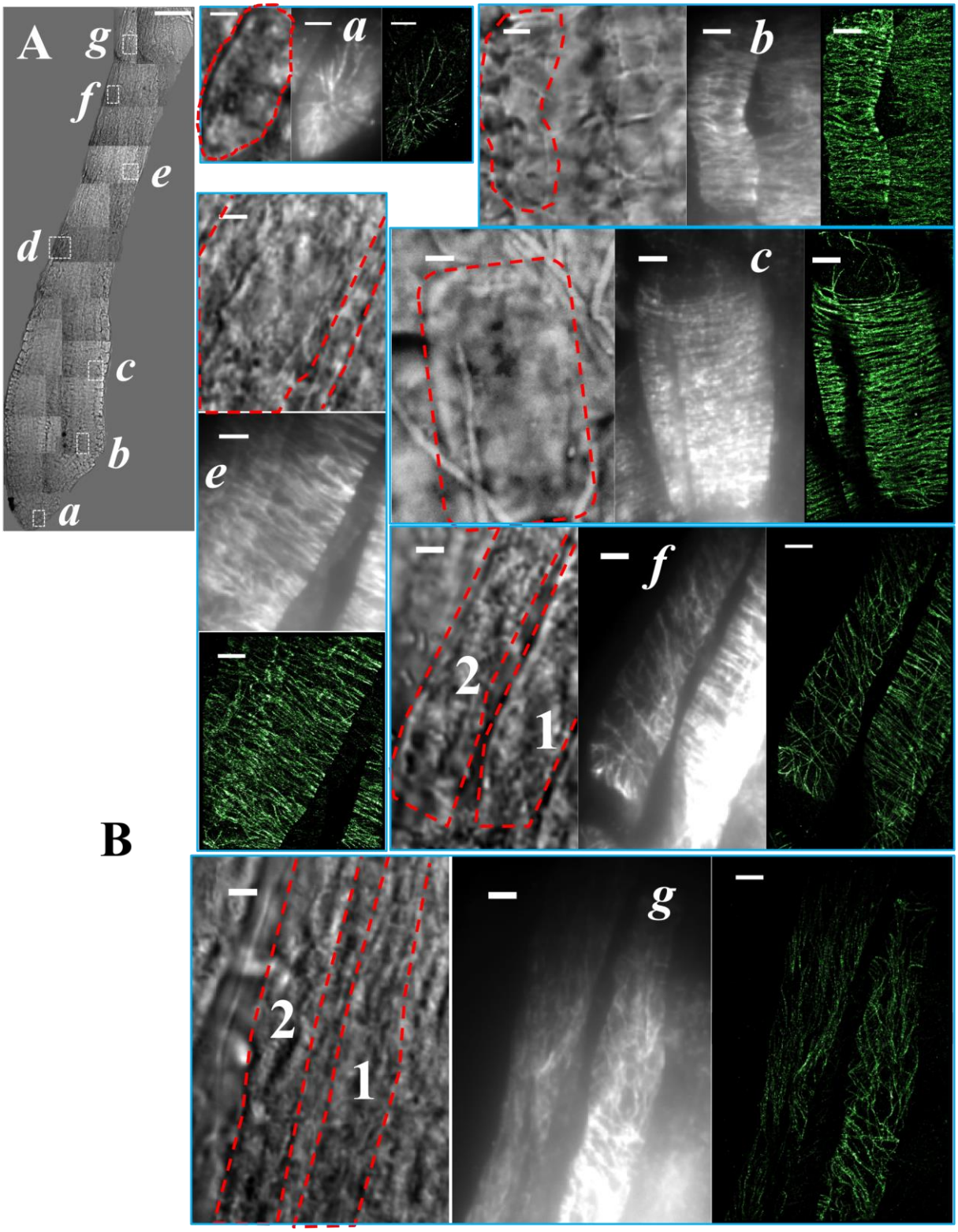
A
g
f
e
d
c
b
a
a
b
c
e
f
2
1
B
2
1
g

Figure 10. VAEM-STORM imaging of cortical microtubules in different parts of an intact Arabidopsis root. (A) Mosaic of bright field images of the root tip. Seven regions (***a-g***) across the root tip are highlighted and were chosen for dSTORM imaging. (B) Zoomed-in bright field and corresponding epi-fluorescence and STORM images of the white-boxed regions in (A). Images are shown of cortical microtubules of epidermal cells in meristematic (***a-b***), elongation (***c-e***), and differentiation (***f-g***) zones of the intact Arabidopsis root tip. Note that the zoomed-in bright field image, epi-fluorescence image and STORM image of cells in region ***d*** are shown in Fig. 2. Cell boundaries are highlighted with red dashed lines. Cells in regions ***f*** and ***g*** show distinct microtubule organization patterns, thus they are analyzed separately in Fig. 6 as f_1, f_2 and g_1, g_2 as indicated in the corresponding bright field images. Scale bars: 50 μm (A) and 3 μm (B, ***a-g***).

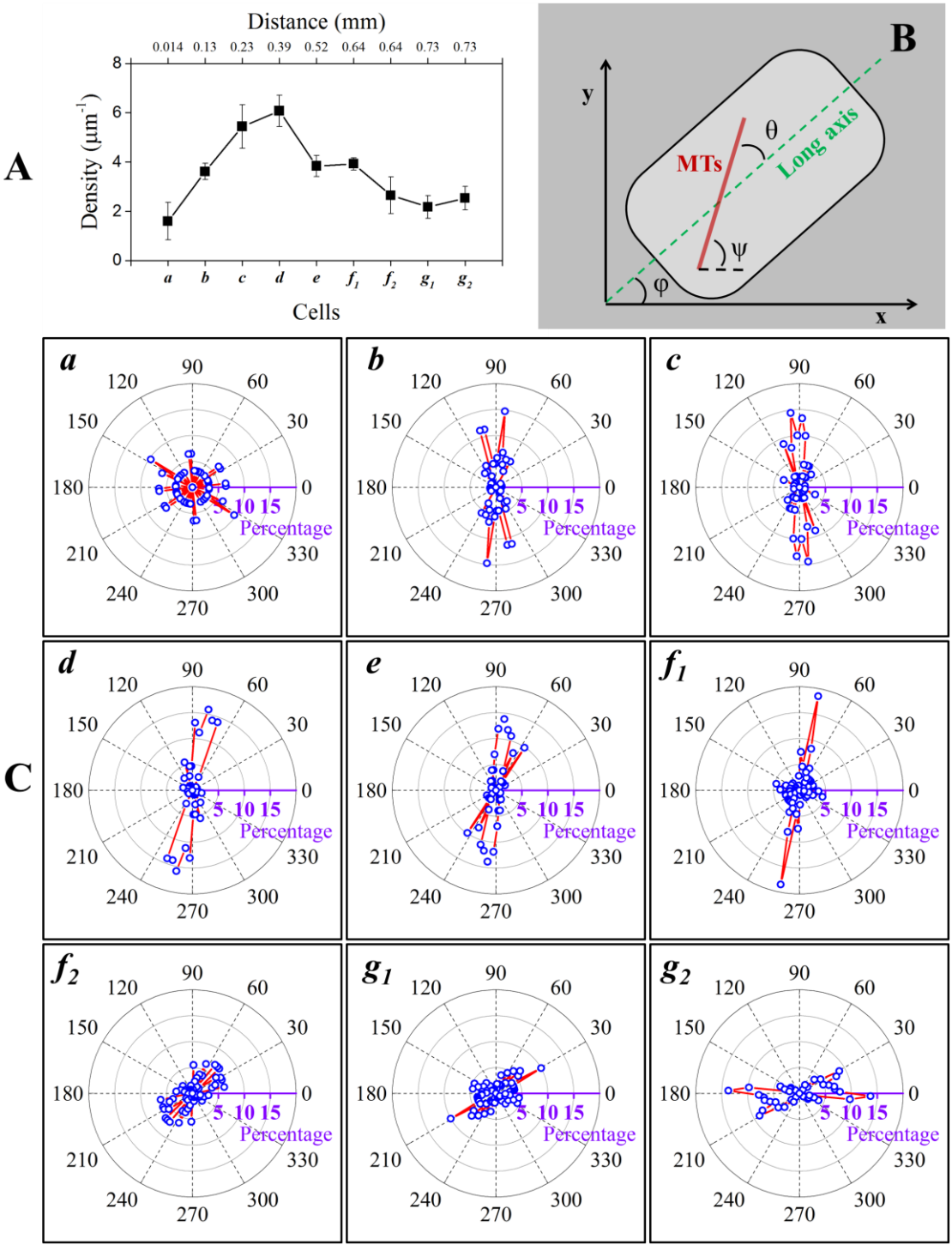

Figure 11. Quantitative analysis of the cortical microtubule network in a plant root tip. (A) The average cortical microtubule density (number of microtubules per micrometer) in the highlighted cells in Fig. 5, with the distance of cells from the root tip. Error bars represent the

standard deviation of densities of cortical microtubules from over 10 sub-regions in each cell. (B) Schematic representation of the orientation of cortical microtubules, taken as the relative angle (θ) of each microtubule filament to the long axis of the cell. The orientation angle θ as displayed in (C) is corrected by the offset angle φ of the cell, determined by its long axis. Ψ is the angle of the microtubule filament in the coordinates of the STORM image (x-y). All angles were determined by using NIH ImageJ (http://rsbweb.nih.gov/ij/). (C) Polar plots showing the distributions of cortical microtubule orientations (θ) of the corresponding cells in Fig. 4. Adjacent cells ($\boldsymbol{f_1}$ and $\boldsymbol{f_2}$, $\boldsymbol{g_1}$ and $\boldsymbol{g_2}$) showing dramatically different cortical microtubule organizations were analyzed separately. Note that the long axis of the cell has been aligned to the 3 o'clock position in all polar plots as highlighted in purple.

CHAPTER 3: STUDYING CHEMICAL REACTION, MOLECULAR TRANSPORTATION AND THEIR COUPLING IN CORE-SHELL CATALYSTS AT THE SINGLE-MOLECULE LEVEL

Bin Dong, Yuchen Pei, Chaoxian Xiao, Wenyu Huang, Ning Fang

A manuscript under peer review

Abstract

The emergence and advancement of super-resolution and super-localization fluorescence microscopy in the past decades had enabled researchers to reveal more detailed molecular dynamics and structural information from single molecule imaging. The application of single molecule localization based super-resolution imaging techniques in imaging chemical reactions had brought new insights of the reaction mechanism at single particle level void of the averaging effect in classical ensemble experiments. Heterogeneous properties of porous materials had been revealed in single molecule fluorescence microscopy. Here we synthesized a multilayer nanocatalysts composed of platinum nanoparticles sandwiched between an optically transparent solid core and a mesoporous shell with aligned pores. The catalytic reaction, molecular transportation and their coupling on the core-shell nanocatalysts were studied. Heterogeneity of the nanopore structure was revealed by single molecule imaging experiments.

Introduction

Optical microscopy imaging of single molecules, which reveals static and dynamic heterogeneities from seemingly equal molecules by removing the averaging effect in classical ensemble experiments, has played an important role in the investigations of fundamental biological and chemical processes at the molecular and nanoscale. The emergence of single molecule-based super-localization and super-resolution microscopy imaging techniques[1-4] in the past decade has introduced the critical ability of resolving individual molecule with nanometer scale accuracy and precision for revealing more detailed molecular dynamics and structural information. Nearly all of these technical advances were originally developed for biological studies.

More recently, however, efforts in super-resolution chemical imaging started to gain momentum. New discoveries that were previously unattainable with conventional diffraction-limited techniques have been made, such as super-resolution mapping of catalytic reactions on single nanocatalysts[5-16] and the mechanistic insight into protein ion-exchange adsorptive separations.[17] Moreover, super-localization based single particle tracking (SPT) methods had also been widely used to study the dynamic behaviors of single molecule in porous materials such as mesoporous silica nanomaterials[18-21] and reversed phase high performance liquid chromatography beads.[22,23] The sub-populations of immobile or temporally trapped molecules in the porous structure were used to reveal defects and other properties of the porous materials. Furthermore, single molecular trajectories also helped to uncover the alignment of pore structures with nanometer precision.

New insights on molecular transport and chemical reaction, and more importantly, their coupling, at the single molecule level in a wide range of length scales (from nanometer to tens of

micrometers) become increasingly interesting and important. However, most previous studies[7,10-12,16,18-22,24] dealt with these two important phenomena separately. Therefore, it is important to develop new methods to elucidate the coupling of molecular transport and catalytic reaction at the single molecule and single particle level. Herein, we applied an automated total internal reflection fluorescence microscope (TIRFM) to study the molecular transport and catalysis in high-performance core-shell catalysts.[25] The core-shell catalysts were composed of a 3D sandwiched structure in which platinum (Pt) nanoparticles (NPs) were located between an optically-transparent spherical solid SiO_2 core and a mesoporous SiO_2 shell with aligned pores. The fully optimized automated TIRFM enables us imaging fluorescent molecules with high signal to noise ratio (SNR) and thus allowing us to localize the molecular positions with sub-10-nm precision. The results from analyzing single molecular trajectories showed that resorufin molecule diffuses much slower in a nanopore than it is in a free aqueous solution. Moreover, three characteristic diffusional behaviors were also observed indicating the heterogeneous environment inside the nanopore. Analysis of the time dependence of all three sets of diffusion coefficients on different lag time revealed that resorufin molecules were undergoing both fast free motion and slow motions with restriction.

Results and Discussion

Imaging chemical reaction, molecular transportation and their coupling in core-shell catalysts

The core-shell catalysts which have highly tunable complex structures with well-defined geometry and manageable complexity were synthesized following the procedure as described in Fig. 1. The synthesized core-shell catalysts consist of Pt NPs, sandwiched in between an

optically transparent solid SiO_2 core and a mesoporous SiO_2 shell (Fig. 2). The Pt NPs have an average size of 2.9 nm and the SiO_2 core sphere is about 200 nm in diameter. The well-aligned nanopores in the mesoporous SiO_2 shell have an average length of 110 nm. Since the catalytic reaction takes place on the surface of Pt NPs, a reactant molecule needs to diffuse through the nanopores in order to get contact with the surface of Pt NPs. The life cycle of a product molecule in a core-shell mesoporous nanocatalyst refers to the following events and processes: 1) Desorption of the product molecule from the surface of Pt NP. 2) Free diffusion in nanopores. 3) Adsorption/desorption of the product molecule on the inner surface of nanopores. 4) Moving out of the nanopore and leaving the evanescent field of TIRFM. After the fluorescent product molecule leave the evanescent field of TIRFM, the fluorescence signal vanishes completely. The oxidation of non-fluorescent amplex red into fluorescent resorufin (Fig. 3a) is used here as a model reaction to study the aforementioned events and processes. The nanopores in the porous silica shell confine the diffusion of the generated fluorescent molecules.

TIRFM is arguably the most successful mode of fluorescence microscopy to be applied in studies of molecular dynamics, including diffusion[26-28] and absorption,[29,30] at liquid/solid interfaces. Under TIR illumination the incident angle of light is varied upon a material of a high index of refraction (n_1). At angles beyond the critical angle, the incident light is completely reflected and an evanescent wave is created in the adjacent medium (n_2), which must have a lower index of refraction than n_1. The penetration depth of the evanescent wave varies with the angle of incidence, the wavelength of light, and the indices of refraction of the two media. The TIR geometry provides excellent background rejection for interfacial measurements. However, it is worthwhile to note that the dimension (~ 400 nm in height) of the core-shell catalysts used here is significantly larger than those in the previous works such as gold-semiconductor hybrid

nanocatalysts[10] (< 10 nm in height). This makes finding the optimal illumination conditions more challenging in our experiments since the depth of the evanescent field generated under TIR illumination (limited to a few hundred nanometers) is comparable to the height of the nanocatalysts. To get the best performance (i.e., maximum illumination depth and highest SNR) out of TRIFM, we used an auto-calibrated scanning-angle TIRFM setup (Fig. 4) that had been accomplished with an optimized system layout and an automatic high-precision calibration procedure [31,32]. A computer program developed in-house was used to find the incident angles in the full range with an interval as small as ~0.1°. The entire auto-calibration procedure can be finished within minutes. The automated operation allows us to find the truly optimized illumination conditions and achieve the best possible SNR in single molecule detection, which is crucial for localizing the positions of fluorescent resorufin molecules when they are diffusing in the nanopores. Sub-10-nm localization precision (Fig. 3b) can be achieved at an exposure time of 50 ms under the fully-optimized *automated* TIRFM. Such high localization precision makes it possible to determine the entire trajectory of a resorufin molecule from the initial position on the SiO_2 core (catalytic reaction site) to the final position where it disappears at the outer edge of a nanopore.

Molecular transportation in nanopores

Fig. 5a shows an example of the catalytic cycle of the oxidation of amplex red and the dynamic transportation of a resorufin molecule in a nanopore. In the recorded movies the generated fluorescent resorufin molecule shows a relatively stable fluorescence intensity, which indicates a horizontal alignment of this specific nanopore in the core-shell catalyst. The fluorescence intensity in the final frame is weaker than the rest of images, which is most likely

due to the fluorescent molecule escaping the nanopore and diffusing beyond the illumination depth of the evanescent field within the exposure time of 50 ms.

Super-localization microscopy allows us to pinpoint the locations of fluorescent molecules in the nanopores with high precision. The distribution pattern of single molecule images can be fitted by a two-dimensional Gaussian function, which is commonly used as a close estimation of the point spread function in optical microscopy. The centers of the fluorescent molecules can be extracted with a sub-10-nm precision from the fitting parameters. The high localization precision allows us to construct the trajectory of the fluorescent resorufin molecule in the nanopore as shown in Fig. 5c. The spatial and temporal information of the catalysis cycle of oxidation of amplex red is thus readily available from the single molecular trajectory.

The reactant molecule amplex red was first transferred into the product molecule resorufin on Pt NPs that corresponds to the first 3 frames of the recorded movie. Then the fluorescent resorufin molecule diffused away after desorption from the surface of Pt NPs. Instead of quickly diffusing out of the nanopores, the fluorescent molecule was trapped in nanometer region as it shows relatively slow motions. The “trapping” event could be caused by the interaction between the resorufin molecule and nanopore’s inner surface. The heterogeneous behavior of molecular transport reflects the inhomogeneity of the inner surface of nanopores. Once the resorufin molecule stepped out of the trapping region, it moved smoothly along the nanopore and eventually escaped out of nanopore.

Stage drift is an important factor in super-resolution and super-localization imaging experiments. In order to rule out any possibility that the trajectory the resorufin molecule is arbitrary as the result of stage drift, images of fluorescent beads which worked as fiducial marker for stage drift correction in long-term imaging were extracted during the same imaging period of

tracking the resorufin molecule in nanopore (Fig. 5b). The constructed trajectory of the locations of fluorescent beads was shown in Fig. 5d. The movement of fluorescent beads is insignificant compared to the recorded traces of diffusing resorufin molecules. Therefore, we can confidently rule out the influences of stage drift to the trajectory of the resorufin molecule diffusing in nanopore.

The transportation of resorufin molecules in nanopores can be quantified through analyzing the distribution of step size (r) in single-molecule trajectories. The diffusional behavior of resorufin molecules in nanopores can be obtained with high accuracy from single molecule trajectories by examining the distributions of step size.[20] One of the benefits of such analysis is that a large number of single molecule trajectories similar to the one shown in Fig. 5c can be used to draw conclusions on statistical significance. The distribution of step size of resorufin molecules in nanopores, as shown in Fig. 6a, exhibits a feature similar to Gaussian distribution indicating a random walk mechanism according to the central limit theorem.[33] Therefore, the histogram distribution in Fig. 6a was fit to a radial displacement probability density function of a random walk in one dimension (see more details in Materials and Methods). The yielded apparent square root of mean squared displacement ($\langle r^2 \rangle^{1/2}$) is 22.4 ± 0.5 nm. It is worthwhile to note that the displacement of resorufin molecules in nanopore is two orders of magnitude smaller than that in free aqueous solution (6.93×10^3 nm),[34] indicating that the movement of resorufin molecules in nanopore is much slower. This can be explained with the small size of the nanopore (2~3 nm) (Fig. 2d). We have also examined the movement of a fluorescent bead fixed on a quartz surface, which mainly reflects the uncertainty of localization (Fig. 6b). The distribution of step sizes was calculated using the trajectory of the fluorescent

bead after correcting for the stage drift. Compared to the resorufin molecules, the fluorescent bead shows insignificant movement during the imaging period.

Characterization of molecular trajectories in terms of diffusion coefficient

The molecular transportation in nanopore can be quantitatively described by calculating the diffusion coefficients (D), which can be readily obtained from the $\langle r^2 \rangle$ at interval time of t_{lag} according to the Einstein-Smoluchowski equation[35] (See Materials and Methods). However, the result from data for single t_{lag} is usually insufficient to fully describe the molecular diffusion in a confined environment. One needs to consider the long-term observation. For molecules following free random-walk motions, a linearly increasing of $\langle r^2 \rangle$ with the t_{lag} can be expected. On the contrary, for those restricted molecules, $\langle r^2 \rangle$ that is still well approximated in the same way is stationary at different t_{lag}. Therefore, the diffusion coefficient is better estimated by fitting the $\langle r^2 \rangle$ versus t_{lag}. There are commonly two ways to deduce $\langle r^2 \rangle$ from single molecular trajectories, namely fitting the histogram distribution of step sizes or fitting the cumulative probabilities. In practice, the result is more precise through the analysis of the cumulative probabilities instead of the histograms and loss of information by binning of the histogram can also be avoided. So we analyzed the single molecular trajectories by plotting the inverse of the cumulative probability ($C(r^2)$) of the squared step sizes (r^2) at different t_{lag}. The plotted data were then fitted with modified multi-exponential decay functions (See more details in Materials and Methods) giving of the mean squared displacement, which is the characteristic value of describing single molecular diffusion in nanopore.

Fig. 7a shows the cumulative probabilities versus squared step sizes at two different t_{lag} (0.05 s and 0.2 s resembled as square and triangle, respectively). The data here cannot be simply

fitted by mono-exponential decay function (red dash line in Fig 7a) with which only a single diffusion type is recovered. To best fit the data, it requires at least three individual components of exponential decays (red solid line in Fig. 7a) giving of three different mean squared displacements at each t_{lag}. This indicates that three types of diffusional behavior of resorufin molecules in nanopores can be revealed. To determine the diffusion coefficients of resorufin molecules in nanopores, different sets of mean squared displacements were plotted against the lag time (Fig. 7b). The data were then fitted with the Einstein-Smoluchowski equation for random diffusion in one dimension, giving diffusion coefficients of 0.022 ± 0.001 $\mu m^2/s$ (fast), 0.0068 ± 0.002 $\mu m^2/s$ (slow) and 0.0021 ± 0.0003 $\mu m^2/s$ (very slow). The large differences of these diffusion coefficients indicate that the resorufin molecule is moving in three main types of environment in nanopores. The resorufin molecules showing a fast diffusion behavior (the component with largest diffusion coefficient) are those diffusing in the free solution filled in nanopores. The resorufin molecules with smallest diffusion coefficient are likely temporally absorbed or trapped onto either the Pt NPs or the inner surface of nanopores. It is also possible that the resorufin molecules diffuse slowly on the inner surface (the component with intermediate diffusion coefficient) because of weak interaction between resorufin molecule and nanopore inner surface. Through these three characteristic diffusion behaviors of resorufin molecules in nanopores were deduced from the ensemble data of single molecular trajectories, it still holds true on individual molecular traces. For instance, all three types of diffusional behaviors of resorufin molecules in nanopores can be clearly resolved in Fig. 5c. The result here shows that the mobility of resorufin molecules in nanopores changes strongly along its pathway due to the heterogeneous environments. Nevertheless, we did not always see all three distinct types of diffusion in the same single molecular trajectory as shown in Fig. 8. In some nanopores

(Fig. 8c), only a single diffusion behavior is observed. Therefore, the analysis of single molecular trajectories demonstrates that the diffusion coefficient not only varies along the diffusion trajectory of the same resorufin molecule in individual nanopore but also changes among different nanopores. The heterogeneities of the nanopore structure in the core-shell could only be revealed by single molecule tracking methods and would have been obscured in ensemble experiments due to inevitable averaging effects.

To test whether the movement of resorufin molecules in nanopores actually follows free diffusion according to random-walk mechanism, the diffusion coefficients of all three components were calculated using Einstein-Smoluchowski equation (Table 1). The results were illustrated in Fig. 9. It clearly shows that the relationship between diffusion coefficients and lag time varies among three diffusion components. The fast diffusing resorufin molecules are nearly free since the diffusion coefficients stay same at different lag time. On the contrary, the other two slow diffusion components show decreasing diffusion coefficients as the lag time grows indicating that the molecule's movement is restricted. The restriction of the diffusion of resorufin molecules in nanopores can be physically described by introducing a factor α,[36,37] which is used to quantify the dependence of the diffusion coefficient on lag time. Γ is the transportation coefficient. The underlying mechanism is that the molecule diffuse freely at short observation periods but slows down at long observation time as a result of increasing effects of barriers or bindings. The base of this mechanism is that no average residence time of molecules per step can be obtained due to the broad distribution of association energies of interactions between resorufin molecules and the continuously changing environment in nanopores. The strength of restriction is quantified by α. For $\alpha = 1$, the diffusion of molecules is independent of lag time indicating that the molecules is undergoing free Brownian diffusion. The results from fitting the

time dependence of diffusion coefficients are shown in Fig. 9, giving of α values of 0.98 ± 0.02 (fast), 0.84 ± 0.07 (slow), and 0.66 ± 0.01 (very slow) and transportation coefficients of 0.084 ± 0.002 $\mu m^2/s$ (fast), 0.023 ± 0.003 $\mu m^2/s$ (fast), and 0.0062 ± 0.0001 $\mu m^2/s$ (fast). The fast mobile fraction of resorufin molecules diffusing in nanopores is close to free motions, while the two slow mobile fractions indicate that the diffusion of resorufin molecules is restricted at some degree. Therefore, the changing between free diffusion and restricted motion of resorufin molecules in nanopores of core-shell catalysts is in consistent with the heterogeneity of the pore structure not only among different nanopores but also within the same nanopore.

Conclusions

In summary, we studied the molecular transportation and on-site chemical reaction, and more importantly, their coupling at single molecule and single channel level in mesoporous core-shell catalysts. The catalysts used in this work have a complex, but well-defined geometry - Pt NPs sandwiched between an optically transparent solid SiO_2 core and a mesoporous SiO_2 shell with aligned pores. Fluorogenic oxidation of amplex red was used as a model reaction for studying catalytic reactions on the Pt NPs and molecular transportation in well-aligned nanopores. Under fully optimized automated TIRFM, the fluorescent product molecule, resorufin, was detected with high SNR thus allowing us to achieve sub-10-nm localization precision of single molecule image at a temporal resolution of 50 ms. The high localization precision enables us to track the full trajectory of a resorufin molecule from the initial position on the SiO_2 core (the site of catalytic reaction) to the final position where it disappears at the outer edge of a nanopore. Analysis of the single molecular trajectories reveals that the displacement of resorufin molecules in nanopores is much slower comparing to that in free

solution. Furthermore, the heterogeneity of motions of resorufin molecules along their pathways indicates the heterogeneity in the local environment inside the individual nanopores. The diffusion coefficients of resorufin molecules in nanopores were calculated to show at least three sub-populations of different molecular mobility. Analysis of the time dependence of diffusion coefficients on lag time has also led to the quantification of the degree of restriction on motions of resorufin molecules in nanopores. The source of restriction could come from both the initial adsorption of resorufin molecules on Pt NPs or the adsorption-desorption of resorufin molecules on the inner surface of nanopores. These results show the heterogeneity of nanopore structure can only be revealed by single molecule tracking method.

Materials and Methods

Synthesis of Multilayer Nanocatalysts

As shown in Fig. 1, monodisperse SiO_2 spheres are synthesized as the starting core via Stöber method.[38,39] The reason we choose SiO_2 as the core as well as the shell material is that it has excellent thermal stability, inert catalytic activity, tunable surface functionality, and optical transparency in the visible light region, meeting the requirement of our research. After purification by centrifugation, monodisperse SiO_2 spheres with an average diameter of 180 nm were obtained (Fig. 2). We polymerized 3-aminopropyltriethoxysilane (APTS) on SiO_2 surface to introduce $-NH_2$ groups. These $-NH_2$ groups enhance the binding between Pt NPs and SiO_2 spheres, and thus the loading efficiency.

Monodisperse 2.9 nm Pt NPs were synthesized by methanol reduction of chloroplatinic acid (H_2PtCl_6) in the presence of polyvinylpyrrolidone. These Pt NPs were loaded on NH_2-functionalized SiO_2 spheres by mixing them in ethanol. Pt loading amount was controlled to be

~2.5 wt%. As shown in Fig. 2c, Pt NPs were uniformly dispersed on the surface of SiO_2 spheres, owing to the strong interaction between Pt NPs and $-NH_2$ groups on the surface of SiO_2 spheres.

Finally, a mesoporous SiO_2 shell was grown on the surface of Pt NPs loaded SiO_2 spheres. Tetraethyl orthosilicate (TEOS) was used as the SiO_2 precursor and hexadecyltrimethylammonium bromide (C_{16}TAB) was used as the templating agent. The transmission electron microscopy (TEM) image in Fig. 2 shows a solid SiO_2 core of 180 nm in diameter and a uniform SiO_2 shell of 110 nm.

The SiO_2 spheres were loaded with Pt NPs before the mesoporous SiO_2 coating. The C_{16}TAB template in mesoporous SiO_2 was removed by refluxing in a mixture of methanol and concentrated hydrochloric acid. After removing the organic template, we noticed that the channels of mesoporous SiO_2 shell are aligned perpendicular to the surface of the SiO_2 core. The obtained nanostructure, Pt NPs confined between a solid SiO_2 core and an aligned SiO_2 mesoporous shell, imitates a *particle-in-well* structure. The aligned pore orientation is attributed to the self-assembly of C_{16}TAB surfactant and siliceous oligomer molecules occurring on the surface of preformed SiO_2 spheres.[40]

Optical setup for single molecule imaging at single particle level

An adjustable 50 mW 532 CW laser (Uniphase, San Jose, CA) was first collimated using a pair of lens and then focus into the interface between aqueous sample and quartz slide by a long working distance lens. An extra quarter wave plate (WPMQ05M-532, Thorlabs, Newton, NJ) was introduced into the optical path to switch the linear polarized laser beam into circular polarized laser profile. The fluorescence signal was collected by a 60 × oil immersion objective (N.A. = 1.4) and focused onto the Andor iXonEM$^+$ 897 camera (Belfast, Northern Ireland: 512 ×

512 imaging array, 16 μm × 16 μm pixel size). A fluorescent filter set composed of a 532 nm longpass filter, a 532 nm nortch filter and a 568/40 bandpass filter (Semrock, Rochester, NY) was inserted before the camera to reject scattering signal from the sample. There is an extra magnification after the imaging objective in the microscope giving an effective imaging pixel size of 213 nm.

The incident angle of laser beam at the interface was determined by the angle of the last mirror (controlled by a galvanometer), which was also in conjunction with a motorized linear stage (MAA-PP, Newport, Irvine, CA). The best illumination conditions achieves when the laser spot overlapped perfectly with the view field of the objective. For every incident angle, the best illumination condition was obtained by scanning the vertical position and the data was recorded in self-written program for later use. Therefore, we can fully optimize the imaging conditions to achieve maximum illumination depth while maintaining high SNR for every sample. It is worthwhile to notice that the whole process of optimization only take a few minutes.

Fluorogenic Oxidation Reaction on Single Nanocatalysts

In order to carry out the single-molecule imaging experiments on the multilayer mesoporous nanocatalysts, a fluorogenic oxidation reaction of non-fluorescent amplex red (10-acetyl-3,7-dihydroxyphenoxazine) to produce highly fluorescent resorufin (λ_{ex} = 563 nm; λ_{em} = 587 nm, at pH 7.5) (Fig. 3a) has been used. A sample is typically prepared by spin-casting the nanocatalyst solution on a poly-L-lysine functionalized quartz slide. The concentration of the nanocatalysts immobilized on the quartz slide is usually controlled to be 1 μm^{-2} for single particle catalysis. The sample slide is then measured under our automated prism-type TIRFM. A 532-nm green laser is used to excite the fluorescent resorufin product. The reactant-containing

solution (0.4 μM amplex red, 20 mM H_2O_2, and 50 mM pH 7.5 phosphate buffer) is introduced over the nanocatalysts within a flow chamber. Highly fluorescent resorufin product molecules are formed at one of many possible reactive Pt NPs on a single nanocatalyst.

Identify catalytic events from single molecular intensity traces

Fig. 10a is an example of fluorescent intensity trace of a mesoporous nanocatalyst in a short time period with an integration area of 10 pixels × 10 pixels. The catalytic events were resembled as bursts in the intensity trace. Fig. 10b is the fluorescent intensity trace of a nearby area time where no nanocatalysts exist during the same observation. The histogram distributions of both traces were showed in Fig. 10c. It is clearly observed that the intensity distribution is dominated by the fluorescent background which is in consistent with results that reaction bursts were sparsely and randomly distributed along the whole intensity trace (Fig. 10a). Nevertheless, the right shift to larger intensity values of the distribution (Fig. 10c, red) from the burst trace indicates the existence of catalytic events. In order to filter out the burst events from the whole fluorescent intensity trace efficiently, we first set up a low intensity threshold (blue dash line in Fig. 9a,b) of $I_{bg} + 2.5\sigma_{bg}$ where I_{bg} and σ_{bg} were the mean intensity and standard deviation respectively from fitting the intensity distribution of the whole trace (Fig. 10c). Then a second intensity threshold ($I_{bg} + 4\sigma_{bg}$, red dash line in Fig. 10a, b) was set to further examine the identified bursts. The summed intensities from all frames of identified bursts were first calculated and those below the high threshold were ejected as noise from background. The method of using two intensity thresholds allowed us to include catalytic events showing low fluorescent signal but last for a long period. The two thresholds were set to maintain 1% of uncertainty that the identified burst are actually from the background. Fig. 10d shows the

intensity distribution of identified fluorescent bursts (red) which is clearly separated with the background intensity distribution (black). The identification processes of fluorescent bursts were finished by using a self-written MATLAB script which enabled us to manage large amount of imaging data without artificial bias.

Localize the center positions of single molecules

The molecular positions in identified bursts were localized by using similar approach in the previous chapter. Briefly, the distribution of the fluorescent intensity was fitted by a 2D Gaussian function to determine the center position of the single molecule image (Fig. 3b). This process was repeated for localizing the positions of the fluorescent bursts in all frames. Single molecular trajectories could then be constructed using the molecular positions and used for latter analysis. The localization precision is inversely proportional to the square root of collected photons (N) emitted from the fluorescent probe and proportional to the background noise (b). As a benefit of largely reduced fluorescent background noise in TIRFM and using collection objective with high numerical aperture (N.A.), we can collect the single molecule image with high SNR thus allowing us to localize the molecular position with sub-10-nm precision. The localization precision is determined using the following equation.[41]

$$\boldsymbol{\sigma = \sqrt{\frac{s^2}{N} + \frac{a^2}{12N} + \frac{8\pi b^2 s^4}{a^2 N^2}}}$$

where s is the standard deviation of the Gaussian distribution that equals 1/2.2 of the PSF width, a is the pixel size, b is background noise and N is number of collected photons. The first term (s^2/N) is the photon noise, the second term is the effect of finite pixel size of the detector, and the last term is the effect of background. In the example shown in Fig. 3b, the center of resorufin

molecule is determined with precision of 8 nm given by the following parameters: s = 192 nm, a = 213 nm, N = 2063 photons and b = 15 photons. The high localization precision ensures us to visualize the whole process of the catalytic reactions and followed molecular transportation in nanopores. It is worthwhile to notice that the localization precision also varies depending on the location of catalytic event on the nanocatalysts. Resorufin molecules generated by the catalytic events happened on the bottom of the nanocatalysts gave higher fluorescent intensity thus their positions were localized with higher precision. The localization procedure was also accomplished by using a self-developed MATLAB script.

Global analysis of single molecular trajectories

The single molecular trajectories were studies through the mean squared displacement analysis. The step sizes (r) at lag time (t_{lag}) were first calculated from the molecular trajectories and grouped into a histogram showing the distribution of molecular displacement per t_{lag} (Fig. 6). For calculating the step sizes, every position on the trajectory was treated equally as a valid beginning point. Large data sets of single molecular trajectories were used for analysis in order to draw conclusions with statistical significance.

Under random-walk mechanism, the probability that a molecule from the origin will be found at time t within a shell of radius r and the thickness of dr is defined as $p(r,t)dr^2$ where $p(r,t)$ is probability density function.[33] Therefore, one can fit the distribution of the molecular step sizes with the probability density function:

$$\boldsymbol{p(r^2,t)\cdot dr^2 = \frac{1}{\pi\langle r^2_{(t)}\rangle}\exp\left(\frac{-r^2_{(t)}}{\langle r^2_{(t)}\rangle}\right)2\pi r\cdot dr^2}$$

where $\langle r^2 \rangle$ stands for the mean square displacement. Fitting the histogram distribution in Fig. 6a giving of a $\langle r^2 \rangle^{1/2}$ of 22.4 ± 0.5 nm. In practice, the $\langle r^2 \rangle$ is better determined by fitting cumulative probability of the distribution of step sizes rather than the grouped histogram due to the loss of information from binning.

$$\boldsymbol{P(r^2, t) = \int_0^{r^2} p(r^2, t) \cdot dr^2 = 1 - \exp\left(\frac{-r^2_{(t)}}{\langle r^2_{(t)} \rangle}\right)}$$

$$\boldsymbol{C(r^2, t) = 1 - P(r^2, t) = \exp\left(\frac{-r^2_{(t)}}{\langle r^2_{(t)} \rangle}\right)}$$

Therefore, one can use the inverse cumulative probability function, $C(r^2)$, which is a simple exponential decay function to fit the probability data. However, it can be clearly seen that a single component fitting is insufficient to describe the overall distribution (Fig. 7a). Thus multi-component exponential decay functions were used to fit the data.

$$\boldsymbol{C(r^2, t) = \sum_{i=1}^{n} c_i \exp\left(\frac{-r^2_{(t)}}{\langle r^2_{i(t)} \rangle + \sigma^2}\right)}$$

In the equation, c_i is the amplitude of the different exponential components, $\boldsymbol{\sum c_i = 1}$, $\boldsymbol{\langle r^2_{i(t)} \rangle}$ are the characteristic values for the mean squared displacement and $\boldsymbol{\sigma^2}$ corresponds to the uncertainty of localization. To best describe the probability distribution data, it needs at least three exponential decay functions. Three types of mobile fractions (fast diffusion, slow diffusion and very slow diffusion) of resorufin molecules were thus observed in mesoporous nanocatalysts.

According to the Einstein-Smoluchowski equation for random diffusion in one dimension,[35] the diffusion coefficient can be directly calculated using the following equation.

$$\boldsymbol{\langle r^2_{i(t)} \rangle = 2D \cdot t}$$

Nevertheless, the result from data for single t_{lag} is usually insufficient to fully describe the molecular diffusion in a confined environment. One needs to consider the long-term observation. For molecules undergoes free diffusion, the $\langle r^2 \rangle$ increases as the t_{lag} grows. However, for those restricted molecules, $\langle r^2 \rangle$ that is still well approximated in the same way is stationary at different t_{lag}. Therefore, the diffusion coefficient is better estimated by fitting the $\langle r^2 \rangle$ versus t_{lag} giving of three diffusion coefficients of 0.022 ± 0.001 $\mu m^2/s$ (fast), 0.0068 ± 0.002 $\mu m^2/s$ (slow) and 0.0021 ± 0.0003 $\mu m^2/s$ (very slow). The large difference of diffusion coefficients indicates that the local environments in nanopores are very heterogeneous.

Motions of molecules in confined environment are usually expected to be restricted. To test the degree of restriction of resorufin molecules diffusion in nanopores, the diffusion coefficient at different lag time for all three mobile fractions were calculated as shown in Table 1. The time dependence of diffusion coefficient on lag time is fitted by the following equation.[36,37]

$$\boldsymbol{D = \frac{\Gamma}{4} t^{\alpha-1}}$$

Here Γ stands for the transportation coefficient, and α is the factor for quantifying the degree of restriction of molecular motions. For α = 1, it stands for molecules undergoing unrestricted motions, namely free Brownian diffusion, with a constant diffusion coefficient of D = Γ/4.

Acknowledgements

We thank Yuchen Pei and Dr. Chaoxian Xiao in Dr. Wenyu Huang's lab at Iowa State University for kindly providing the core-shell catalysts, TEM imaging and pore size distribution analysis from N2 adsorption-desorption isotherm experiments.

References:

1 Rust, M. J., Bates, M. & Zhuang, X. Sub-diffraction-limit imaging by stochastic optical reconstruction microscopy (STORM). *Nat. Meth.* 3, 793-796 (2006).

2 Betzig, E. *et al.* Imaging Intracellular Fluorescent Proteins at Nanometer Resolution. *Science* 313, 1642-1645 (2006).

3 Yildiz, A. *et al.* Myosin V Walks Hand-Over-Hand: Single Fluorophore Imaging with 1.5-nm Localization. *Science* 300, 2061-2065 (2003).

4 Yildiz, A. & Selvin, P. R. Fluorescence Imaging with One Nanometer Accuracy: Application to Molecular Motors. *Acc. Chem. Res.* 38, 574-582 (2005).

5 Roeffaers, M. B. J. *et al.* Spatially resolved observation of crystal-face-dependent catalysis by single turnover counting. *Nature* 439, 572-575 (2006).

6 De Cremer, G., Sels, B. F., De Vos, D. E., Hofkens, J. & Roeffaers, M. B. J. Fluorescence micro(spectro)scopy as a tool to study catalytic materials in action. *Chem. Soc. Rev.* 39, 4703-4717 (2010).

7 Chen, P. *et al.* Single-molecule fluorescence imaging of nanocatalytic processes. *Chem. Soc. Rev.* 39, 4560-4570 (2010).

8 Xu, W., Jain, P. K., Beberwyck, B. J. & Alivisatos, A. P. Probing Redox Photocatalysis of Trapped Electrons and Holes on Single Sb-doped Titania Nanorod Surfaces. *J. Am. Chem. Soc.* 134, 3946-3949 (2012).

9 Han, K. S., Liu, G., Zhou, X., Medina, R. E. & Chen, P. How Does a Single Pt Nanocatalyst Behave in Two Different Reactions? A Single-Molecule Study. *Nano Lett.* 12, 1253-1259 (2012).

10 Ha, J. W. *et al.* Super-Resolution Mapping of Photogenerated Electron and Hole Separation in Single Metal–Semiconductor Nanocatalysts. *J. Am. Chem. Soc.* 136, 1398-1408 (2014).

11 Tachikawa, T., Yonezawa, T. & Majima, T. Super-Resolution Mapping of Reactive Sites on Titania-Based Nanoparticles with Water-Soluble Fluorogenic Probes. *ACS Nano* 7, 263-275 (2012).

12 Roeffaers, M. B. J. *et al.* Super-Resolution Reactivity Mapping of Nanostructured Catalyst Particles. *Angew. Chem. Int. Edit.* 48, 9285-9289 (2009).

13 Blum, S. A. Location change method for imaging chemical reactivity and catalysis with single-molecule and -particle fluorescence microscopy. *Phys. Chem. Chem. Phys.* 16, 16333-16339 (2014).

14 Zhou, X., Choudhary, E., Andoy, N. M., Zou, N. & Chen, P. Scalable Parallel Screening of Catalyst Activity at the Single-Particle Level and Subdiffraction Resolution. *ACS Catalysis* 3, 1448-1453 (2013).

15 Xu, W. *et al.* Single-Molecule Electrocatalysis by Single-Walled Carbon Nanotubes. *Nano Lett.* 9, 3968-3973 (2009).

16 Andoy, N. M. *et al.* Single-Molecule Catalysis Mapping Quantifies Site-Specific Activity and Uncovers Radial Activity Gradient on Single 2D Nanocrystals. *J. Am. Chem. Soc.* 135, 1845-1852 (2013).

17 Kisley, L. *et al.* Unified superresolution experiments and stochastic theory provide mechanistic insight into protein ion-exchange adsorptive separations. *Proc. Natl. Acad. Sci. U. S. A.* 111, 2075-2080 (2014).

18 Lebold, T., Michaelis, J. & Brauchle, C. The complexity of mesoporous silica nanomaterials unravelled by single molecule microscopy. *Phys. Chem. Chem. Phys.* 13, 5017-5033 (2011).

19 Hellriegel, C. *et al.* Diffusion of Single Streptocyanine Molecules in the Nanoporous Network of Sol−Gel Glasses†. *J. Phys. Chem. B* 108, 14699-14709 (2004).

20 McCain, K. S., Hanley, D. C. & Harris, J. M. Single-Molecule Fluorescence Trajectories for Investigating Molecular Transport in Thin Silica Sol−Gel Films. *Anal. Chem.* 75, 4351-4359 (2003).

21 Christian, H., Johanna, K. & Christoph, B. Tracking of single molecules as a powerful method to characterize diffusivity of organic species in mesoporous materials. *New J. Phys.* 7, 23 (2005).

22 Cooper, J. T., Peterson, E. M. & Harris, J. M. Fluorescence Imaging of Single-Molecule Retention Trajectories in Reversed-Phase Chromatographic Particles. *Anal. Chem.* 85, 9363-9370 (2013).

23 Mabry, J. N., Skaug, M. J. & Schwartz, D. K. Single-Molecule Insights into Retention at a Reversed-Phase Chromatographic Interface. *Anal. Chem.* 86, 9451-9458 (2014).

24 Na, K., Choi, K. M., Yaghi, O. M. & Somorjai, G. A. Metal Nanocrystals Embedded in Single Nanocrystals of MOFs Give Unusual Selectivity as Heterogeneous Catalysts. *Nano Lett.* 14, 5979-5983 (2014).

25 Xiao, C. *et al.* High-Temperature-Stable and Regenerable Catalysts: Platinum Nanoparticles in Aligned Mesoporous Silica Wells. *ChemSusChem* 6, 1915-1922 (2013).

26 Xu, X. H. & Yeung, E. S. Direct measurement of single-molecule diffusion and photodecomposition in free solution. *Science* 275, 1106-1109 (1997).

27 Xu, X. H. N. & Yeung, E. S. Long-range electrostatic trapping of single-protein molecules at a liquid-solid interface. *Science* 281, 1650-1653 (1998).

28 He, Y., Li, H. W. & Yeung, E. S. Motion of single DNA molecules at a liquid-solid interface as revealed by variable-angle evanescent-field microscopy. *J. Phys. Chem. B* 109, 8820-8832 (2005).

29 Kang, S. H., Shortreed, M. R. & Yeung, E. S. Real-Time Dynamics of Single-DNA Molecules Undergoing Adsorption and Desorption at Liquid-Solid Interfaces. *Anal. Chem.* 73, 1091-1099 (2001).

30 Kang, S. H. & Yeung, E. S. Dynamics of single-protein molecules at a liquid/solid interface: Implications in capillary electrophoresis and chromatography. *Anal. Chem.* 74, 6334-6339 (2002).

31 Sun, W., Marchuk, K., Wang, G. F. & Fang, N. Autocalibrated Scanning-Angle Prism-Type Total Internal Reflection Fluorescence Microscopy for Nanometer-Precision Axial Position Determination. *Anal. Chem.* 82, 2441-2447 (2010).

32 Sun, W., Xu, A., Marchuk, K., Wang, G. & Fang, N. Whole-Cell Scan Using Automatic Variable-Angle and Variable-Illumination-Depth Pseudo-Total Internal Reflection Fluorescence Microscopy. *J. Lab. Autom.* 16, 255-262 (2011).

33 Barlow, R. J. Statistics, A Guide to the Use of Statistical Methods in the Physical Sciences. *John Wiley & Sons: Chichester* (1989).

34 Schilling, E. A., Kamholz, A. E. & Yager, P. Cell Lysis and Protein Extraction in a Microfluidic Device with Detection by a Fluorogenic Enzyme Assay. *Anal. Chem.* 74, 1798-1804 (2002).

35 Berg, H. C. Random Walks in Biology. *Princeton University Press: Princeton* (1993).

36 Feder, T. J., Brust-Mascher, I., Slattery, J. P., Baird, B. & Webb, W. W. Constrained diffusion or immobile fraction on cell surfaces: a new interpretation. *Biophys. J.* 70, 2767-2773 (1996).

37 Bouchaud, J.-P. & Georges, A. Anomalous diffusion in disordered media: Statistical mechanisms, models and physical applications. *Phys. Rep.* 195, 127-293 (1990).

38 Fang, X. L. *et al.* Hollow Mesoporous Aluminosilica Spheres with Perpendicular Pore Channels as Catalytic Nanoreactors. *ACS Nano* 6, 4434-4444 (2012).

39 Huang, Y. & Pemberton, J. E. Synthesis of uniform, spherical sub-100nm silica particles using a conceptual modification of the classic LaMer model. *Colloid Surface A* 360, 175-183 (2010).

40 Deng, Y. *et al.* Multifunctional Mesoporous Composite Microspheres with Well-Designed Nanostructure: A Highly Integrated Catalyst System. *J. Am. Chem. Soc.* 132, 8466-8473 (2010).

41 Thompson, R. E., Larson, D. R. & Webb, W. W. Precise Nanometer Localization Analysis for Individual Fluorescent Probes. *Biophys. J.* 82, 2775-2783 (2002).

Tables

Table 1. Mobility of single resorufin moelcules in nanopores.

t_{lag} (s)	Fast		Slow		Very slow	
	D_1 ($\mu m^2/s$)	c_1 (%)	D_1 ($\mu m^2/s$)	c_2 (%)	D_1 ($\mu m^2/s$)	c_3 (%)
0.05	0.022	34.17	0.0094	53.98	0.0042	11.85
0.1	0.023	11.49	0.0099	64.98	0.0033	23.53
0.2	0.022	0.3	0.0070	55.54	0.0029	44.16
0.4	0.021	0.05	0.0062	56.73	0.0021	43.22

Results of the analysis of the time-dependence frequency distributions of the step sizes as a function of lag time shown in Fig. 9. The analysis procedures was finished by first fitting the distributions with multicomponent exponential decay function assuming more than one mobile fractions present and diffusion coefficients were calculated at every lag time using Einstein-Smoluchowski equation.

Figures

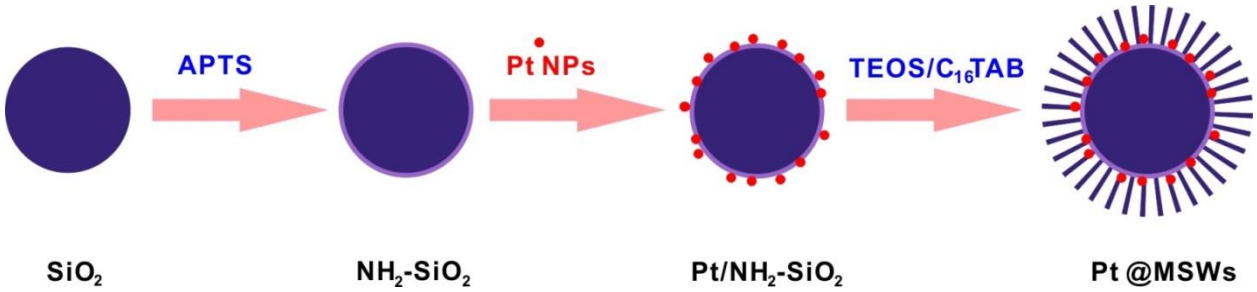

Figure 1. Synthesis of the core-shell nanocatalysts. The Pt NPs are sandwiched in between a solid SiO_2 core and a mesoporous SiO_2 shell with aligned channels. APTS: 3-minopropyltriethoxysilane; TEOS: tetraethyl orthosilicate; C_{16}TAB: hexadecyltrimethylammonium bromide.

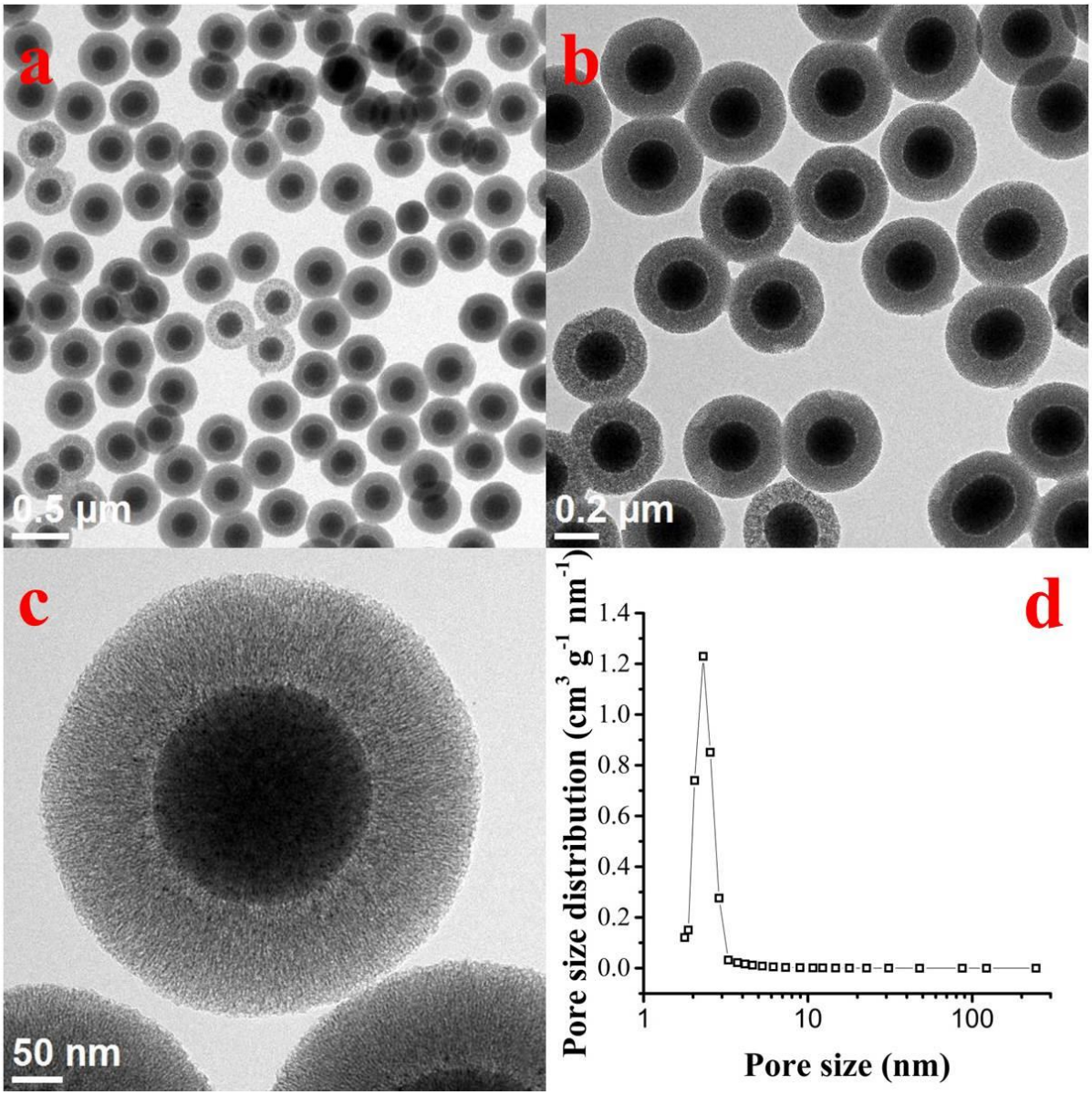

Figure 2. Characterize the structure of the core-shell nanocatalysts. (a) - (c) TEM images of 2.9 nm Pt NPs confined inside aligned mesoporous SiO_2 wells of 110 nm deep. The size of the SiO_2 core is 180 nm on average. Pt loading amount is ~ 2.5 wt%. (d) BJH-pore size distribution calculated from N2 adsorption-desorption experiments.

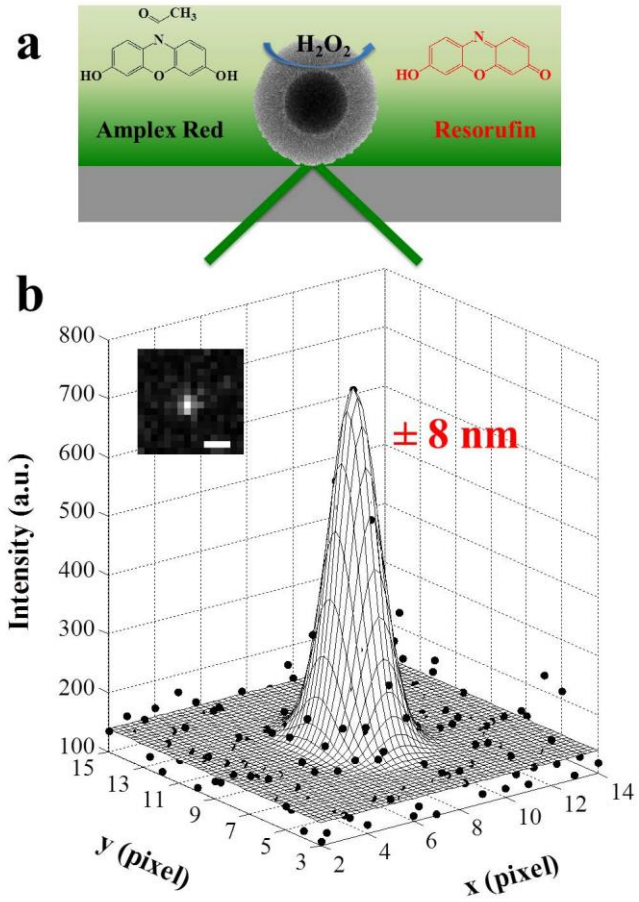

Figure 3. Localize the positions of single resorufin molecules from fluorogenic oxidation of amplex red. (a) Scheme shows the catalytic oxidation of non-fluorescent amplex red into highly fluorescent resorufin molecule by core-shell nanocatalysts with the present of hydrogen dioxide (H_2O_2). The fluorescence signal from produced resorufin molecules was captured by the imaging system. (b) A fluorescence image of a single resorufin molecule (inserted images) spreads over a few pixels as a point spread function (PSF). The center position of this PSF can be determined with an accuracy of a few nanometers by 2D Gaussian fitting of its fluorescence profile. In this specific example, the center position was determined with a precision of 8 nm. The localization precision varies depending on the fluorescence signal collected from each resorufin molecule. Scale bar: 1 μm.

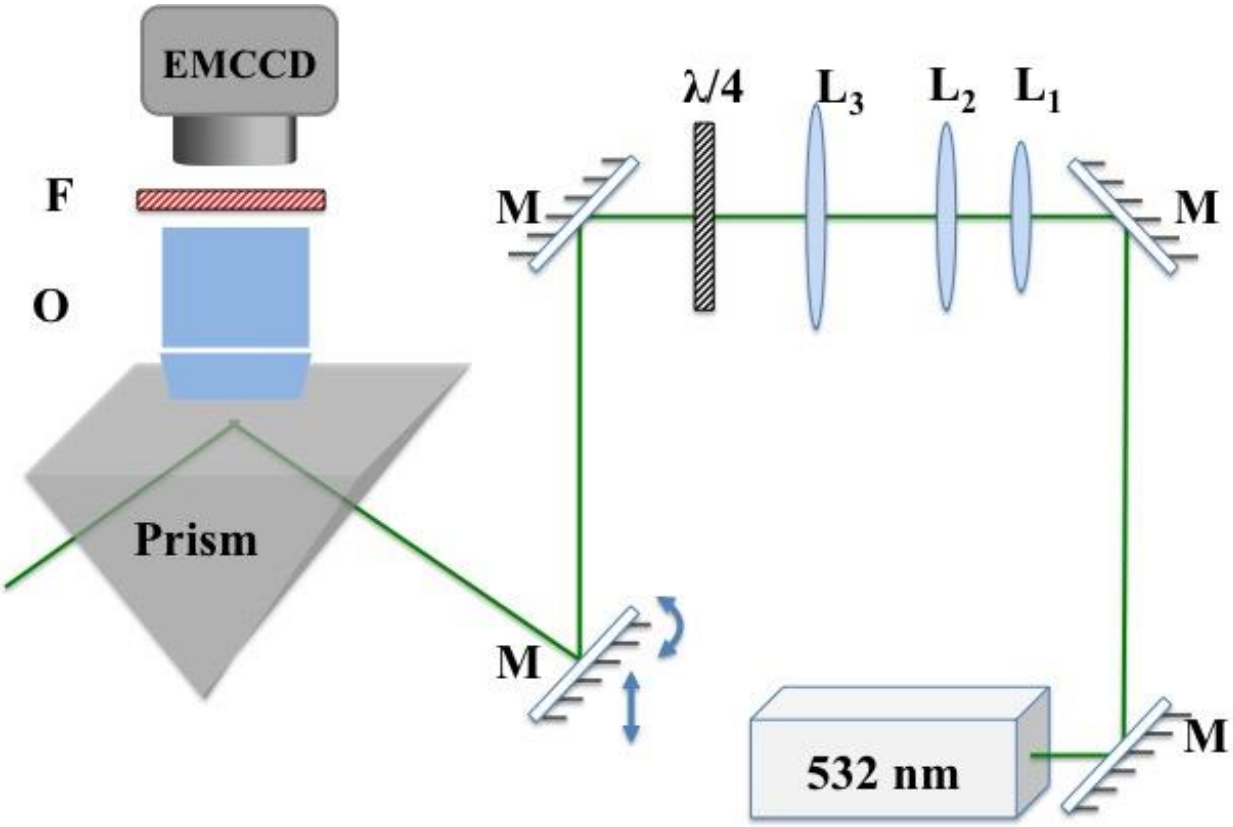

Figure 4. ***Automated*** **TIRFM.** (a) The optical setup of automated total internal reflection fluorescence microscopy. A CW 532 nm laser line was first collimated through a pair of lens L_1 and L_2. The laser beam was then directed through a equilateral prism encountering at the solid-liquid interface where TIR happened by a mirror galvanometer, which is also in conjunction with a motorized linear stage. In combination, the incident angle of incident laser beam and the location of illumination spot were able to adjusted to achieve optimal illumination conditions. A third lens (L_3) was inserted to control the size of illumination area. A quarter wave plate (λ/4) was insert into and out of the optical path to switch the laser beam between linear polarized and circular polarized. The fluorescent signal was collected by an oil immersion objective (O) and focused on the camera by a tube lens (L_4). The scattering background was rejected by a filter set (F).

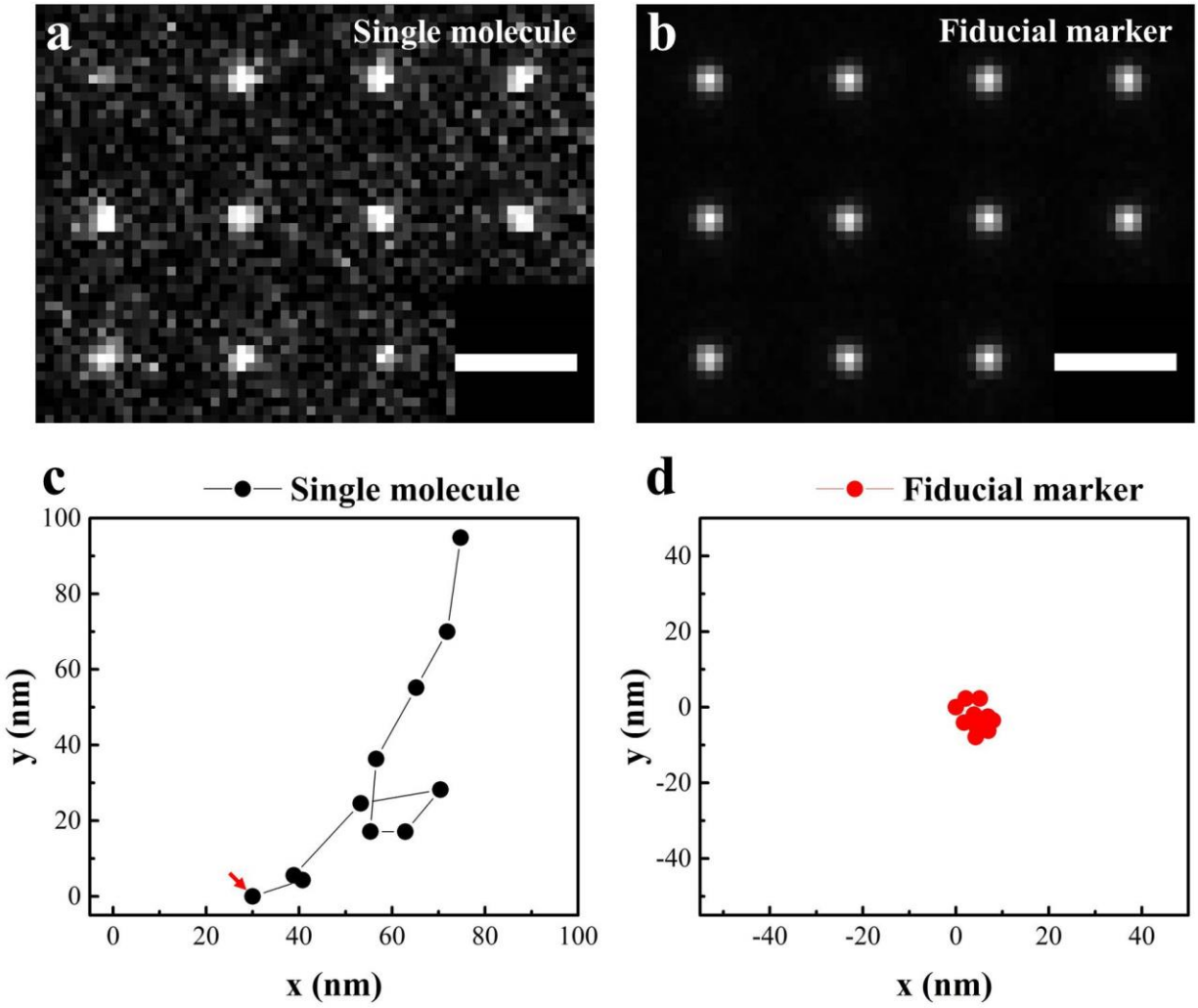

Figure 5. Single molecule imaging of chemical reaction and molecular transportations in confined environment. (a) A series of single images of fluorescent resorufin molecules generated from the catalytic reaction. (b) Images of a fluorescent bead (fiducial marker) at the same imaging time period as in (a). The localized positions of resorufin molecules and the fluorescent bead were plotted as trajectories as shown in (c) and (d) respectively. The location of catalytic reaction site was indicated by the red arrow in (c). Scale bar: 3 μm.

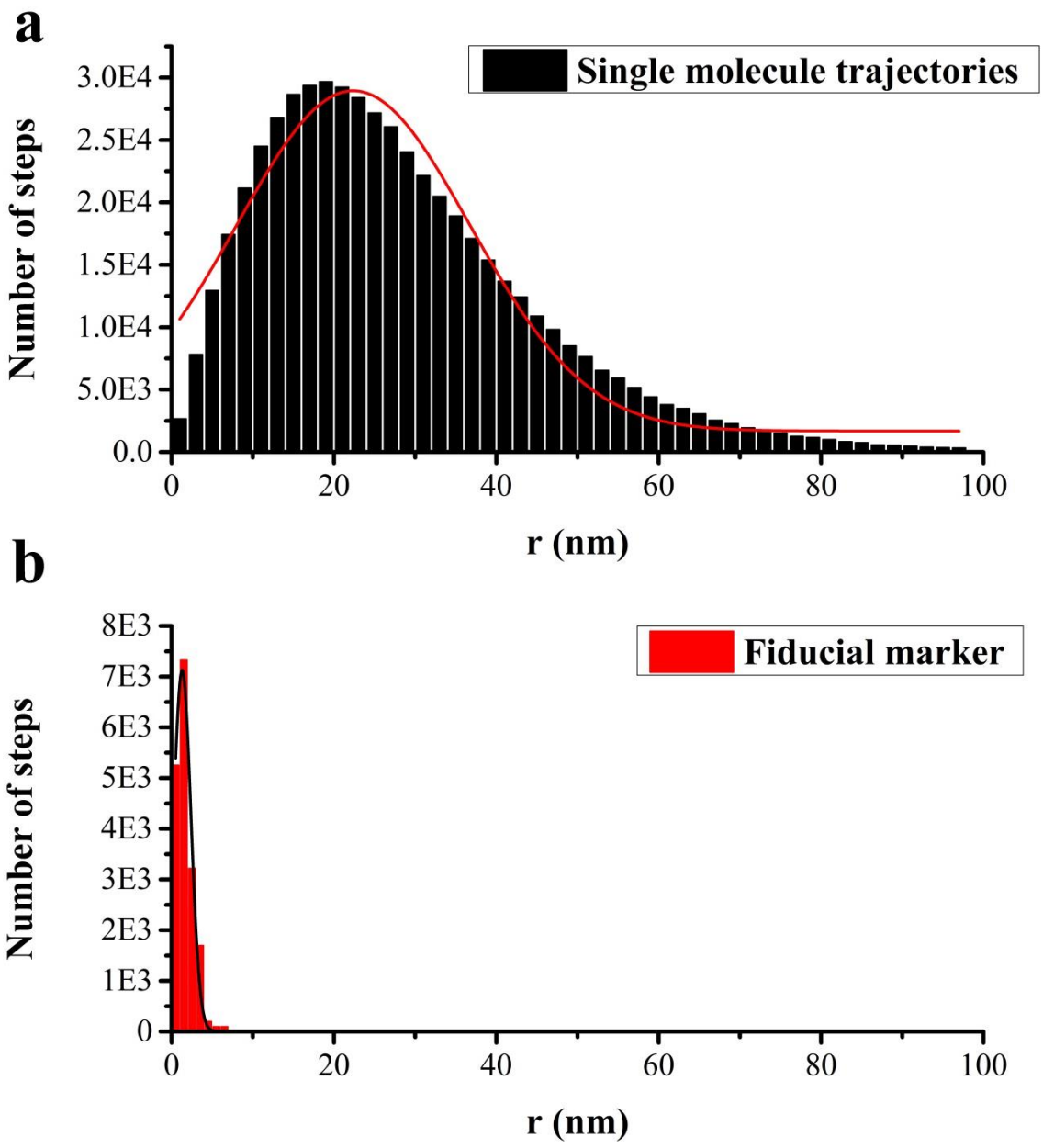

Figure 6. Displacement analysis of single molecular trajectories. (a) The histogram distribution of the step sizes at lag time of 0.05 s, which were calculated from over $\times 10^4$ single molecular trajectories. (b) The displacement of a fiducial marker during the imaging experiments was also analyzed in the same way. The positions of the fiducial marker were first corrected of stage drift by using another fiducial maker before the displacement analysis.

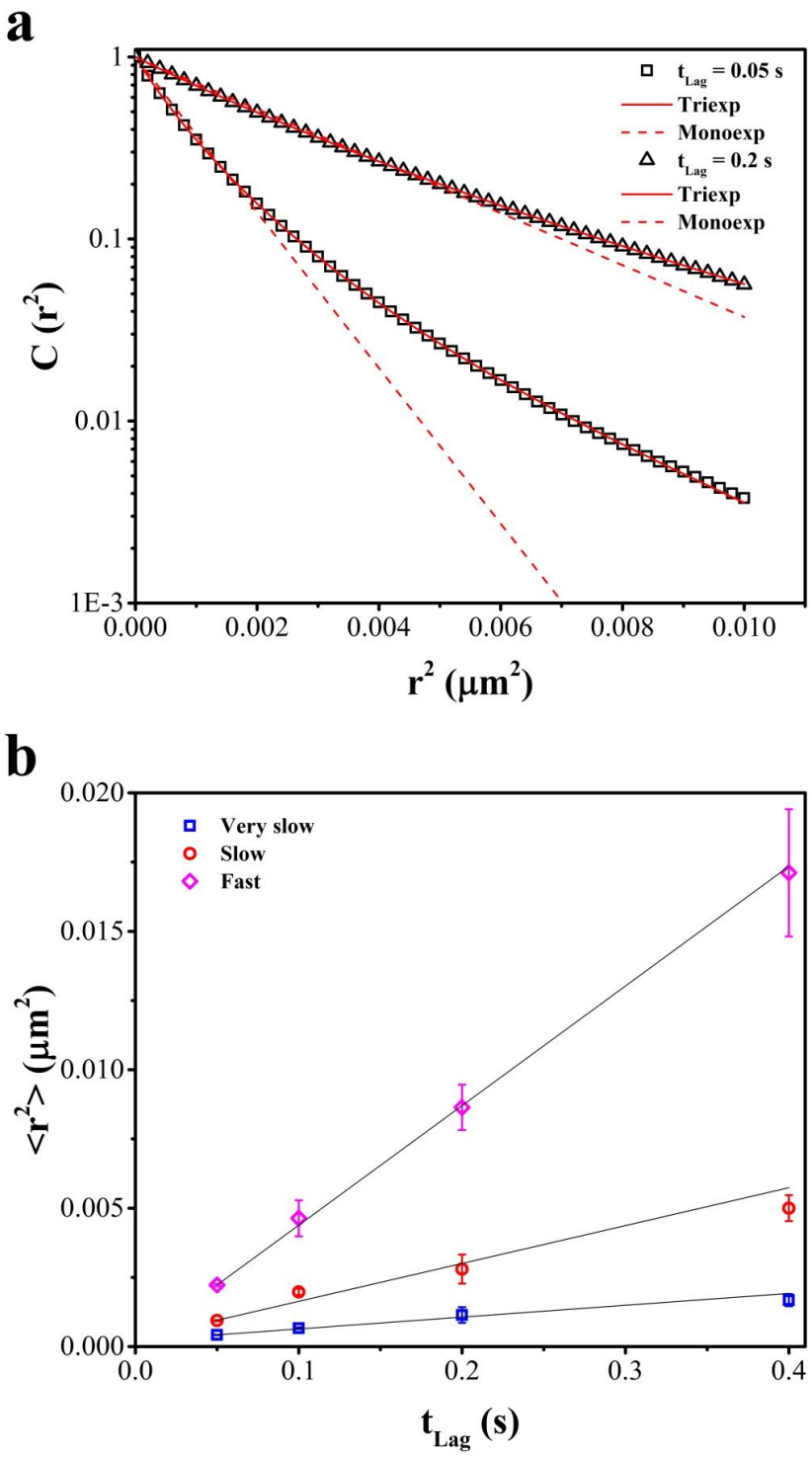

Figure 7. Quantify the mobility of resorufin molecules in nanopores. (a) The inverse cumulative probability distributions ($C(r^2)$) over the step sizes (r^2) at different lag time. The

results at two different lag time t_{lag} = 0.05 s (empty square) and t_{lag} = 0.2 s (empty triangle) were shown here. The probability distribution data were fitted by exponential decay functions with single component (red dash line) and multi-component (red solid line). (b) Mean squared displacement over lag time. Three sets of data from three different mobile fractions (Fast: magnet empty diamond, Slow: red empty circle, Very slow: blue empty square) were plotted and fitted with Einstein-Smoluchowski equation (See Materials and Methods).

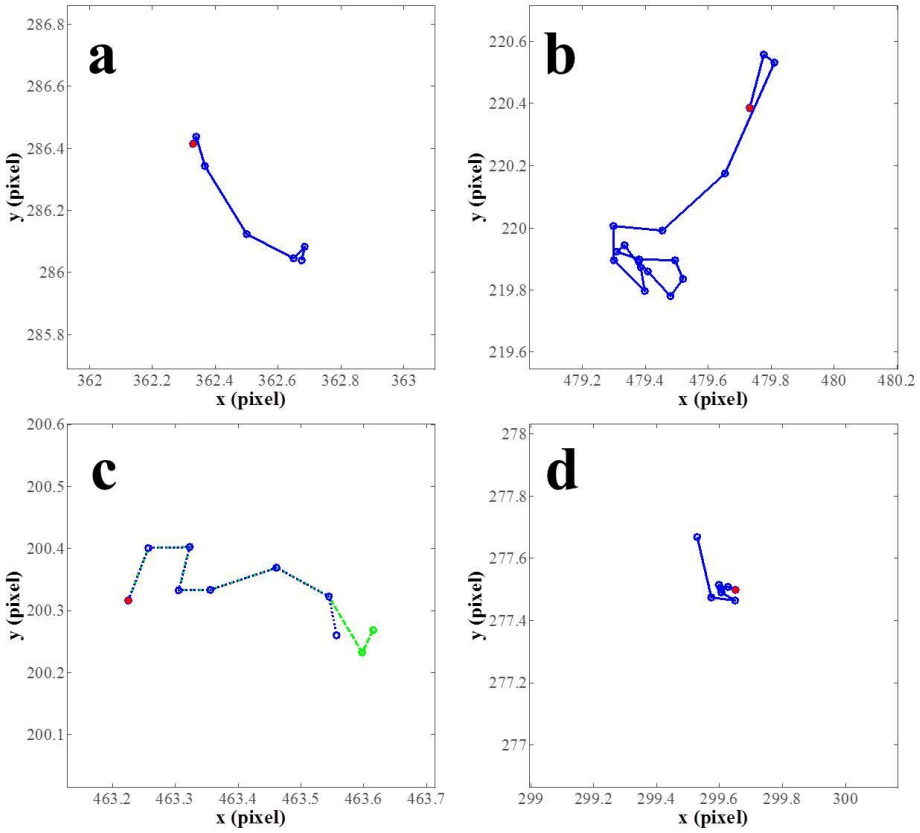

Figure 8. Single molecular trajectories of resorufin molecule diffusing in a nanopore. (a), (b) The resorufin molecule desorbed and diffusion in a nanopore quickly and was trapped in a short time period before it escaped away from the nanopore. (c) The resorufin molecule shows a relatively stable motion in this nanopore. (d) After staying at the catalytic reaction sites for a long time, the resorufin molecule quickly diffuse out the nanopore. The motions of resorufin molecules vary largely among different nanopores reflecting the heterogeneous pore structures of the core-shell nanocatalysts. It is worth to notice that the lengths of molecular trajectories were different due to the fact that the pores on a single nanocatalyst were aligned in all three dimensions. Therefore these trajectories are planar projections of one-dimensional diffusion trace of resorfion moelcules in three-dimensional space. The starting point of the single molecular trajectory was indicated as the red dot in figures.

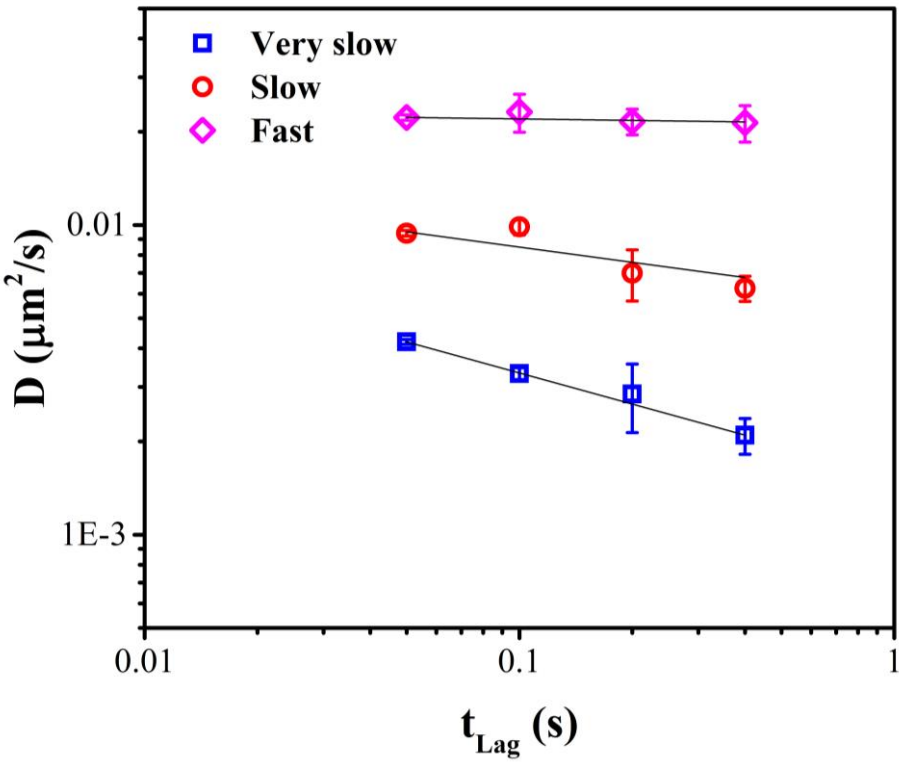

Figrue 9. Diffusion properties of resorufin molecule in a nanopore. The degree of restriction of molecular motion in a nanopore was quantified for all three different mobile components (Fast: magnet empty diamond, Slow: red empty circle, Very slow: blue empty square). The fast mobile component follows a free Brownian diffusion ($\alpha = 0.98 \pm 0.02$) behavior while the two slow mobile fractions undergo different amplitude of restrictions ($\alpha = .84 \pm 0.07$and $\alpha = 0.66 \pm 0.01$for slow and very slow diffusion components respectively).

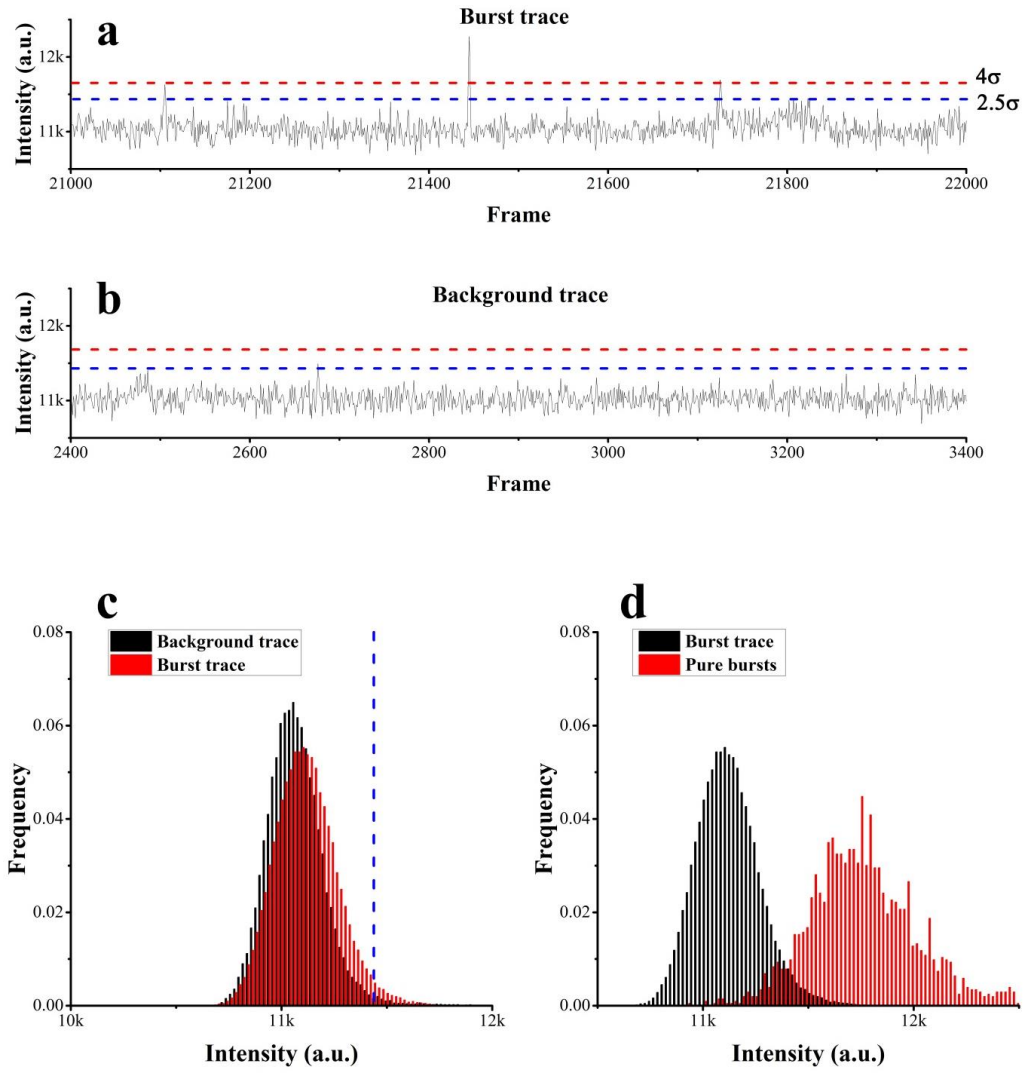

Figure 10. Criteria for identifying fluorescent bursts from the catalytic reaction. (a), (b) Part of the integrated fluorescence intensity traces from a imaging area of 10 pixels × 10 pixels of a core-shell nanocatalyst and nearby background. The blue and red dash lines correspond to the two intensity thresholds (Low: $I_{bg} + 2.5\sigma_{bg}$, High: $I_{bg} + 4.0\sigma_{bg}$) for filtering out the fluorescence bursts with 1% of uncertainty that the bursts are actually from background noise. (c) Histogram distributions of the integrated intensity from burst trace (red) and background trace (black). (d) Histogram distributions of the integrated intensity from identified bursts (red) and background trace (black).

CHAPTER 4: SINGLE PARTICLE ORIENTATION AND ROTATIONAL TRACKING IN REFLECTED LIGHT SHEET SCATTERING MICROSCOPY

Bin Dong, Ning Fang

A manuscript under peer review

Abstract

Rotational tracking with plasmonic gold nanorod probes has been shown to be a useful method to study rotational dynamics at sub-micrometer scale. In this chapter, a novel method, termed reflected light sheet scattering microscopy (RLSSM), was introduced for deciphering the three-dimensional orientation of gold nanorods with high angular resolution and localization accuracy. Two configurations of RLSSM were reported. In the dual-color RLSSM, two linearly polarized and well-collimated light sheets at the longitudinal and transverse surface plasmon resonance wavelengths were utilized to determine both in-plane and our-of-plane motions of gold nanorods. In the bifocal RLSSM, through pattern matching of the aberrant images of gold nanorods, the azimuthal angle of AuNR was resolved without suffering from the angular degeneracy. The detailed rotational dynamics of gold nanorods in glycerol/water mixtures was revealed at fast imaging rates of up to 500 frames per second. Furthermore, the imaging depth in RLSSM can be extended to hundreds of micrometers for imaging thick biological samples.

Introduction

Molecular motors are involved in many biological processes, such as DNA polymerization,[1] stepping of motor protein,Kural, et al. [2,3] and self-rotation of ATP synthase,[4] to perform critical functions at sub-micrometer scale. A full understanding of the detailed mechanisms of these processes often requires visualizing both translational and rotational motions induced by molecular motors. As an example of resolving translational motions, single particle tracking techniques with nanometer-scale localization precision have been used to reveal the hand-over-hand walking mechanism of microtubule-associated motor proteins.[2,5] On the other hand, fluorescence polarization spectroscopy[6-8] has been employed to decipher rotational motions of fluorescence dipole moments under polarized excitation. Traditionally, organic dye molecules or semiconductor quantum dots (QDs) are used as optical probes in these fluorescence anisotropy measurements; however, their applicability is significantly limited by the irreversible photobleaching of dye molecules and the intrinsic blinking of QDs.[9,10]

Plasmonic gold nanorods (AuNRs), which display excellent optical and chemical stability, have been intensely investigated as an alternative to fluorescent probes.[11-14] AuNRs possess several desirable features for single particle rotational tracking, including large scattering and absorption cross sections at the localized surface plasmon resonance (LSPR) wavelengths,[15-17] geometrically controlled anisotropic optical properties (the longitudinal and transverse LSPR modes along the long and shot axes of AuNRs, respectively), good biocompatibility, and controllable surface chemistry.[18-20]

Several techniques have been developed to resolve the orientation of AuNRs in the focal plane including dark-field (DF) polarization microscopy,[18] photothermal heterodyne imaging (PHI),[21] and differential interference contrast (DIC) microscopy.[22-26] These imaging methods use a similar strategy of separating light into two orthogonal polarization channels to decipher the azimuthal (in-plane) angle of either the long or short axis of an AuNR. However, the polar (out-of-plane) angle is either inaccessible (PHI) or ambiguous because of insufficient angular resolution (DF, DIC). Furthermore, the angular degeneracy resulting from the cylindrical shape of AuNRs limits these techniques' ability to differentiate the orientation of AuNRs in the four`1 quadrants of the Cartesian coordinate system. To circumvent the angular degeneracy, defocused orientation and position imaging (DOPI)[27,28] has been introduced to determine the three-dimensional (3D) orientation of a tilted single dipole in a single frame. The core idea is based on the electron transition dipole approximation and the fact that the dipole emission exhibits an angular anisotropy. Direct visualization of the spatial distribution of the scattered or emitted field of a single dipole becomes possible when an aberration, e.g., defocusing, is deliberately applied in the imaging system. Furthermore, a common practice of DOPI is to switch back and forth between the defocused and focused imaging modes to achieve more precise position and orientation determination.

Focused orientation and position imaging (FOPI) was recently demonstrated in the Fang Laboratory, which overcame the drawbacks of both polarization based in-focus imaging methods or the DOPI method.[23] The core idea is coupling the effects of the supporting dielectric substrate, such as a gold film, with the far-field scattering patterns of plasmonic nanoparticles. The in-focus imaging patterns are used to resolve the

absolute 3D orientation of tilted AuNRs near the substrate with high signal to noise ratio. Nevertheless, the necessary interaction between the AuNRs and the gold film limits its potential applications. A dual-color total internal reflection scattering (TIRS) imaging method[29] was also developed previously to dynamically resolve the azimuthal and elevation angles of AuNRs, thus allowing the characterization of their conformations on synthetic lipid membranes. Both of these methods, however, are more sensitive to a small range of elevation angles and more suitable for studying the rotational motions of AuNRs on substrate surfaces because of the short coupling distance in FOPI and the exponential decay of the evanescent field in TIRS.

To circumvent the limitations of the existing methods, herein, we report a novel single particle rotational tracking technique, reflected light sheet scattering microscopy (RLSSM), for deciphering the 3D orientation of AuNRs with high angular resolution and localization accuracy. The thickness of the excitation light sheet can be narrowed down to about half a micrometer to significantly reduce the excitation volume, and therefore the background is reduced effectively. Optical sectioning of the sample with large vertical scanning range (~200 μm) can also be achieved. Through modulating the scattering intensity fluctuation or matching the aberrant scattering patterns, we can track the orientation and rotational motions of nanoparticles in glycerol solution.

Results and Discussion

Characterization of light sheet profile

Reflected light sheet microscopy (RLSM) was originally reported by Gebhardt, *et al*.[30] An RLSM system consists of two objectives: one low-magnification water-immersion illumination objective (numerical aperture NA 0.8) and one high-

magnification oil-immersion detection objective (NA 1.3) with a vertical arrangement (Fig. 1). A light sheet with a thickness of several hundred nanometers to a few micrometers can be made by coupling the illumination objective at the focal plane of a cylindrical lens. A disposable atomic force microscopy (AFM) cantilever coated with gold functions as a tiny mirror to reflect the light sheet by 90° and projects a horizontal plane into the sample, thus allowing sub-micrometer optical sectioning.

The characterization of the laser beam profile is critical for the best utilization of the RLSM's unique features. The key parameters, as defined in Fig. 2a, are the minimum thickness (full width at half-maximum of cross-sectional intensity distribution) at the focal plane, the dimension (2 times the Rayleigh length), and the lateral extension (width). An important consideration is the tradeoff between the minimum thickness and the Raleigh length of the light sheet within which it remains reasonably uniform. The thickness of the light sheet can be varied by inserting an optical iris right behind the aperture of the illumination objective. The results show that the larger the iris opening is, the thinner the light sheet can be (Fig. 2b). With the NA 0.8 illumination objective and a laser light source at the wavelength (λ) of 660 nm, the Gaussian light sheet can be narrowed down to a minimum thickness of about 0.42 μm in the center and 0.59 μm at a distance of 0.64 μm (the Rayleigh length) from the center. Moreover, as shown in Fig. 2b, a smaller dimension of light sheet can be used with a smaller thickness. In the rest of experiments discussed here, a 4-mm aperture size was used to maintain a sub-micrometer light sheet thickness while achieving a relatively uniform illumination length of ~6 μm.

Comparison of epi-illumination and reflected light sheet illumination

Similar to total internal reflection fluorescence (TIRF) microscopy, in which a very thin evanescence field with a thickness of only a few hundred nanometers is employed to effectively eliminate the out-of-focus background, RLSM can also reduce the illumination thickness to the sub-micrometer range, thus providing us with an alternative way to greatly reduce the background. It is worthwhile to note that RLSM does not provide as good a background reduction as TIRF microscopy due to its larger illumination volume; however, RLSM does provide an important advantage over TIRF microscopy in its ability to image thick samples (up to several hundred micrometers) with the improved imaging depth.

Fluorescent beads were dispensed in 98% glycerol/water mixture and imaged in both epi-fluorescence microscopy and RLSM (Fig. 3). The shape of the light sheet could be visualized. Fluorescent beads clearly showed better signal to noise ratio (SNR) in RLSM than in epi-fluorescence microscopy. An improvement factor of 6 was calculated from over a hundred fluorescent beads: SNR = 43 ± 12, n = 115 for RLSM (Fig. 3d); SNR = 7 ± 3, n = 110 for epi-fluorescence (Fig. 3e). Variable SNRs are found along the light sheet path, and the best SNR is achieved at the thinnest part of the sheet.

Imaging AuNRs using dual-color RLSSM

The LSPR enhanced scattering of AuNRs depends on the wavelength and polarization of the excitation light, as well as the aspect ratio of the AuNRs. The longitudinal LSPR mode results in much stronger absorption and scattering signals than the transverse LSPR mode.[31,32] The UV-vis spectrum (Fig. 4a) of 40 nm × 97 nm AuNRs

(aspect ratio ~ 2.4, suspended in water) shows two peaks at the transverse (530 nm) and longitudinal (660 nm) LSPR wavelengths.

Two continuous-wave (CW) linearly polarized laser beams at the wavelengths of 532 nm and 660 nm were directed into the illumination objective and then reflected by the AFM tip to form a horizontal light sheet. Two Fresnel rhombs prisms (Fig. 1a) were used to control the polarization directions of both excitation light beams, which allowed us to modulate both excitation light sources between the s-polarization direction (s-pol, perpendicular to the plane of incidence) and the p-polarization direction (p-pol, in the plane of incidence). Fig. 4b shows the results with the 660-nm laser in p-pol and the 532-nm laser in s-pol. At either LSPR wavelength, the scattering intensity changes periodically as the corresponding axis of AuNR rotates with respect to the polarization direction of light.

The out-of-plane orientation changes (polar angles, θ) and the in-plane orientation changes (azimuthal angles, φ) of AuNRs can be tracked by using the p-pol 660-nm laser and the s-pol 532-nm laser, respectively. A dual channel system (Fig. 4c) has been set up to measure both angles simultaneously from the normalized scattering intensity. When the AuNR's long axis is parallel to the propagation direction of the 532-nm s-pol laser (φ=90°), the transverse SPR mode produces the most intense scattering. A $\sin^2\varphi$ fitting is used to calculate the remaining angles. Due to the nature of the squared sine fitting, the four-fold degeneracy remains in assigning the orientation angles. A similar approach is taken to assign polar angles. When the AuNR's long axis lies flat in the imaging plane (θ=90°), a minimum intensity is achieved under the 660-nm p-pol laser, while a vertical position (θ=0°) will result in the maximum LSPR excitation. A $\cos^2\theta$ fitting of the

normalized intensity calculates the rest of the angles. To most accurately assign the maximum and minimum intensities, each AuNR was recorded many thousands of frames.

Resolving both azimuthal and polar angles in dual-color RLSSM

To test the concept, the AuNRs (25 nm × 65 nm) were suspended in a mixture of glycerol (98%) and water (2%). High glycerol content results in a large viscosity, thus restricting both translational and rotational motions of AuNRs in this solution. AuNRs show very little lateral movement, but they can still rotate in 3D (Fig. 5a). The scattering intensity from AuNRs varies between a maximum and a minimum in the longitudinal LSPR channel. As a comparison, fluorescent beads in the same glycerol/water mixture show no significant fluctuations during the imaging time of 30 seconds (Fig. 5b).

Fig. 6a is the scatter plot of the positions of the AuNR from the trajectory shown in Fig. 5a. The lateral movement of this AuNR is confined within a narrow range of less than 500 nm. The apparent mean radical displacement of AuNR in this solution is 28.4 nm from fitting the probability density function of the distributions of calculated squared displacement from the same dynamic trace of AuNR (See Materials and Methods). This result is in agreement with the theoretical value of 31.1 nm under our current imaging frequency of 33 Hz according to the Tirado and Garcia dela Torre (TT) model.[33,34] Both theoretical and experimental data prove that the thickness of the light sheet in our setup is sufficiently large that the fluctuations of scattering intensity from AuNRs are not due to translational movement but rather free rotations.

To demonstrate the simultaneous tracking of longitudinal and transverse SPR modes, both lasers were set to s-pol. Since the long and short axes of AuNR are

orthogonally arranged, the signals in these two channels should be out of phase by 90^{o}, resulting in an anti-correlated relation between the two channels. As expected, Fig. 7a shows the nearly perfect anti-correlated traces (correlation coefficient: -0.85). Calculated angles (Fig. 7b) are also in good agreement.

Then we switched to a different configuration of 660-nm p-pol and 532-nm s-pol laser beams to image the same AuNRs and measure both azimuthal and polar angles (Fig. 7c). The correlation coefficient of -0.16 indicates that the anti-correlation was no longer the dominant relation between the two traces. The overall non-correlated relation suggests the existence of both in-plane and our-of-plane rotations.

Resolving azimuthal and polar angles without angular degeneracy in bifocal RLSSM

Though it is convenient to resolve both azimuthal and polar angles using dual-color RLSSM, one of its drawbacks as mentioned previously is the angular degeneracy originating from the symmetric shape of AuNRs. DOPI[27,35] provides a way to resolve the azimuthal angle of AuNRs in all four quadrants of the Cartesian coordinate system. However, its relatively slow imaging rate still limits its applicability in dynamic tracking of live events. To enable fast dynamic tracking of rotational motions without the limitation of angular degeneracy, a biplane imaging system has been implemented from slight modification of dual-color RLSSM system (Fig.4d). In the biplane imaging system, the signal was split in 50:50 by a beam splitter. An extra lens was inserted into one of the optical paths thus shifting the focal plane in that channel.

In the channel where AuNRs are in-focus, we can precisely find their positions and calculate the polar angles with the 660-nm p-pol laser. Using the excitation light at the longitudinal LSPR wavelength helps to increase the localization precision. In the other channel, defocused image can be used to determine the azimuthal angle by matching the real images with the simulated data.

Previously, the azimuthal angle was determined by comparing the collected defocused image with simulated image manually. This often introduced large artificial uncertainties. Herein, we developed a MATLAB program to measure the azimuthal angle automatically based on calculating the correlation coefficient between the defocused image and the simulated images. An example is shown in Fig. 8. Two simulated images with the azimuthal angles of 50^{o} and 225^{o} were first generated using MATLAB codes. Their correlation coefficients with defocused images at different azimuthal angles were then calculated using the in-house programs. The results are shown as two traces with maximum correlation coefficients at 46° and 227°, respectively.

Because of the largely enhanced scattering intensity from plasmonic AuNRs, we can use high frame rates up to 500 Hz to image at the orientation and rotational behaviors of AuNRs in glycerol solution with sufficiently high SNR. Fig. 10 shows a trace of scattering intensity (red dot-line) from an AuNR in 98% glycerol/water mixture at an imaging rate of 2 ms/frame. The calculated polar angles and azimuthal angles were presented in Fig. 10 (green dot-line) and Fig. 11 (magnet dot-line), respectively. The AuNR would be expected to exhibit free rotations in all three dimensions thus giving a dynamic trace of angles that is fluctuating randomly between a maximum and a minimum (Fig. 5a). The measured rotational diffusion constants D_r were $0.0476 \pm 0.0004\ s^{-1}$ (out-

of-plane rotation) and 0.0211 ± 0.0006 s^{-1} (in-plane rotation) using auto-correlation analysis of the full dynamic trace of angles (Materials and Methods). These rotational diffusion coefficients are about two orders of magnitude smaller than the theoretical value[18] of 18.6 s^{-1}. The much smaller D_r from our experiments is consistent with the observation of frozen moments during the several observation periods (out-of-plane rotation: 10.0 s – 10.5 s and 14.5 s – 16.7 s; in-plane rotation: 20.6 s – 25.0 s and 26.0 s – 32.0 s in Fig. 10). When traces during 20 s – 60 s (polar angle) and 35 s – 60s (azimuthal angle) were used to run the auto-correlation analysis, giving of rotational diffusion coefficient D_r 17.7 ± 1.5 s^{-1} (out-of-plane rotation) and 22.3 ± 1.2 s^{-1} (in-plane rotation). These results indicated that the AuNR was undergoing free rotations during these observation times. The results show that the rotation of AuNRs in the glycerol/water mixture was not always completely free but with some restrictions occasionally.

Higher temporal resolution reveals more detailed rotational behaviors of AuNRs

There is a tradeoff between the accuracy in angle assignment and the imaging rate due to the fact that weaker signals are obtained at faster imaging rates. In addition, the imaging rate is also limited by the capability of the detector itself. To study the effects of imaging rates on the measured rotational diffusion constants, we reconstructed the tracking of AuNRs under the exposure times of 4 ms, 8 ms, 20 ms, 40 ms, and 100 ms (Fig. 12 – Fig. 16, respectively) through binning the 2-ms trace from the same AuNR. As the exposure time increases, the two slow rotation periods gradually disappear. As a result, the measured D_r increases (Fig. 9b, d). The loss of rotational information due to slower imaging rate is further demonstrated by studying the fast rotation periods. Fig. 10

is the result from auto-correlation analysis of the angle variations of the same AuNRs during the observation period from 20 s to 60 s (polar angle, Fig. 10a, b) and 35 s to 60 s (azimuthal angle, Fig. 10c, d). It clearly shows that the measured rotational diffusion constants decrease and deviate from the theoretical value as the imaging rate slows down. Therefore, more details including fast and slow rotational behaviors of AuNRs in glycerol/water mixture can be observed at faster imaging rates while they could be hidden at slower imaging rates.

Conclusions

In summary, we have presented a novel single particle orientation and rotational tracking method that combines the reflected light sheet illumination scheme with a dual-view detection system for tracking anisotropic plasmonic gold nanoparticles in 3D. Two approaches including dual-color RLSSM and bifocal RLSSM have been demonstrated to determine polar angles and azimuthal angles simultaneously. The LSPR enhanced absorption and scattering strength from plasmonic AuNRs and largely reduced background of thin excitation volume enabled us to push the imaging rate up to 500 fps. Unlike TIRF, the imaging depth in RLSSM can be extended to hundreds of micrometers. Therefore, we expect this method to become widely useful in biological studies in which 3D rotational motions are of great interest such as endocytosis and intracellular transportation in animal cells.

Materials and Methods

Optical setup

A 50-mW 532-nm CW laser (Uniphase, San Jose, CA) and a 200-mW 660-nm CW laser (Laser Quantum, UK) were collimated into the same optical pathway with dichroitic mirrors. The beams were then expanded by a telescope of a pair of cylindrical lens and then directed into the illumination objective. The tipless AFM cantilever coated with gold reflected the formed light sheet by 90° and projected it into a horizontally planar illumination beam. A half-wave Fresnel rhomb (FR600HM, Thorlabs, Newton, NJ) was placed into the beam path for switching between s-pol and p-pol illuminations. Scattered light is collected by a Plan Fluor 100x/NA 1.3 oil immersion objective and directed into a dual-view imaging system before reaching an Andor iXonEM+ 897 camera (Belfast, Northern Ireland; 512 × 512 imaging array, 16 μm × 16 μm pixel size). Within the dual-view system, a Stopline 532-nm notch filter (Semrock, Rochester, NY) was placed in the long pass path, and a Coherent 560-nm short pass (Coherent, Santa Clara, CA) was placed in the short pass path.

The configuration of bifocal RLSSM was similar to dual-color RLSSM. The collected scattering signal was split 50:50 with a beam splitter (BPD254S-FS, Thorlabs, Newton, NJ), and an additional long-focusing lens was inserted into one of the optical path to introduce a different focus depth in order to generate defocused images, which were used to determine the in-plane angle of AuNRs in 360°. One laser (660 nm, the longitudinal LSPR wavelength) was sufficient to obtain the 3D orientations of AuNRs in the bifocal imaging system.

Determination of the light sheet profile

According to the set of equations shown below, the minimum thickness when using a NA 0.8 illumination objective is 0.42 μm (λ = 660 nm) at the focal plane, giving the Rayleigh length of 0.64 μm. Therefore, a relatively uniform light sheet of 1.28 μm long is available. The dimension of a light sheet with reasonably even intensity can be as long as 28.33 μm if the minimum thickness increases to 2.00 μm.

$$\omega_0 = \frac{0.46\lambda}{\sqrt{M} \cdot NA^{0.91}} \; ; \; FWHM = \sqrt{2\ln(2)} \cdot \omega_0$$

$$z_r = \frac{\pi \cdot \omega_0^2}{\lambda} \; ; \quad \omega_0 = 1.27 \times f \cdot \lambda \cdot \frac{M^2}{D}$$

In these equations, ω_0 is $1/e^2$ radius of the laser spot, λ is the wavelength of light, $M^2 = 1$ for a perfect Gaussian beam, z_r is the Rayleigh length of light sheet, f is the focal length, D is the diameter of laser beam controlled by an optical iris.

The adjustment of the light sheet profile was realized by inserting an optical iris as an optical aperture behind the back focal plane of the illumination objective. The cross-sectional profiles of the light sheets at different opening sizes of the optical aperture were taken at different axial positions away from the focal plane of illumination objective. The thickness of the light sheet at every axial position was then determined as the FWHM from the Gaussian fitting of the cross-sectional profiles. It is worthwhile to note that reducing the optical aperture size also cuts off the laser beam and reduces the laser intensity at the focal plane and along the optical axis. All of these factors should be considered as a whole in the sample-dependent optimization process.

Sample Preparation

Fluorescent polystyrene beads (60 nm in diameter) were purchased from Duke Scientific (Palo Alto, CA), while AuNRs of two different sizes (25 nm × 65 nm, 40 nm × 97 nm) were purchased from Nanopartz (Salt Lake City, UT). The fluorescent bead solution was first dilute with 18.2-MΩ pure water to a proper concentration. 2 μL of the diluted solution were added into 998 μL of glycerol (Sigma-Aldrich). Then the glycerol solution containing the nanospheres was vortex and sonicated for 15 minutes.

The AuNRs colloid solutions were first centrifuged at room temperature and the supernatants were removed. Then the glycerol solutions of appropriate concentration were added into the AuNR pellet and then sonicated for 30 minutes. To uniformly suspend nanoparticles and fluorescent beads in the glycerol solution, the solution was mounted on a tube rotator for over 24 h.

Imaging AuNRs under RLSSM

The prepared glycerol solutions containing nanoparticles were first transferred into μ-Dish glass chamber (81158, ibidi). The chamber was then mounted on the sample holder. The reflected light sheet was inserted into the imaging system by adjust height of AFM tip holder. Further adjustments were necessary in order to make the horizontal light sheet close to the glass surface of the chamber. Once the adjustment was done, the sample was left on the microscope for 30 min to reduce the translational movement of nanoparticles caused by the operation.

An Andor iXonEM+ 897 camera was used to record full-frame images at 33 Hz. In order to achieving higher imaging speed, the region of image was cropped. The highest

frame rate with a reasonable size of imaging area we could manage with this camera was 500 Hz while the electron-multiplying (EM) gain was set to the maximum value of 300.

Determination of azimuthal and polar angles simultaneously

In dual-color RLSSM imaging, scattering intensity traces for both the longitudinal and transverse LSPR modes of single nanoparticles were generated using a MATLAB program. The calculation was based on summing the intensity of the 10 brightest pixels in the region of interest and then the summed intensity was subtracted by the background intensity.

The background intensity was determined by the following procedure. First, the average intensity of background was measured from a nearby 15 × 15 pixel area of the AuNRs. This area was carefully chose so that no signals from nanoparticles were included. Then the background intensity was taken as ten times of the average intensity. The background corrected intensity was then subtracted by the minimum intensity. The scattering intensity traces were further normalized using the resulting maximum intensity. $Cos^2\theta$ and $sin^2\varphi$ were used to perform the fitting of normalized intensity traces for the longitudinal and transverse LSPR channels, respectively. Thousands of frames were collected to ensure that all possible orientation angles were captured.

For bifocal RLSSM imaging, the polar angle was determined from the intensity trace of the in-focus channel following a similar procedure used for dual-color RLSSM. On the other hand, a MATLAB script was developed in-house to determine the azimuthal angles from the defocused images. A series of simulated defocused images from single dipoles were first generated using a programs published previously[27]. The angular

resolution in the simulated data pool was 1^{o} for both azimuthal and polar angles. The azimuthal angle was determined to be the case where simulated defocused image and collected defocused images generates the highest correlation coefficient. The Computer Vision System Toolbox package in MATLAB was used to calculate the correlation coefficient between two images. It should be noted that much weaker signals were acquired when the AuNR's long axis laid horizontally, leading to higher uncertainties in determining large polar angles.

Super-localization of AuNRs

The scattering intensity distributions from single AuNRs were fitted with 2D Gaussian functions, and the lateral positions (x, y) were extracted from the fitting results. The localization accuracy (σ) on average from the fitting results was calculated to be 3 nm based on the average collected photon number (N) of 6820 photons and the background noise (b) of 22 photons. It should be noted that the localization accuracy cannot be determined by 2D fitting of the distribution of locations from a cluster mainly because of the free translational movement (Fig. 6a) of nanoparticles in the solution.

Determination of the translational and rotational diffusion coefficients of AuNRs in solution

The probability distribution of the displacements as a function of different lag times (t_{lag}) was analyzed to understand the translational motions of nanoparticles in a homogenous medium such as the glycerol solution used in our experiments. The probability[36-39] that a nanoparticle from the origin will be found at time *t* within a shell of

radius r and thickness of *dr* is commonly defined as *p(r,t)dr*. For nanoparticles undergoing random-walk in solution, the probability density function *p(r,t)* is given by the following equation:

$$p(r,t) = \frac{1}{\pi < r^2 >} exp^{(\frac{-r^2}{<r^2>})} \cdot 2\pi r$$

$<r^2>$ is the mean squared displacement. Therefore, by fitting the distributions of displacements of nanoparticles at certain lag time (Fig. 6c), we can extract the mean square displacement $<r^2>$. According to the Einstein equation,[40] the mean square displacement $<r^2>=4D_t \cdot t_{lag}$ where D_t is the diffusion constant of nanoparticles in solution and t_{lag} is the delay time between observations for two-dimensional diffusion. To determine D_t more precisely, $<r^2>$ at different t_{lag} was calculated and a plot of the MSD versus time is shown in Fig. 6b. The data points follow a linear trend as predicted by the equation giving a diffusion coefficient D_t of $(6.7 \pm 0.3) \times 10^{-11}$ cm^2/s. The calculated D_t from our experiment data is in good agreement with the theoretical translational diffusion constant (5.4×10^{-11} cm^2/s) of 40 nm × 97 nm AuNRs based on the TT model.[33,34]

To determine the rotational diffusion constant of AuNRs in glycerol solution, we followed the same procedure as the previously published works.[18,25] Briefly, we first run autocorrelation analysis (ACA) on the calculated angles of AuNRs, the trend of autocorrelation coefficient versus time lag was then fitted by simple exponential decay function. The mean decay time $<\tau>$ for nanorods rotation can thus be determined from fitting results. $<\tau>$ of the decay reflects the rotation speed of AuNRs in the glycerol solution. With larger $<\tau>$, it means slower rotation. The rotational diffusion constant D_r was calculated based on $<\tau> = 1/6D_r$ as also reported from others' works.[18] The theoretical rotational diffusion constant was calculated using the following equation:[41]

$$D_r = \frac{3k_BT}{\pi\eta l^3}(ln^{\frac{2l}{d}} - 0.8),$$

where k_B is the Boltzmann constant, T is the absolute temperature, η is the viscosity of the glycerol/water mixture, l and d are the length of the long and short axes of AuNR, respectively.

References

1 Waga, S. & Stillman, B. THE DNA REPLICATION FORK IN EUKARYOTIC CELLS. *Annu. Rev. Biochem.* **67**, 721-751 (1998).

2 Kural, C. *et al.* Kinesin and Dynein Move a Peroxisome in Vivo: A Tug-of-War or Coordinated Movement? *Science* **308**, 1469-1472 (2005).

3 Forkey, J. N., Quinlan, M. E., Alexander Shaw, M., Corrie, J. E. T. & Goldman, Y. E. Three-dimensional structural dynamics of myosin V by single-molecule fluorescence polarization. *Nature* **422**, 399-404 (2003).

4 Yasuda, R., Noji, H., Yoshida, M., Kinosita, K. & Itoh, H. Resolution of distinct rotational substeps by submillisecond kinetic analysis of F1-ATPase. *Nature* **410**, 898-904 (2001).

5 Nan, X., Sims, P. A., Chen, P. & Xie, X. S. Observation of Individual Microtubule Motor Steps in Living Cells with Endocytosed Quantum Dots. *J. Phys. Chem. B* **109**, 24220-24224 (2005).

6 Forkey, J. N., Quinlan, M. E. & Goldman, Y. E. Protein structural dynamics by single-molecule fluorescence polarization. *Prog. Biophys. Mol. Biol.* **74**, 1-35 (2000).

7 Khatua, S. *et al.* Micrometer-Scale Translation and Monitoring of Individual Nanocars on Glass. *ACS Nano* **3**, 351-356 (2009).

8 Chung, I., Shimizu, K. T. & Bawendi, M. G. Room temperature measurements of the 3D orientation of single CdSe quantum dots using polarization microscopy. *Proc. Natl. Acad. Sci. U. S. A.* **100**, 405-408 (2003).

9 Moerner, W. E. & Orrit, M. Illuminating Single Molecules in Condensed Matter. *Science* **283**, 1670-1676 (1999).

10 Xie, X. S. & Dunn, R. C. Probing Single Molecule Dynamics. *Science* **265**, 361-364 (1994).

11 Wang, G., Stender, A. S., Sun, W. & Fang, N. Optical imaging of non-fluorescent nanoparticle probes in live cells. *Analyst* **135**, 215-221 (2010).

12 West, J. L. & Halas, N. J. Engineered Nanomaterials for Biophotonics Applications: Improving Sensing, Imaging, and Therapeutics. *Annu. Rev. Biomed. Eng.* **5**, 285-292 (2003).

13 Murphy, C. J. *et al.* Gold Nanoparticles in Biology: Beyond Toxicity to Cellular Imaging. *Acc. Chem. Res.* **41**, 1721-1730 (2008).

14 De, M., Ghosh, P. S. & Rotello, V. M. Applications of Nanoparticles in Biology. *Adv. Mater.* **20**, 4225-4241 (2008).

15 Kelly, K. L., Coronado, E., Zhao, L. L. & Schatz, G. C. The Optical Properties of Metal Nanoparticles: The Influence of Size, Shape, and Dielectric Environment. *J. Phys. Chem. B* **107**, 668-677 (2003).

16 Jain, P. K., Huang, X., El-Sayed, I. H. & El-Sayed, M. A. Noble Metals on the Nanoscale: Optical and Photothermal Properties and Some Applications in Imaging, Sensing, Biology, and Medicine. *Acc. Chem. Res.* **41**, 1578-1586 (2008).

17 Xiao, L., Wei, L., He, Y. & Yeung, E. S. Single Molecule Biosensing Using Color Coded Plasmon Resonant Metal Nanoparticles. *Anal. Chem.* **82**, 6308-6314 (2010).

18 Sönnichsen, C. & Alivisatos, A. P. Gold Nanorods as Novel Nonbleaching Plasmon-Based Orientation Sensors for Polarized Single-Particle Microscopy. *Nano Lett.* **5**, 301-304 (2005).

19 Sperling, R. A., Rivera Gil, P., Zhang, F., Zanella, M. & Parak, W. J. Biological applications of gold nanoparticles. *Chem. Soc. Rev.* **37**, 1896-1908 (2008).

20 Xiangyang, W. & Edwin, K. L. Y. Fluorescence blinking dynamics of silver nanoparticle and silver nanorod films. *Nanotechnology* **19**, 035706 (2008).

21 Chang, W.-S., Ha, J. W., Slaughter, L. S. & Link, S. Plasmonic nanorod absorbers as orientation sensors. *Proc. Natl. Acad. Sci. U. S. A.* **107**, 2781-2786 (2010).

22 Ha, J. W., Sun, W., Stender, A. S. & Fang, N. Dual-Wavelength Detection of Rotational Diffusion of Single Anisotropic Nanocarriers on Live Cell Membranes. *J. Phys. Chem. C* **116**, 2766-2771 (2012).

23 Ha, J. W., Marchuk, K. & Fang, N. Focused Orientation and Position Imaging (FOPI) of Single Anisotropic Plasmonic Nanoparticles by Total Internal Reflection Scattering Microscopy. *Nano Lett.* **12**, 4282-4288 (2012).

24 Wang, G., Sun, W., Luo, Y. & Fang, N. Resolving Rotational Motions of Nano-objects in Engineered Environments and Live Cells with Gold Nanorods and Differential Interference Contrast Microscopy. *J. Am. Chem. Soc.* **132**, 16417-16422 (2010).

25 Gu, Y., Sun, W., Wang, G. & Fang, N. Single Particle Orientation and Rotation Tracking Discloses Distinctive Rotational Dynamics of Drug Delivery Vectors on Live Cell Membranes. *J. Am. Chem. Soc.* **133**, 5720-5723 (2011).

26 Stender, A. S., Wang, G., Sun, W. & Fang, N. Influence of Gold Nanorod Geometry on Optical Response. *ACS Nano* **4**, 7667-7675 (2010).

27 Toprak, E. *et al.* Defocused orientation and position imaging (DOPI) of myosin V. *Proc. Natl. Acad. Sci. U. S. A.* **103**, 6495-6499 (2006).

28 Li, T. *et al.* Three-Dimensional Orientation Sensors by Defocused Imaging of Gold Nanorods through an Ordinary Wide-Field Microscope. *ACS Nano* **6**, 1268-1277 (2012).

29 Marchuk, K., Ha, J. W. & Fang, N. Three-Dimensional High-Resolution Rotational Tracking with Superlocalization Reveals Conformations of Surface-Bound Anisotropic Nanoparticles. *Nano Lett.* **13**, 1245-1250 (2013).

30 Gebhardt, J. C. M. *et al.* Single-molecule imaging of transcription factor binding to DNA in live mammalian cells. *Nat. Meth.* **10**, 421-426 (2013).

31 Sau, T. K. & Murphy, C. J. Seeded High Yield Synthesis of Short Au Nanorods in Aqueous Solution. *Langmuir* **20**, 6414-6420 (2004).

32 Sönnichsen, C. *et al.* Drastic Reduction of Plasmon Damping in Gold Nanorods. *Phys. Rev. Lett.* **88**, 077402 (2002).

33 Garcia de la Torre, J., Lopez Martinez, M. C. & Garcia Molina, J. J. Approximate methods for calculating rotational diffusion constants of rigid macromolecules. *Macromolecules* **20**, 661-666 (1987).

34 Tirado, M. M. & Garciadelatorre, J. Rotational-Dynamics of Rigid, Symmetric Top Macromolecules - Application to Circular-Cylinders. *J. Chem. Phys.* **73**, 1986-1993 (1980).

35 Toprak, E., Balci, H., Blehm, B. H. & Selvin, P. R. Three-Dimensional Particle Tracking via Bifocal Imaging. *Nano Lett.* **7**, 2043-2045 (2007).

36 Wilson, K. M., Morrison, I. E., Smith, P. R., Fernandez, N. & Cherry, R. J. Single particle tracking of cell-surface HLA-DR molecules using R-phycoerythrin labeled monoclonal antibodies and fluorescence digital imaging. *J. Cell Sci.* **109**, 2101-2109 (1996).

37 Anderson, C. M., Georgiou, G. N., Morrison, I. E., Stevenson, G. V. & Cherry, R. J. Tracking of cell surface receptors by fluorescence digital imaging microscopy using a charge-coupled device camera. Low-density lipoprotein and influenza virus receptor mobility at 4 degrees C. *J. Cell Sci.* **101**, 415-425 (1992).

38 Smith, P. R., Morrison, I. E. G., Wilson, K. M., Fernández, N. & Cherry, R. J. Anomalous Diffusion of Major Histocompatibility Complex Class I Molecules on HeLa Cells Determined by Single Particle Tracking. *Biophys. J.* **76**, 3331-3344 (1999).

39 McCain, K. S., Hanley, D. C. & Harris, J. M. Single-Molecule Fluorescence Trajectories for Investigating Molecular Transport in Thin Silica Sol−Gel Films. *Anal. Chem.* **75**, 4351-4359 (2003).

40 Michalet, X. & Berglund, A. J. Optimal diffusion coefficient estimation in single-particle tracking. *Phys. Rev. E* **85**, 061916 (2012).

41 Li, L.-s. & Alivisatos, A. P. Origin and Scaling of the Permanent Dipole Moment in CdSe Nanorods. *Phys. Rev. Lett.* **90**, 097402 (2003).

Figures

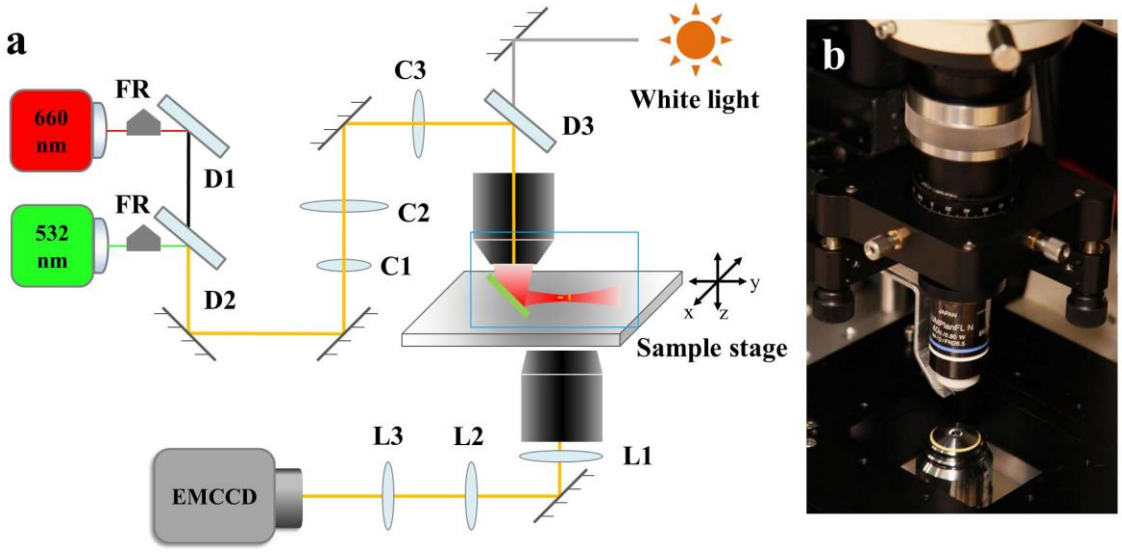

Figure 1. Imaging system for RLSSM. (a) Optical path showing the formation of reflected light sheet in RLSSM microscopy in which FR stands for half-wave Fresnel rhomb, D stands for dichroitic mirror, C stands for cylindrical lens and L stands for focus lens. A tiny mirror (i.e. a disposable tipless AFM cantilever coated with gold on both faces) reflects the light sheet by 90^{o} and projects a horizontal plane into the sample that is mounted on a high precision 3D-piezo stage, thus allowing sub-micrometer optical sectioning of the sample. White light source is conjugated into the optical path by using a dichroitic mirror (D_3). Before the collected signal gets the EMCCD camera, a pair of relay lens is used to adjust the magnification times. (b) A real picture showing the setup at sample stage.

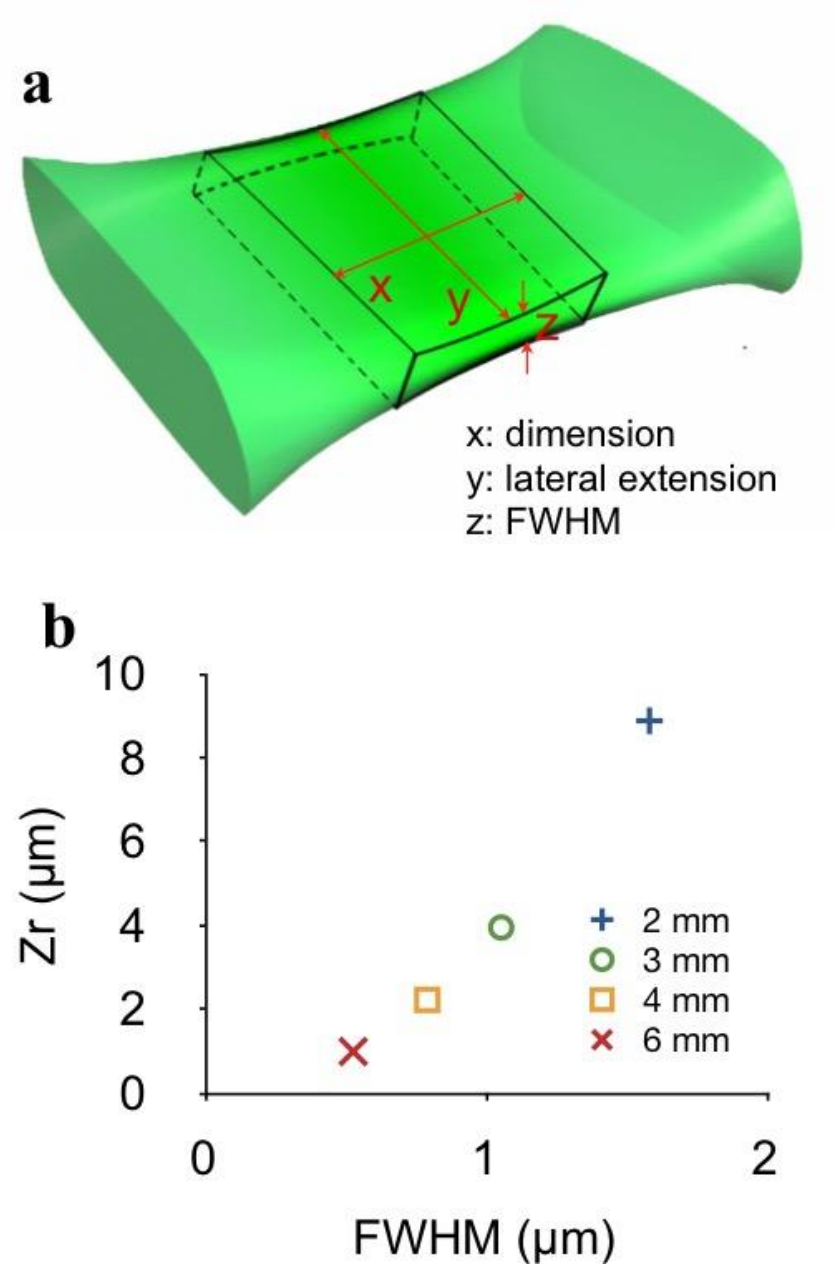

Figure 2. The light sheet profile can be readily adjusted with an iris behind the illumination objective. (a) 3D shape of a light sheet. *x* is the dimension which is 2 times of the Rayleigh length (Z_r); *y* is the lateral extension of the parallel light path; and *z* is the thickness of the light sheet at the focal plane which is determined by using FWHM of cross-sectional intensity distribution. (b) Correlation between the minimum thickness and the Rayleigh length under different optical aperture sizes of the iris.

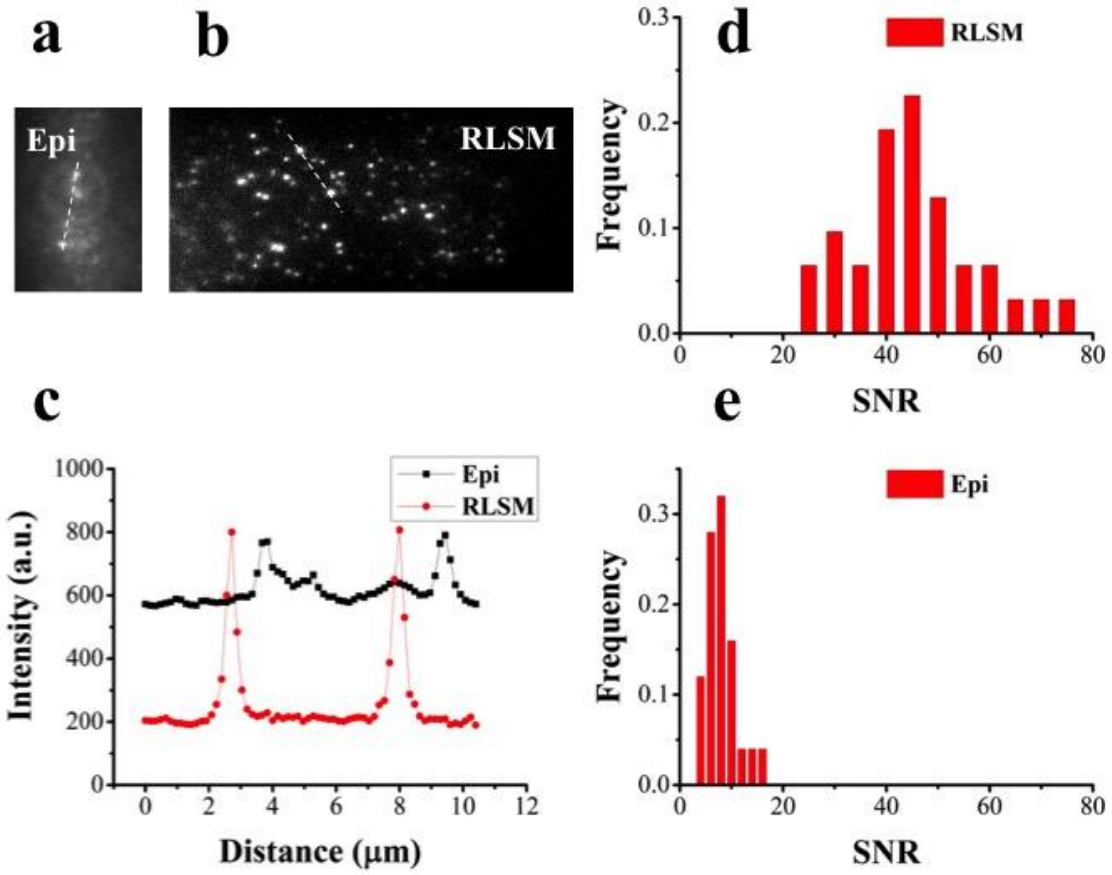

Figure 3. Schematics of illumination strategy for DC-RLSSM and bifocal RLSSM. (a) UV-vis spectrum of AuNRs with an average size of 40 nm × 97 nm in aqueous solution shows SSPR wavelength around 530 nm and LSPR wavelength around 660 nm. AuNRs with average size of 25 nm × 65 nm have same aspect ratio as 40 nm × 97 nm nanorods thus similar SSPR and LSPR wavelength should be expected. (b) The 660 nm (LSPR) laser was set to be p-polarized for determining the polar angle and the 532 nm (SSPR) laser was set to be s-polarized for determining the azimuthal angle in DC-RLSSM. The azimuthal angle and polar angle are defined as (φ) relative to the x axis (also the propagation direction of light) and (θ) relative to the z axis as shown in the Cartesian coordinate system. (c) Dual view system for DC-RLSSM in which collected scattering signal is separated into shortpass wavelength channel and longpass channel and

then focused by a focus lens to form image in the EMCCD camera. Image in each channel will occupy one half the full view field from the camera. (d) Dual view system for bifocal RLSSM where a beam splitter is used to split the collected signal 50:50 into two channels. One additional focus lens (L_2) is inserted into the optical path of one channel to introduce defocused image.

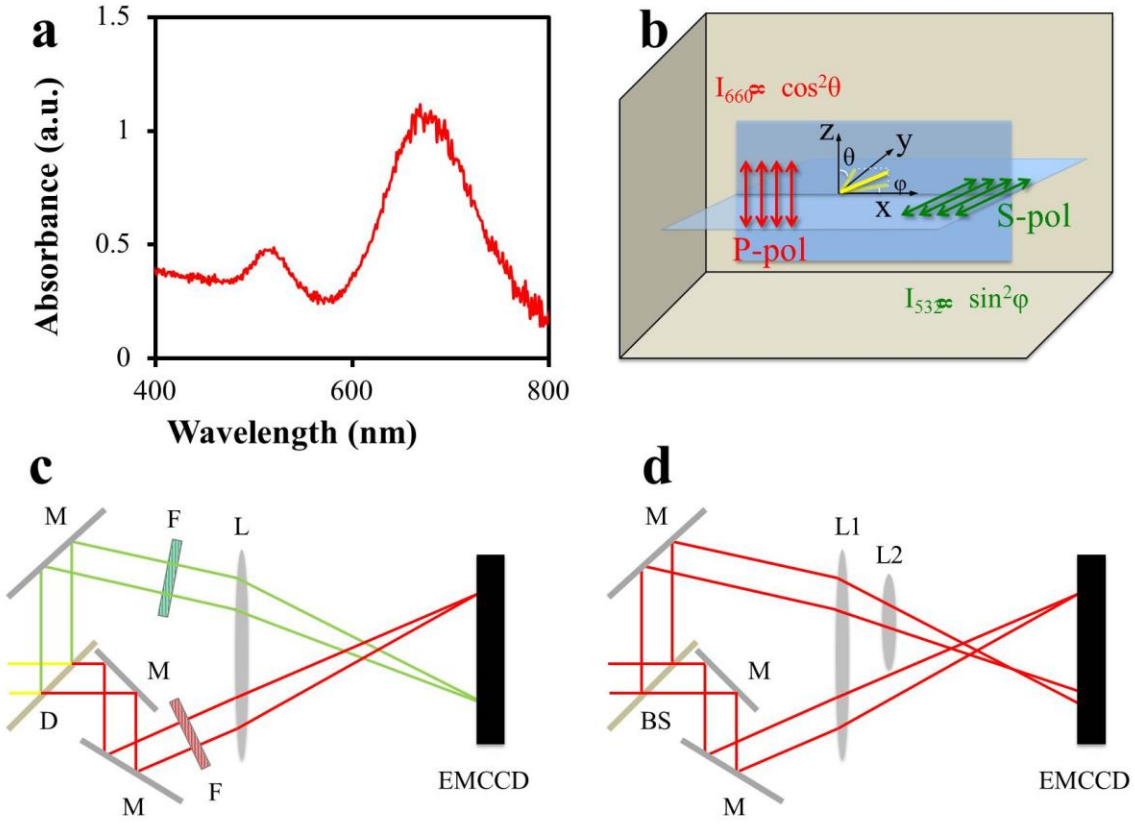

Figure 4. The confined illumination volume of light sheet reduces the background from out-of-focus significantly. (a) Epi-fluorescence image and (b) RLSSM image of 60 nm fluorescent beads in 98% glycerol/water mixture. The rectangular shape of reflected light sheet in the imaging plane is readily visible. (c) Cross-sectional profiles of the two beads from RLSSM image (red dot line) and epi-fluorescence image (black dot line) show the largely reduced background and noise in RLSSM imaging compared to epi-fluorescence imaging. (d) and (e) are histogram distributions of SNR over 115 and 110 fluorescent beads in RLSSM imaging and epi-fluorescence imaging respectively.

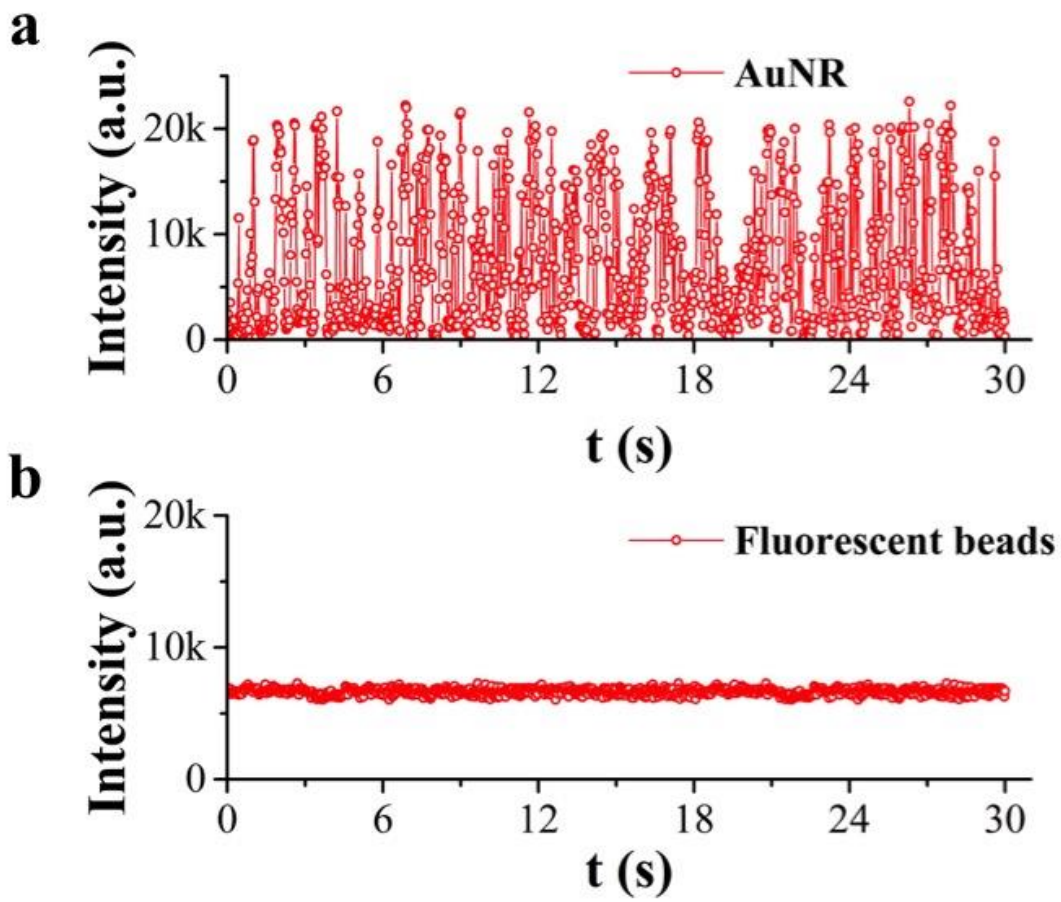

Figure 5. The dynamic intensity traces from nanoparticles and fluorescent beads show significant difference. (a) The scattering intensity from AuNR is blinking between a maximum and a minimum for long period of time, indicating free rotation of AuNR in glycerol solution. (b) On the contrary, no obvious change of fluorescent intensity from beads in same glycerol solution during the same amount observation time.

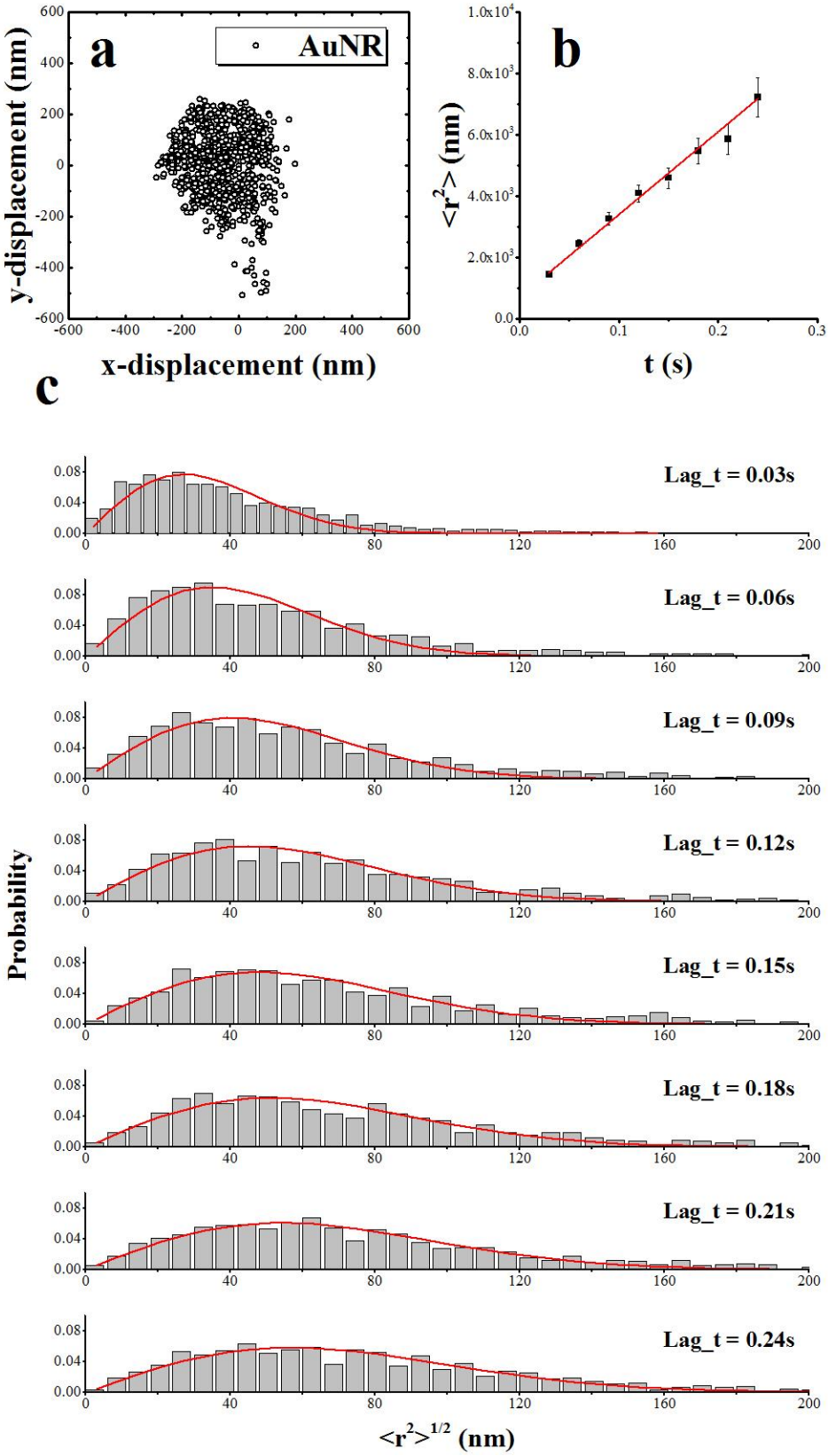
a
AuNR
y-displacement (nm)
x-displacement (nm)
b
<r^2> (nm)
t (s)
c
Lag_t = 0.03s
Lag_t = 0.06s
Lag_t = 0.09s
Lag_t = 0.12s
Lag_t = 0.15s
Lag_t = 0.18s
Lag_t = 0.21s
Lag_t = 0.24s
Probability
<r^2>^1/2 (nm)

Figure 6. The translational moving of AuNR in 98% glycerol solution is nearly frozen. (a) locations of same AuNR as shown in Fig. 5a. The translational diffusion of AuNR is confined within a very small region (400nm × 400nm). (b) The mean squared displacement of AuNR vs. lag time. The translational diffusion constant (D_t) from linear fitting of data points is $6.7 \pm 0.3 \times 10^{-11}$ cm^2/s which is in consistent with the theoretical value 5.4×10^{-11} cm^2/s. (c) Probability distributions of displacement (histogram) which are fitted by radical probability density function (red line) from a two dimensional random-walk model at different lag time (t_{lag}). Mean squared displacement can be extracted from the fitting results.

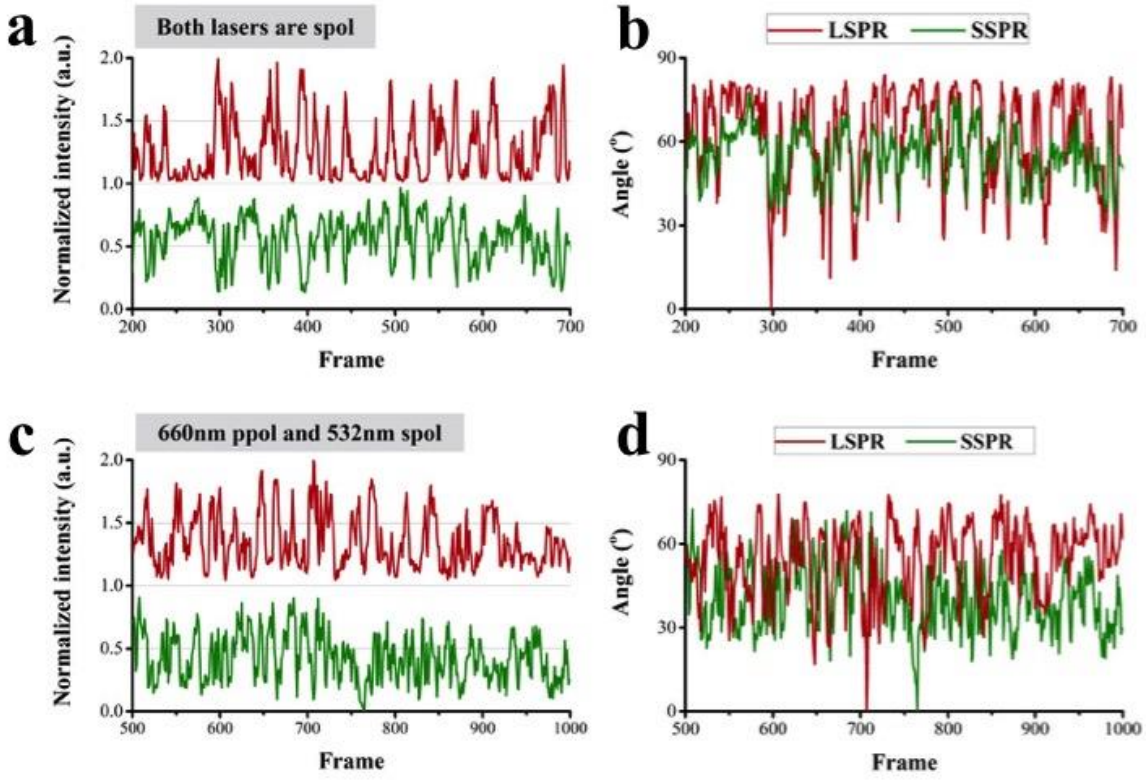

Figure 7. Determine the in-plane and out-of-plane angles of AuNRs in solution using DC-RLSSM. (a) An anti-correlated dynamic traces (anti-correlated coefficient: -0.85) of scattering intensity from 40 nm × 97 nm AuNR in 98% glycerol solution when the polarization of two illuminating laser lines at 532 nm and 660 nm are aligned perpendicular to the propagation direction of light. (b) Calculated angles from fitting the normalized scattering intensity traces showing a good agreement. (c) The normalized intensity traces and (d) calculated angles from the same particles but with 532 nm s-pol and 660 nm p-pol illumination shows decreasing correlations. The correlation coefficient is reduced -0.16 indicating a mix of anti-correlated, non-correlated and positive correlated relations between scattering intensity traces from two channels. Here, the azimuthal angles are plotted as green line while the red stands for the polar angles.

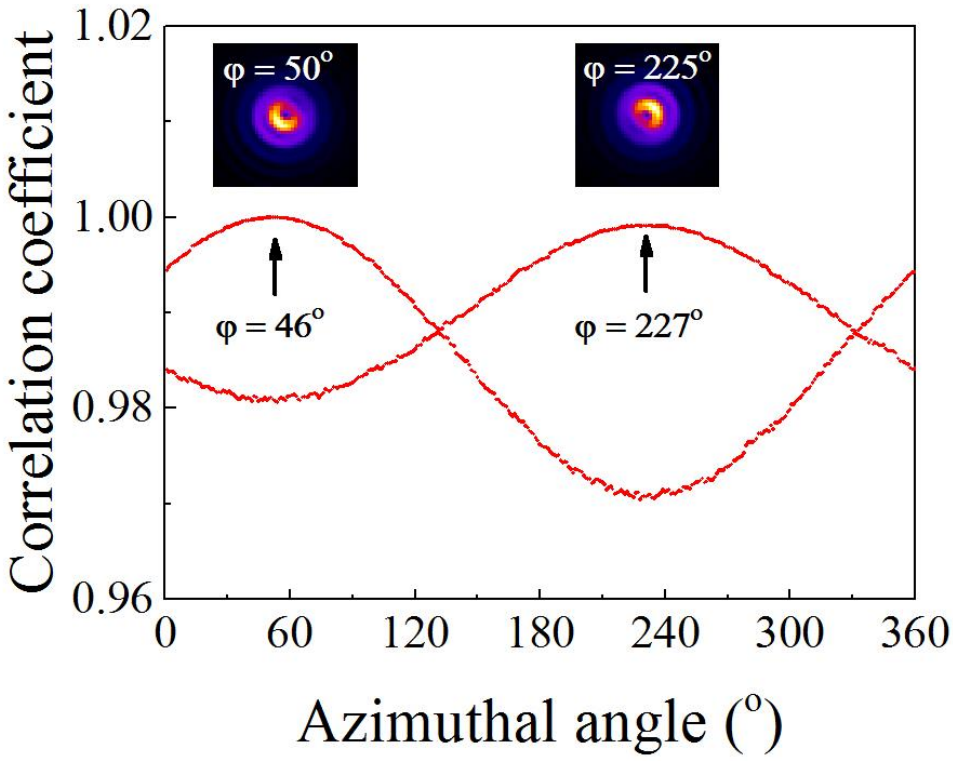

Figure 8. Determine the azimuthal angle of GNRs through pattern matching. The pattern matching process was based on calculating the correlation coefficient between target images and simulated images by using MATLAB codes. Two examples are shown here.

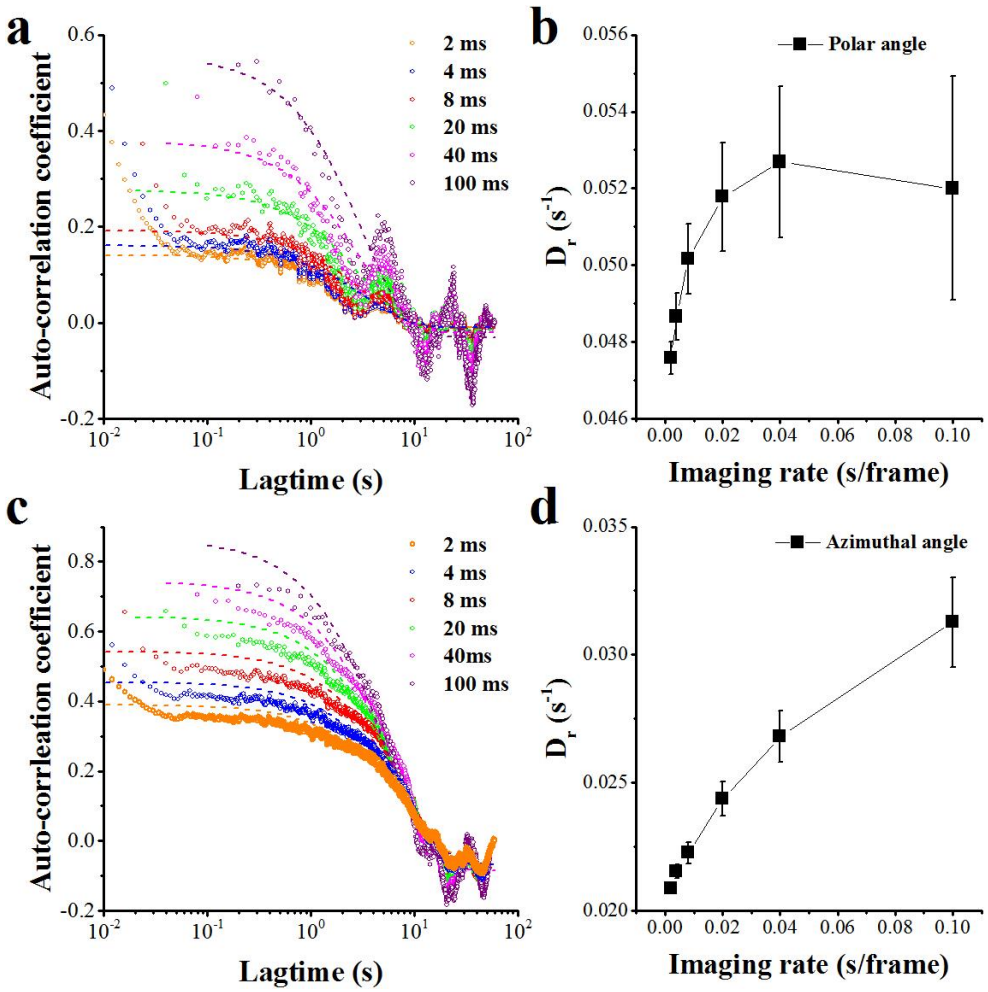

Figure 9. Determine the rotation speed of AuNRs in glycerol solution by auto-correlation analysis (ACA). (a) Results from performing ACA of the trace of polar angles of a AuNR under different frame rate. The full trace used for analysis was shown Fig. 11 (green dot-line) and Fig. 13 – Fig. 17 (green scatter-line) which was from a whole imaging period of 1.0 min. The scatter plots represented the auto-correlation coefficient versus the time lag. Dash lines were the fitting results from exponential decay function. (b) Plot showing the mean decay time D_r under different imaging speed. Larger D_r means faster rotation speed. (c) ACA of the trace of azimuthal angles and (d) plot of D_r versus imaging rate. The full trace of azimuthal angles was given in Fig. 12 – Fig. 17 (magnet dot-line).

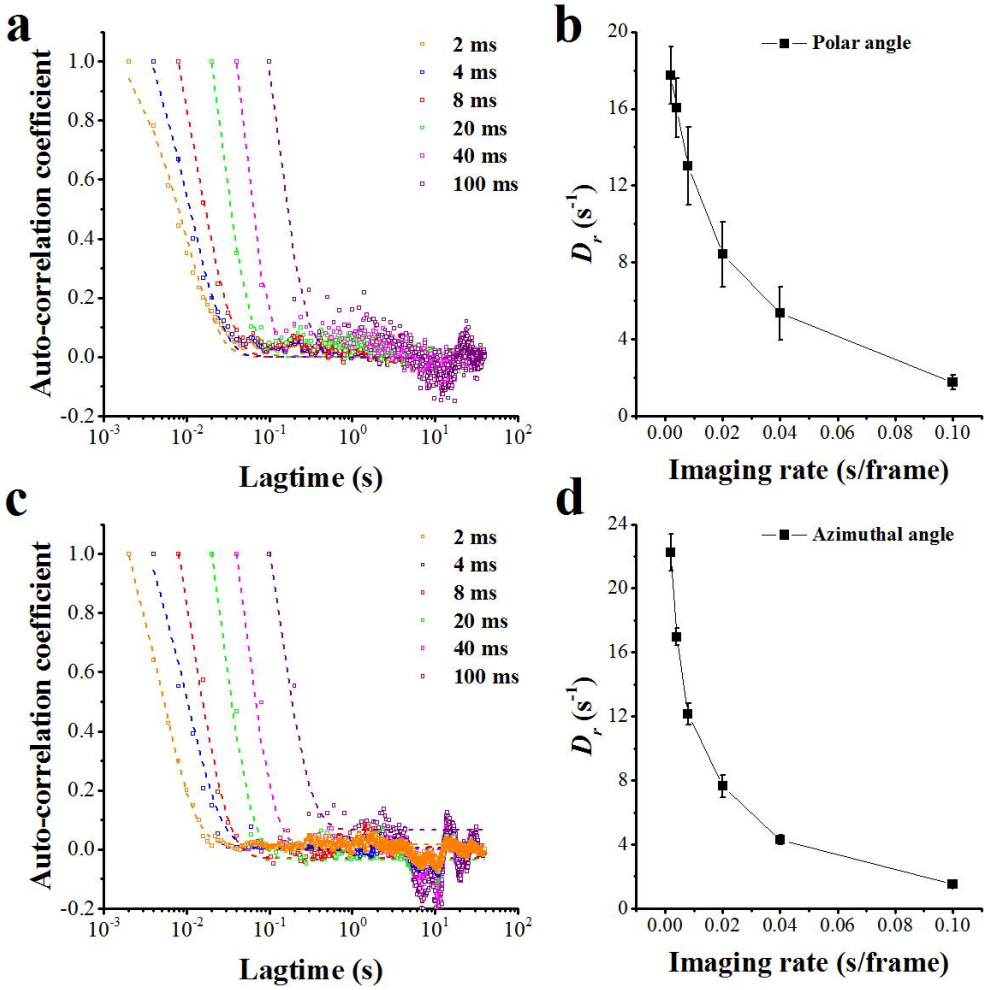

Figure 10. Effects of imaging rate on determining rotation speed of nanorods in glycerol solution. (a) Results from performing ACA of the trace of polar angles of the same AuNR as Fig. 9 between 20 s to 60 s under different frame rate. The scatter plots represented the auto-correlation coefficient versus the lagtime. Dash lines were the fitting results from exponential decay function. (b) Plot showing the rotational diffusion constant D_r under different imaging speed. (c) Auto-correlation analysis of the trace of azimuthal angles and (d) plot of D_r versus imaging speed during the same imaging period as in (a).

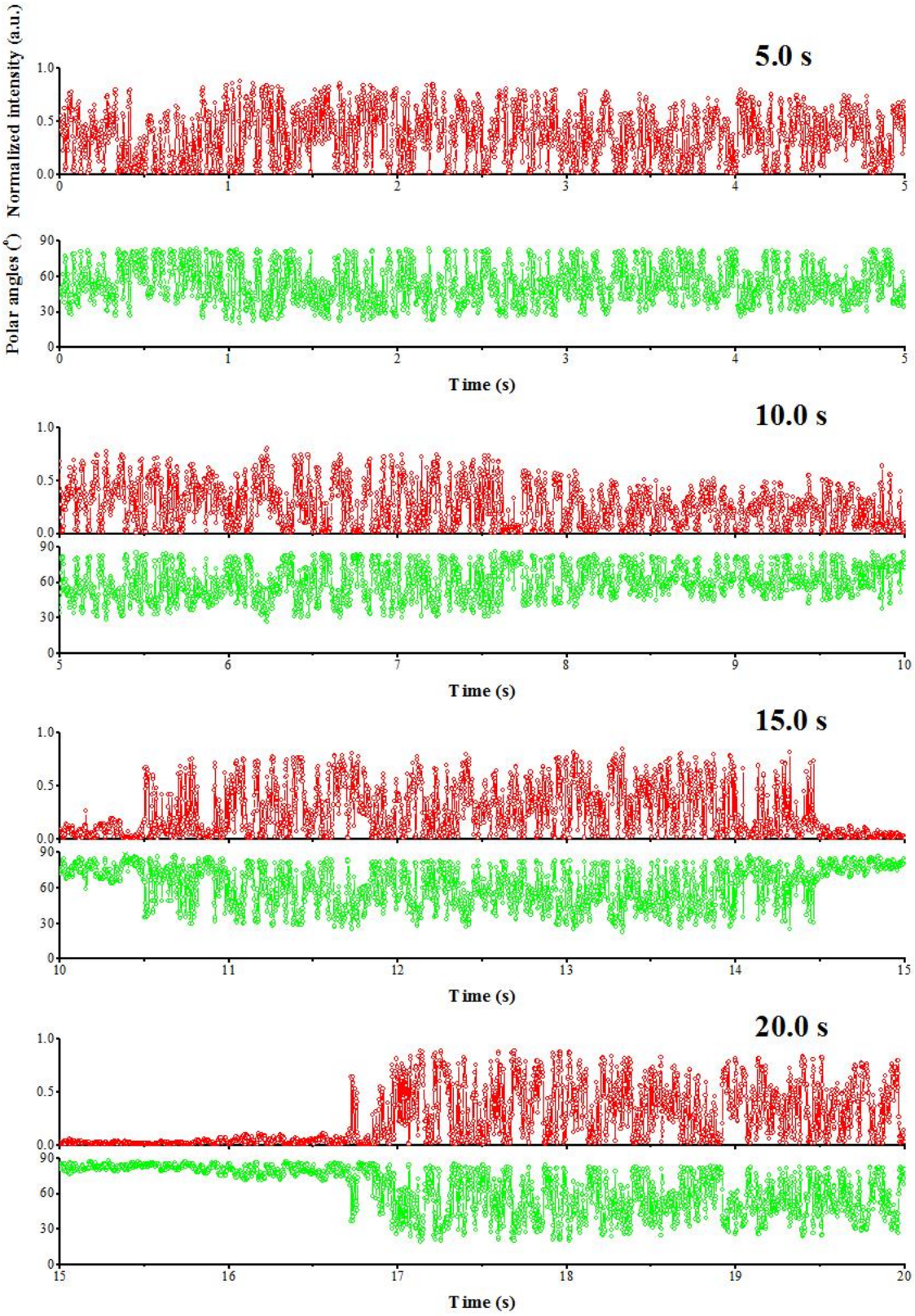
5.0 s
10.0 s
15.0 s
20.0 s
Normalized intensity (a.u.)
Polar angles (°)
Time (s)

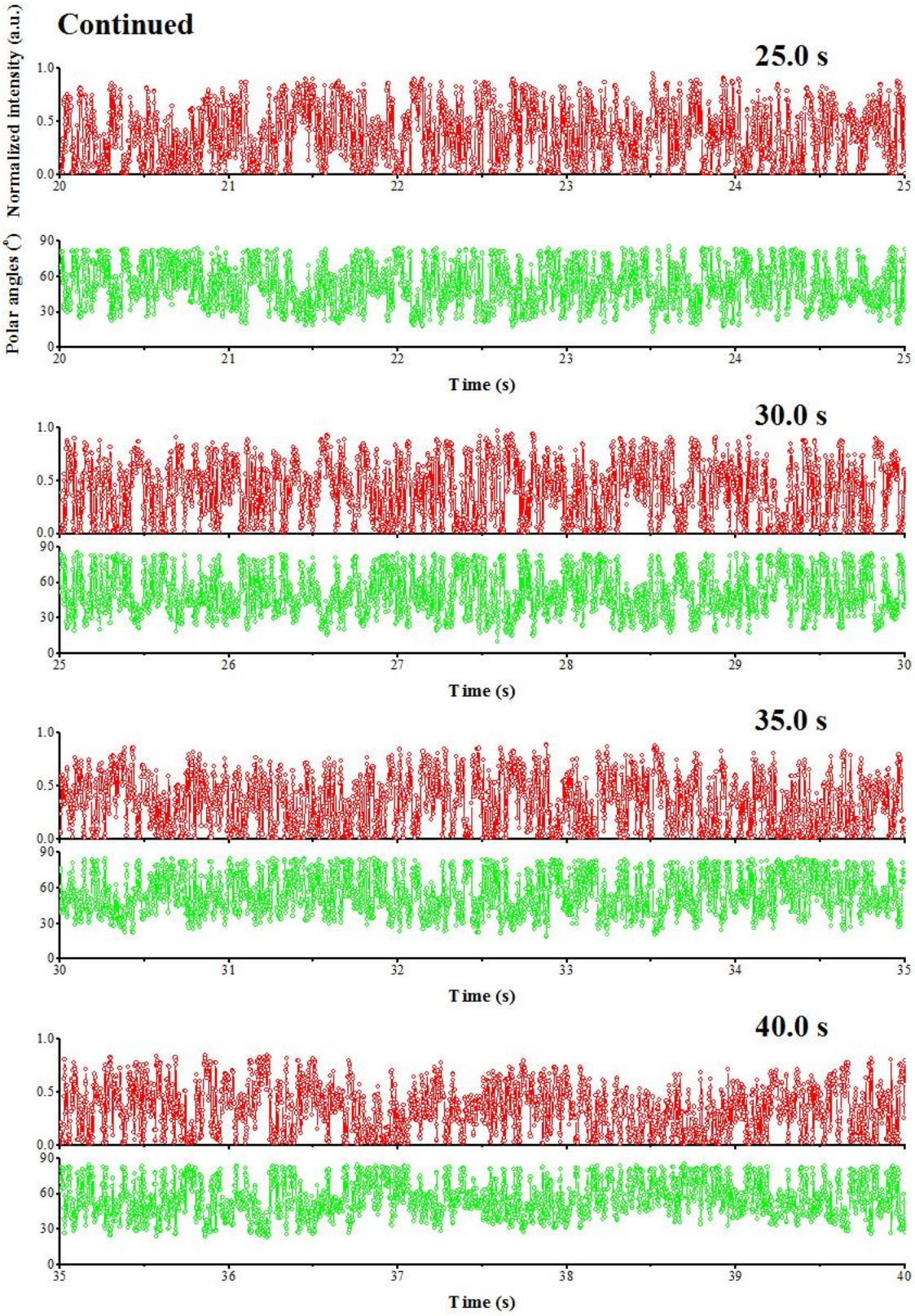
Continued
25.0 s
Normalized intensity (a.u.)
Polar angles (°)
Time (s)
30.0 s
Time (s)
35.0 s
Time (s)
40.0 s
Time (s)

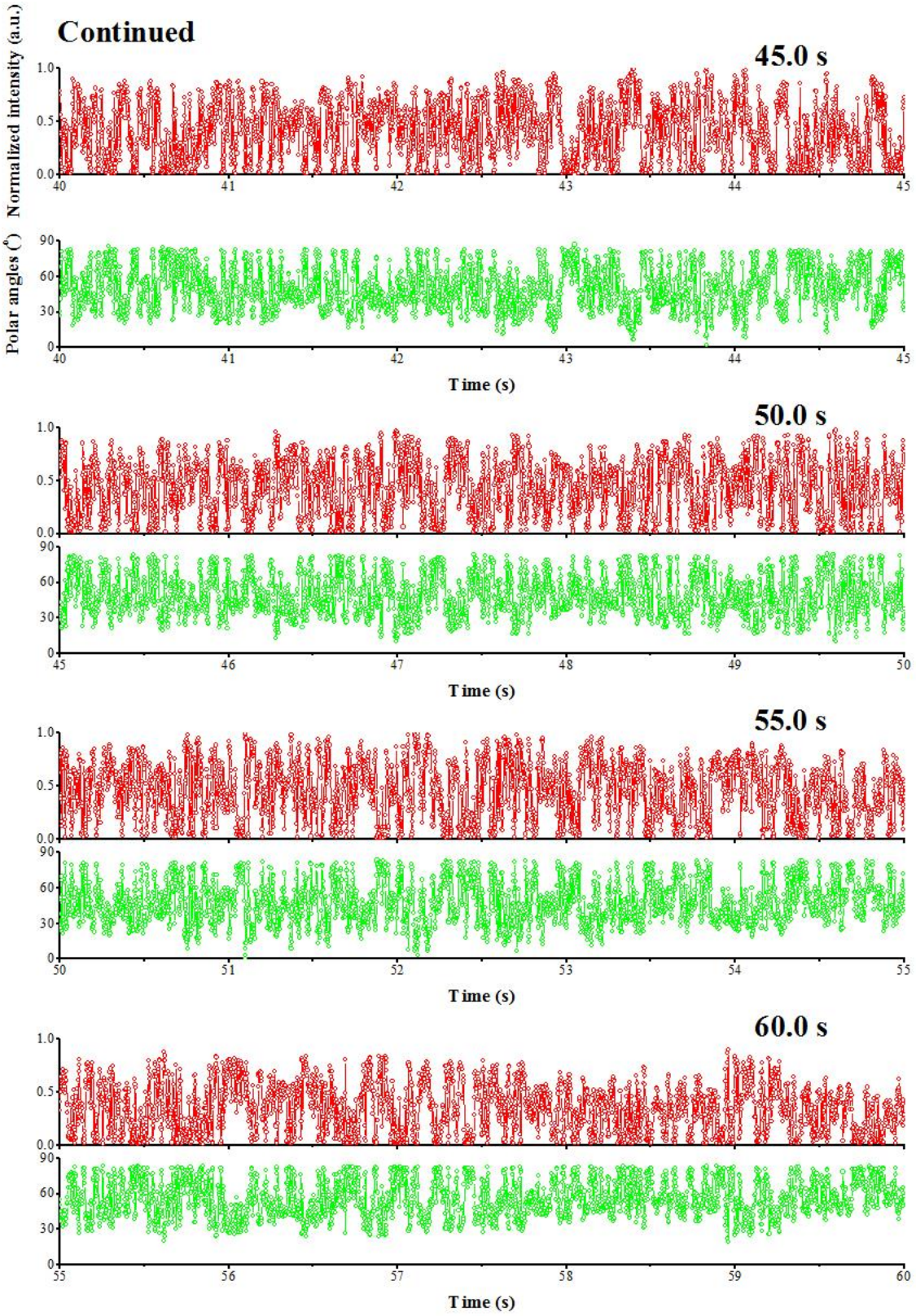
Continued
45.0 s
Normalized intensity (a.u.)
Polar angles (°)
Time (s)
50.0 s
Time (s)
55.0 s
Time (s)
60.0 s
Time (s)

Figure 11. Dynamic trace of normalized scattering intensity and polar angles from a AuNR in glycerol solution. Red dot-line plots were the dynamic trace of normalized intensity from AuNR scattering with temporal resolution of 2 ms. Green dot-line plots stands for the calculated polar angles. For better vision, the full trace was split into twelve segments and each segment was a dynamic trace of 5 s imaging.

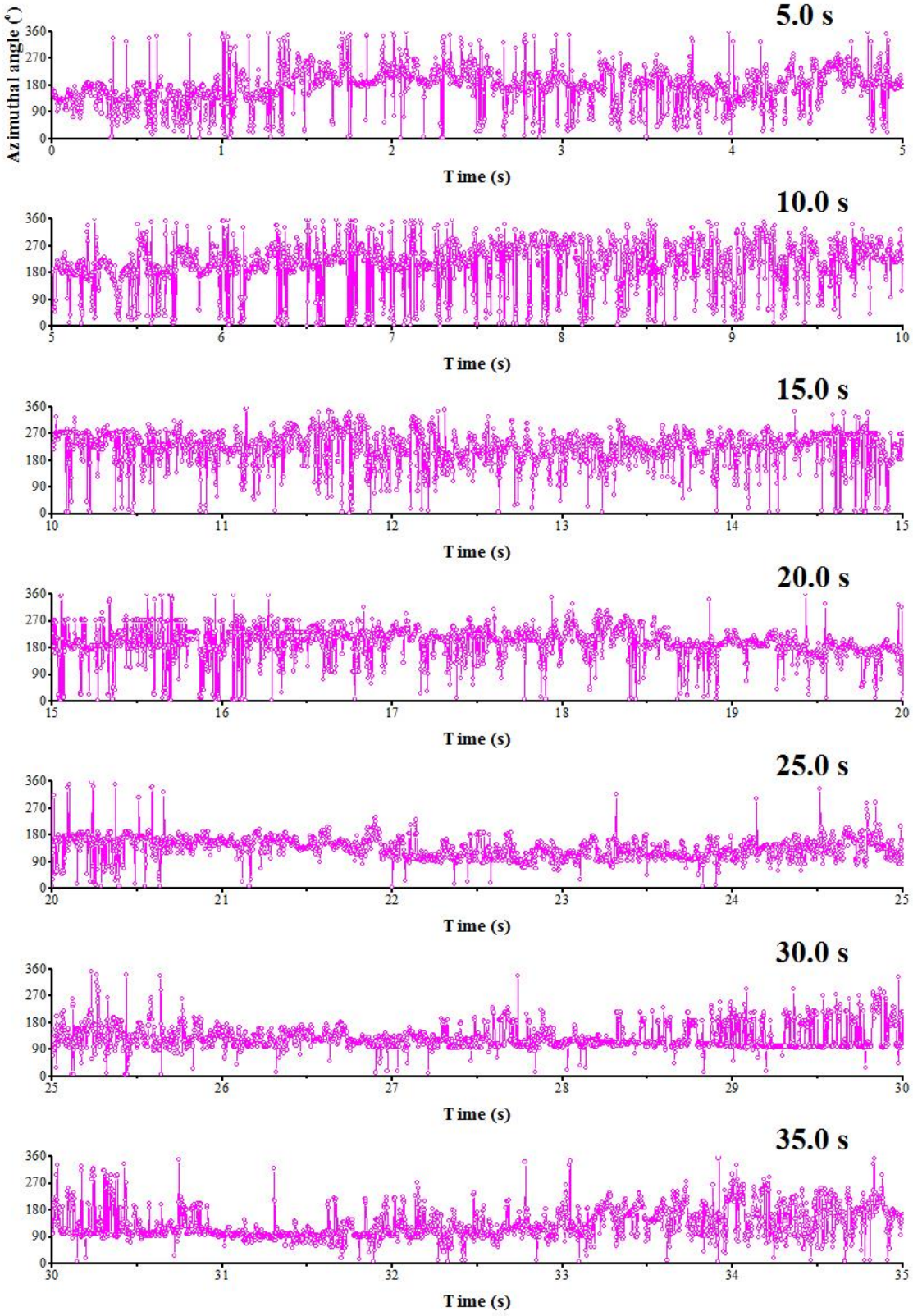
5.0 s
10.0 s
15.0 s
20.0 s
25.0 s
30.0 s
35.0 s
Azimuthal angle (°)
Time (s)

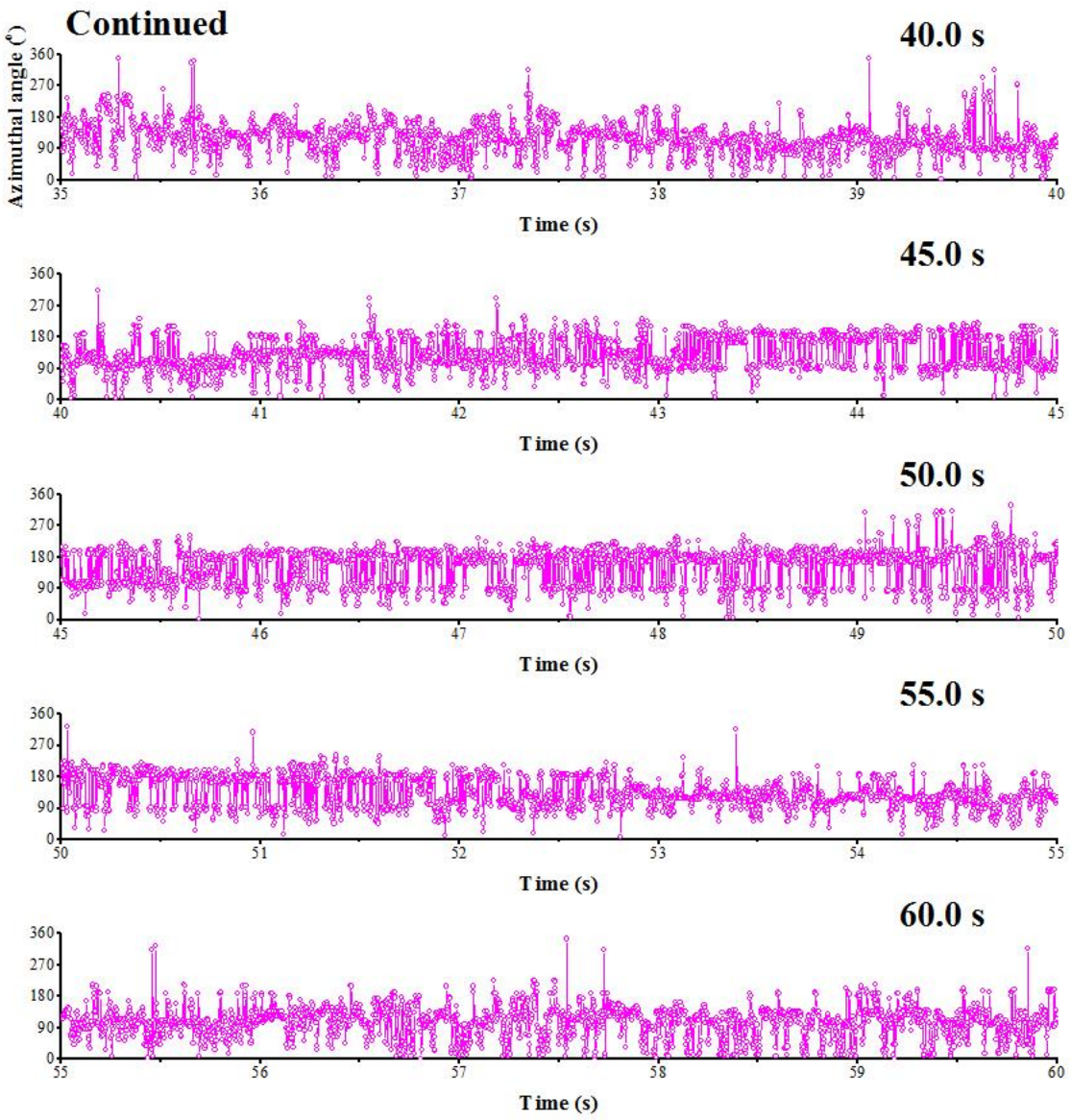

Figure 12. Dynamic trace of azimuthal angles from a AuNR in glycerol solution. The azimuthal angles of the same nanorods as in Fig. 10 were determined from automatically pattern matching program written with MATLAB codes. The frame rate is 2 ms/frame.

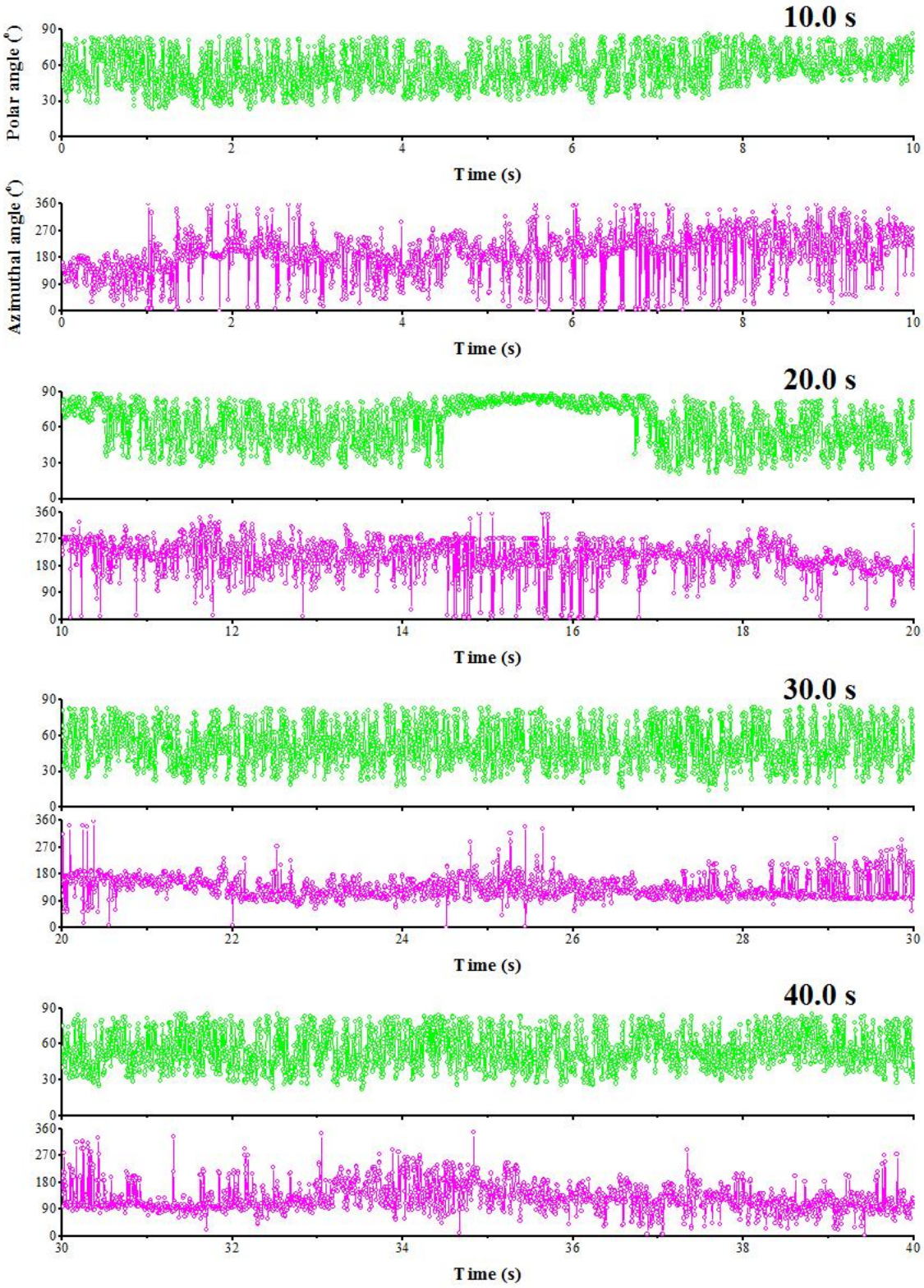
10.0 s
Polar angle (°)
Time (s)
Azimuthal angle (°)
Time (s)
20.0 s
Time (s)
30.0 s
Time (s)
40.0 s
Time (s)

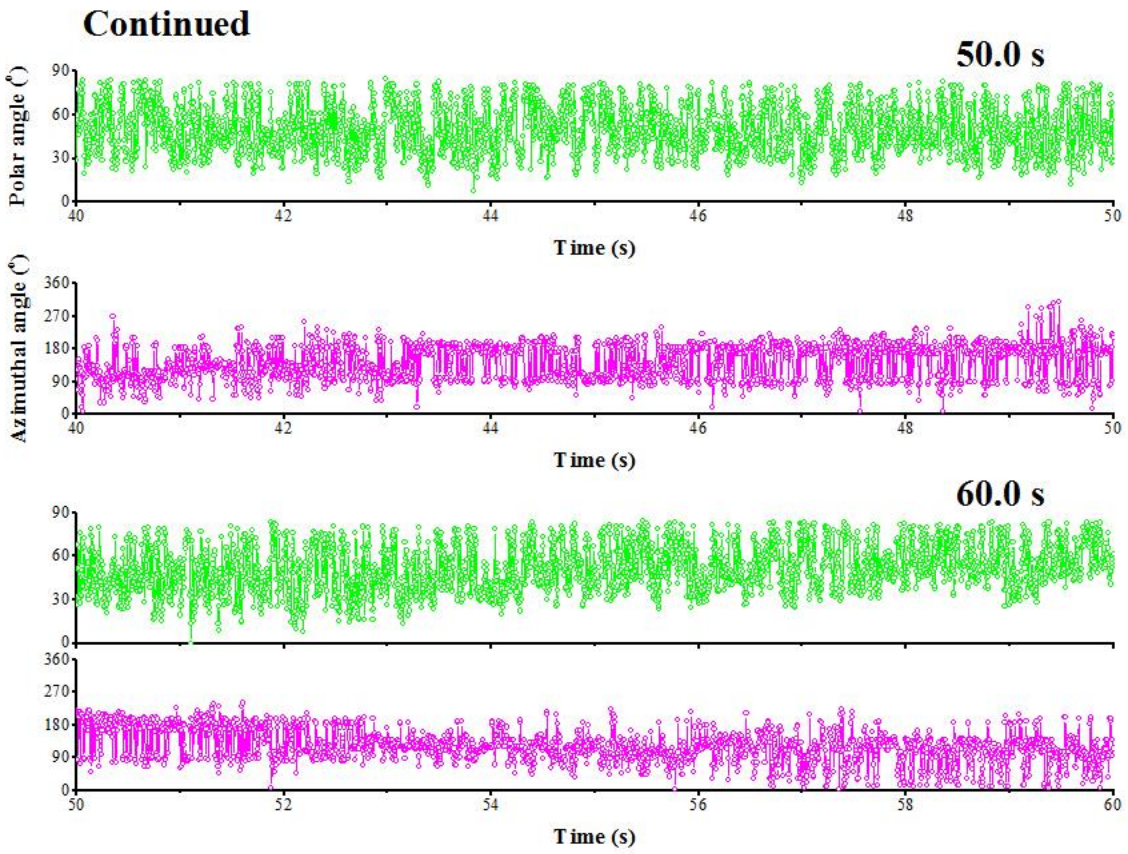

Figure 13. Dynamic trace of angles of nanorods with 4 ms imaging rate. The tracking movies were formed through binning of the original 2 ms tracking movie.

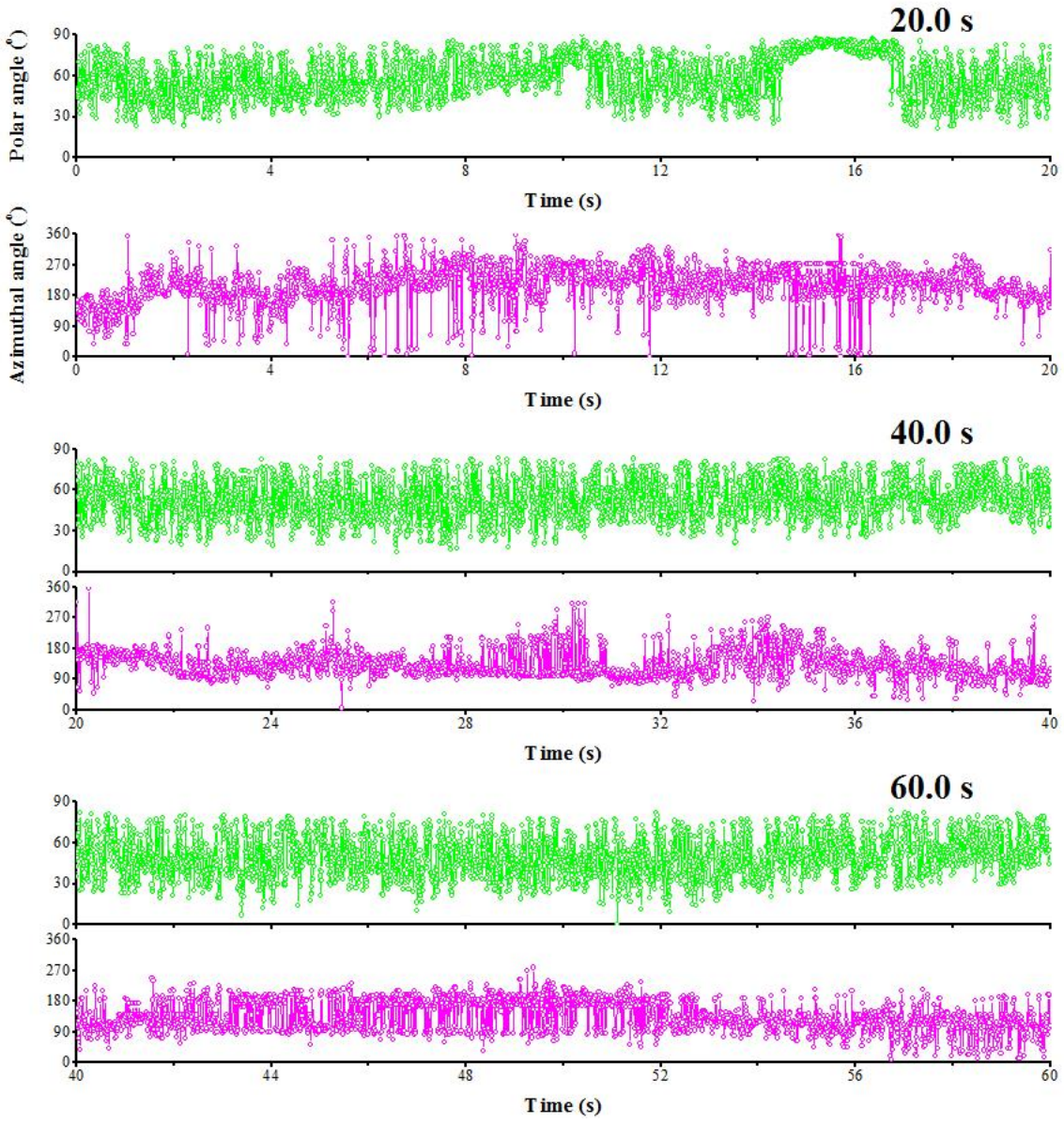

Figure 14. Dynamic trace of angles of nanorods with 8 ms imaging rate. The tracking movies were formed through binning of the original 2 ms tracking movie.

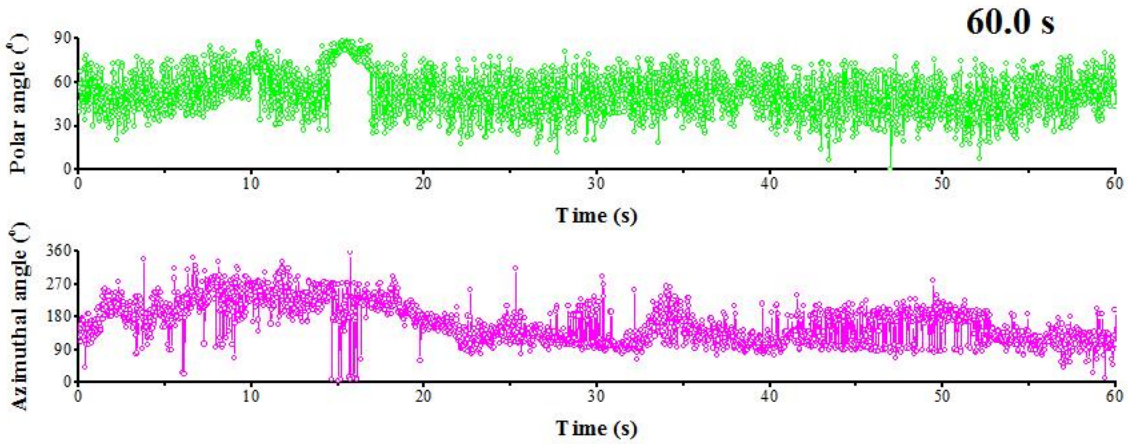

Figure 15. Dynamic trace of angles of nanorods with 20 ms imaging rate. The tracking movies were formed through binning of the original 2 ms tracking movie.

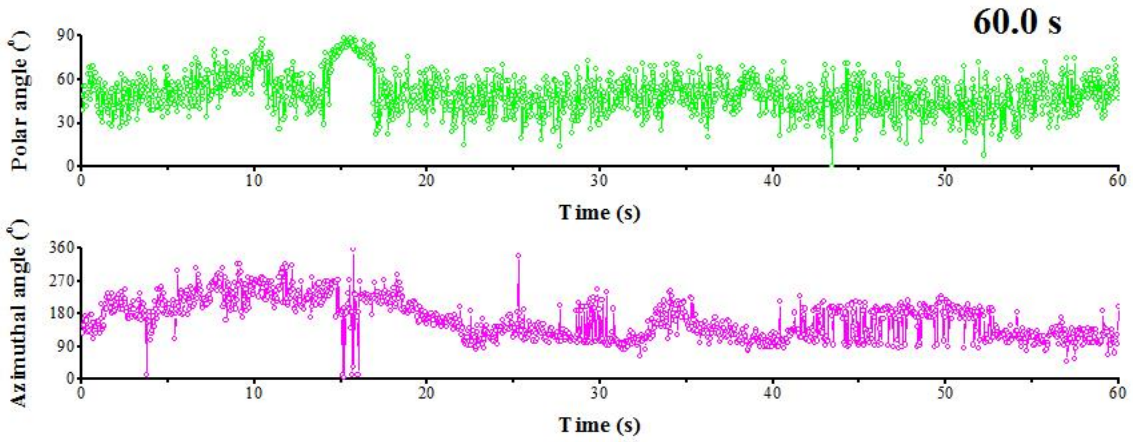

Figure 16. Dynamic trace of angles of nanorods with 40 ms imaging rate. The tracking movies were formed through binning of the original 2 ms tracking movie.

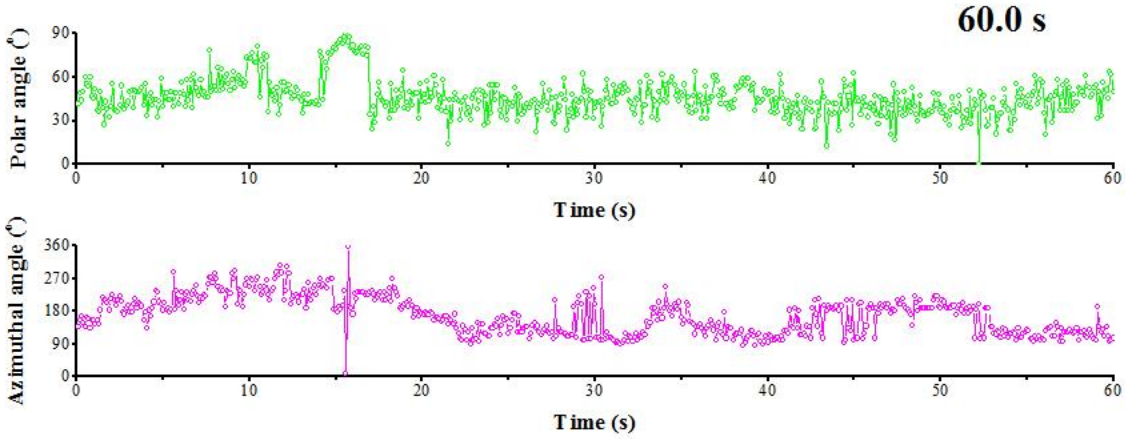

Figure 17. Dynamic trace of angles of nanorods with 100 ms imaging rate. The tracking movies were formed through binning of the original 2 ms tracking movie.

CHAPTER 5: GENERAL CONCLUSIONS

The work presented with centers of developing super-resolution and super-localization imaging methods for studying chemical and biological processes. Three optical sectioning strategies, namely TIR illumination, variable-angle illumination and light sheet illumination, were used as microscopy imaging techniques for the majority of the work.

In the first project, VAE illumination and dSTORM were combined to successfully applied for super-resolution imaging in thick sample such plant root cells. The achieved spatial resolution was quantified (< 50 nm) through cluster analysis. The increased illumination depth yet still well-confined in VAE and the proper labeling density of fluorophores so that fluorophores can be optically resolved work as a whole to resolve the CMT network in plant root cells with a spatial resolution beyond diffract limit. The former helps to excite fluorophores deep inside the plant cells while still maintain low fluorescence background allowing single fluorescent molecule be detected with sufficient high SNR and localized with nanometer precision. The latter is approached by optimize the immunolabeling procedures. Results from quantitative analysis of the CMT network including densities and orientations show the dramatic differences in spatial organization of cortical microtubules in cells of different differentiation stages or types. Future work could be in areas such as imaging of additional elements of the cytoskeleton, organelle substructure, membrane domains and other structures currently only accessible by electron microscopy; revealing the

relationships between subcellular organs and cytoskeleton using multicolor super-resolution microscopy; and so on.

The localization based super-resolution microscopy is also applied for imaging the molecular transportation, the catalytic reaction and their coupling at single molecule and single channel level in a multilayer mesoporous nanocatalysts. The multilayer nanocatalyst is a complex structure with well-defined geometry including Pt NPs sandwiched between an optically transparent solid SiO2 core and a mesoporous SiO2 shell with well-aligned pores. A fluorogenic oxidation of non-fluorescent amplex red to highly fluorescent resorufin is used as model chemical reaction to test the core-shell nanocatalysts. Molecular trajectory with Sub-10-nm localization precision reveals resorufin molecules diffuse two magnitude of orders slower in a nanopore than in free solution. Moreover, at least three sub-populations of different diffusion coefficients (fast: 0.022 $\mu m^2/s$, slow: 0.0068 $\mu m^2/s$ and very slow: 0.0021 $\mu m^2/s$) were found and their motions are restricted with varied strength that could be caused by the initial adsorption of resorufin molecules on Pt NPs or the adsorption-desorption of resorufin molecules on inner surface of nanopores. While the fast mobile fraction follows a free diffusion behavior (Brownian diffusion) ($\alpha = 0.98$), two slow mobile fractions are restricted with degrees at $\alpha = 0.84$ (slow) and $\alpha = 0.66$ (very slow). These results showing the heterogeneity of nanopore structure can only be revealed by super-localization microscopy. The future work will continue study the coupling of molecular transportation and catalytic reaction in terms of reaction kinetics: diffusion dominated vs. chemical reaction dominated. Moreover, effects of pore length, pore size and pore properties (hydrophobic vs. hydrophilic) on catalytic reaction rates and mechanisms will be studied.

Finally, the design and built of RLSM is described and applied for three-dimensional tracking of the orientation changes of anisotropic plasmonic gold nanoparticles in aqueous solutions with very high viscosity. A dual-view detection system with two approaches including DC-RLSSM and bifocal RLSSM were demonstrated to determine polar angles and azimuthal angles simultaneously. Because of the enhanced absorption and scattering strength from plasmonic AuNRs and largely reduced background of thin excitation volume in RLSM, fast imaging rate up to 500 fps is achieved and demonstrated. Rather follows free rotational diffusion, both slow rotation mode and fast rotation mode of AuNRs in glycerol solution are only revealed under very fast imaging speed. Possible future work will focus on in vivo studying orientation changes in 3D of biological processes such as membrane diffusion, endocytosis, intracellular transportation and so on.

The advancement in single localization based microscopy had already and will continue to bring new discoveries and insights in understanding the chemical and biological processes at molecular level.

ACKNOWLEDGEMENTS

There are lots of people helped me to finish my research in graduate school. First, I want to say thanks to Dr. Ning Fang who guided me to finish all my research work here. He helped me not only in the lab, but also in the daily life. I want to thank Dr. Huang for being my major advisor during my last time here. Dr. Huang helped me to finish the catalysis project.

I would also want to thank my committee: Dr. R. S. Houk, Dr. Emily Smith, Dr. Diane Bassham and Dr. Sanjeevi Sivasankar. I really appreciate their help and suggestions for finishing my research work here. I took the Chem 511 class taught by Dr. Houk. It was early morning at 8 am, three days a week. I had a very deep memory how I was struggling to get up early at 6 am and run to catch bus when it was still dark in winter mornings. Luckily, my hard work for getting up did not go to waste. I love that class. It was very fun. I also took Chem 513 in Dr. Smith's class. I learned lots of things like spectroscopy, optical instruments and so on. These helped me a lot during my research work. My first project in plant cell imaging was cooperated with Dr. Bassham's lab. She is always very generous to give us money to buy stuff which is very important for us to eventually accomplish the super-resolution imaging of cellular structures in plant root. I learned a lot about making good plans for future career and what to do if something happens to you from conversations with Dr. Sivasankar. He is a very wise and kind person I must say.

I would thank Dr. Bo Huang from University of California at San Francisco, Dr. Shaobin zhu who worked as a postdoc in our lab, and Xiaochen Yang for helping me finish my project in plant cell imaging. Xiaochen is very hard working person and very nice friend too. It often took

us more than two or three days to prepare the root samples. He is the one who stayed late in the lab to do all those work. I want to thank Dr. Chaocian Xiao and Yuchen Pei from Dr. Huang's lab for their help on my catalysis project.

I also want to thank both the previous and current group members: Dr. Shaobin Zhu, Dr. Kyle Marchuk, Dr. Yan Gu, Dr. Anthony Stender, Dr. Ji Won Ha, Dr. Rui Han, Dr. Ashely Augspurger, Kuangcai Chen, Amanda Nguy, and Fei Zhao. Because of those discussions, arguing and even fighting that we had, life became much easier and colorful in the lab.

At last but most importantly, I want to say thanks to my families. Their silent support is always the force pushing me forward.

This work was performed at Ames Laboratory under Contract No. DE-AC02-07CH11358 with the US. Department of Energy. The United State government has assigned the DOE Report number IS-T 3145 to this thesis.